Spring 5-10-2014

Oscillatory Network Activity in Brain Functions and Dysfunctions

Bhim M. Adhikari

OSCILLATORY NETWORK ACTIVITY IN BRAIN FUNCTIONS AND DYSFUNCTIONS

By

BHIM MANI ADHIKARI

Under the Direction of Dr. Mukesh Dhamala

ABSTRACT

Recent experimental studies point to the notion that the brain is a complex dynamical system whose behaviors relating to brain functions and dysfunctions can be described by the physics of network phenomena. The brain consists of anatomical axonal connections among neurons and neuronal populations in various spatial scales. Neuronal interactions and synchrony of neuronal oscillations are central to normal brain functions. Breakdowns in interactions and modifications in synchronization behaviors are usual hallmarks of brain dysfunctions. Here, in this dissertation for PhD degree in physics, we report discoveries of brain oscillatory network activity from two separate studies. These studies investigated the large-scale brain activity during tactile perceptual decision-making and epileptic seizures.

In perceptual decision-making study, using scalp electroencephalography (EEG) recordings of brain potentials, we investigated how oscillatory activity functionally organizes different neocortical regions as a network during a tactile discrimination task. While undergoing EEG recordings, blindfolded healthy participants felt a linear three-dot array presented electromechanically,

under computer control, and reported whether the central dot was offset to the left or right. Based on the current dipole modeling in the brain, we found that the source-level peak activity appeared in the left primary somatosensory cortex (SI), right lateral occipital complex (LOC), right posterior intraparietal sulcus (pIPS) and finally left dorsolateral prefrontal cortex (dlPFC) at 45, 130, 160 and 175 ms respectively. Spectral interdependency analysis showed that fine tactile discrimination is mediated by distinct but overlapping ~15 Hz beta and ~80 Hz gamma band large-scale oscillatory networks. The beta-network that included all four nodes was dominantly feedforward, similar to the propagation of peak cortical activity, implying its role in accumulating and maintaining relevant sensory information and mapping to action. The gamma-network activity, occurring in a recurrent loop linked SI, pIPS and dlPFC, likely carrying out attentional selection of task-relevant sensory signals. Behavioral measure of task performance was correlated with the network activity in both bands.

In the study of epileptic seizures, we investigated high-frequency (> 50 Hz) oscillatory network activity from intracranial EEG (IEEG) recordings of patients who were the candidates for epilepsy surgery. The traditional approach of identifying brain regions for epilepsy surgery usually referred as seizure onset zones (SOZs) has not always produced clarity on SOZs. Here, we investigated directed network activity in the frequency domain and found that the high-frequency (>80 Hz) network activities occur before the onset of any visible ictal activity, and causal relationships involve the recording electrodes where clinically identifiable seizures later develop. These findings suggest that high-frequency network activities and their causal relationships can assist in precise delineation of SOZs for surgical resection.

INDEX WORDS: Perceptual decision-making, Spectral Granger causality, Cortical sources in tactile discrimination, High-frequency oscillations, Seizure localization, Epilepsy surgery.

OSCILLATORY NETWORK ACTIVITY IN BRAIN FUNCTIONS AND DYSFUNCTIONS

by

BHIM MANI ADHIKARI

A Dissertation Submitted in Partial Fulfillment of the Requirements for the Degree of

Doctor of Philosophy

in the College of Arts and Sciences

Georgia State University

2014

OSCILLATORY NETWORK ACTIVITY IN BRAIN FUNCTIONS AND DYSFUNCTIONS

by

BHIM MANI ADHIKARI

Committee Chair: Mukesh Dhamala

Committee: Vadym M. Apalkov

Richard W. Briggs

Gennady S. Cymbalyuk

Brian D. Thoms

Electronic Version Approved:

Office of Graduate Studies

College of Arts and Sciences

Georgia State University

May 2014

DEDICATION

To my parents, lovely son Bipin, daughter Sneha

And

Wife Bipana

ACKNOWLEDGEMENTS

I would like to take this opportunity to thank the people who inspired and supported me towards my PhD studies and helped me to complete it. Honestly, I knew very little about the research in this field when I was admitted at Georgia State University and joined in Dr. Dhamala's research group. First of all, my enormous thanks and gratitude goes to my advisor Dr. Mukesh Dhamala, whose continuous guidance, inspiration and supervision made this work possible. He was always ready to explain and help me when I had questions in every aspect of learning, designing and conducting experiments, arranging and analyzing data. I found myself extremely fortunate to work with an advisor like Dr. Dhamala.

Next, I am grateful to all members of the Neurophysics research group for their valuable suggestions. Dr. Charles M. Epstein, Dr. Krish Sathian have been truly instrumental in shaping my research projects and I would like to gratefully acknowledge them for their inputs and feedback. I would like to thank Dr. Awadhesh Prasad for providing his valuable inputs and guiding support and to Dr. Dean Sabatinelli for collaborative works.

I would like to thank to my parents, my son Bipin, daughter Sneha, and brothers for their unconditional infinite love and support throughout my endeavor. Most importantly, I would like to express my special thanks to my lovely wife, Bipana, for her all love, invaluable dedication, sacrifice and companionship. For me, she has always been a source of inspiration to work hard and succeed. Without her presence, it would have been much more difficult to finish this dissertation.

Finally, I would like to remember my late mother (she passed away during my PhD studies) who raised me to become the person I am now. I want to thank all of my family members, colleagues who have helped me in any way they could during the course of my graduate study.

TABLE OF CONTENTS

LIST OF TABLES

LIST OF FIGURES

LIST OF ABBREVIATIONS

α	alpha
A	anterior
AC	alternating current
AD	Alzheimer's disease
AEDs	antiepileptic drugs
ASEO	analysis of single-trial ERP and ongoing activity
β	beta
BESA	Brain Electrical Source Analysis
BOLD	blood oxygenation level dependent
C	spectral coherence
Ch	coherence
CT	computed tomography
δ	delta
dc	direct current
dlPFC	dorsolateral prefrontal cortex
ECOG	electrocorticography
EEG	electroencephalography
ERP	event-related potential
F	net causal outflow
f	frequency
FEF	frontal eye field
fMRI	functional magnetic resonance imaging

γ	gamma
GABA	gamma-aminobutyric acid
GC	Granger causality
H	transfer function
HFOs	high-frequency oscillations
Hz	hertz
I	band-integrated Granger causality
IEEG	intracranial electroencephalography
iGC	integrated Granger causality
kΩ	kilo-Ohm
L	left
LFPs	local field potentials
LOC	lateral occipital complex
MEG	magnetoencephalography
mm	millimeter
MNE	minimum-norm estimate
MRI	magnetic resonance imaging
ms	millisecond
N	total number of nodes
OF	net causal outflow
OF_{ch}	net causal outflow averaged over recording channel
OF_f	net causal outflow averaged over frequency
OF_t	net causal outflow averaged over time

P	posterior
P	power
PCS	postcentral sulcus
PD	Parkinson’s disease
PET	positron emission tomography
pIPS	posterior intraparietal sulcus
R	right
s	second
S	spectral density matrix
SD	standard deviation
SEEG	stereotactic encephalography
SI	primary somatosensory cortex
SOZs	seizure onset zones
SPECT	single-photon emission computed tomography
θ	theta
t	time
TI	total interdependence
WM	working memory
Σ	noise covariance matrix
ΔOF	integrated causal outflow difference

1 INTRODUCTION

1.1 Introduction

This dissertation describes two studies on brain oscillatory network activity. The first study is on tactile perceptual decision-making in healthy human participants. The second study is on epileptic seizures in patients admitted in Emory University Hospital for epilepsy surgery. In chapter 2, a short description of the brain neuronal oscillations and network activity is presented. We describe electroencephalography (EEG), intracranial EEG (iEEG) and epileptic seizures and high-frequency oscillations (HFOs). Chapter 3 is about the oscillatory neocortical networks underlying decision-making processes in the somatosensory domain. The experimental set-up, materials and methods, results and the discussion of these results are given in detail. Chapter 4 describes the use of the spectral Granger causality analysis in order to localize the seizure onset zones (SOZs) and onset times. The wavelet-based power, spectral measures such as coherence and Granger causality are used to specify the characteristics of the seizure networks. Chapter 5 summarizes the main conclusions of these studies.

The dissertation is based upon the following peer-reviewed publications:

- **B. M. Adhikari**, K. Sathian, C. M. Epstein, B. Lamichhane, and M. Dhamala, "Oscillatory activity in neocortical networks during tactile discrimination near the limit of spatial acuity", Neuroimage 91, 300-310 (2014).
- **B. M. Adhikari**, C. M. Epstein, and M. Dhamala, "Localizing epileptic seizure onsets with Granger causality", Physical Review E 88, 030701 (Rapid) (2013).

❖ C. M. Epstein, **B. M. Adhikari**, R. Gross, J. Willie, M. Dhamala, "Application of High-Frequency Granger Causality to Analysis of Epileptic Seizures and Surgical Decision Making", in revision, Epilepsia (2014).

My other relevant peer-reviewed publications that are not included in this dissertation are the following:

❖ D. Sabatinelli, L. McTeague, M. Dhamala, D. Frank, T. Wanger, **B. M. Adhikari**, "Reduced medial prefrontal-subcortical connectivity in dysphoria: Granger causality analyses of rapid functional MRI", in press, Brain Connectivity (2014).

❖ **B. M. Adhikari**, K. Quinn, and M. Dhamala, "Is the brain's inertia for motor movements different for acceleration and deceleration? ", PLOS ONE 8(10), e78055 (2013).

❖ **B. M. Adhikari**, E. Goshorn, B. Lamichhane, and M. Dhamala, "Temporal order judgments of audiovisual events involve network activity between parietal and prefrontal cortices", Brain Connectivity, 3(5), 536-545 (2013).

❖ S. Bajaj, B. Lamichhane, **B. M. Adhikari**, and M. Dhamala, "Amygdala mediated connectivity in perceptual decision-making of emotional facial expressions", Brain Connectivity, 3(4), 386-397 (2013).

❖ S. Bajaj, **B. M. Adhikari,** and M. Dhamala, "High-frequency network activity flow predicts low-frequency node activity in fMRI BOLD fluctuations", PLOS ONE 8(5), e64466 (2013).

❖ **B. M. Adhikari**, A. Prasad, and M. Dhamala, "Time-delay-induced phase-transition to synchrony in coupled bursting neurons", Chaos 21, 023116 (2011).

❖ A. Prasad, M. Dhamala, **B. M. Adhikari**, and R. Ramaswamy, "Targeted Control of Amplitude Dynamics in Coupled Nonlinear Oscillators", Physical Review E 82, 027201(2010).

❖ A. Prasad, M. Dhamala, **B. M. Adhikari**, and R. Ramaswamy, "Amplitude Death in Nonlinear Oscillators with Nonlinear Coupling", Physical Review E 81, 027201 (2010).

The following manuscripts have already been submitted to various scientific journals and are under review or in revision process.

❖ D. Sabatinelli, D. W. Frank, T. J. Wanger, M. Dhamala, **B. M. Adhikari**, and X. Li, "The timing and directional connectivity of human frontoparietal and ventral visual attention networks in emotional scene perception", under review in Neuroscience (2014).

❖ B. Lamichhane, **B. M. Adhikari**, S. F. Brosnan, and M. Dhamala, " The neural basis of perceived unfairness in economic exchanges", in revision, Brain Connectivity (2014).

2 OSCILLATIONS AND NETWORKS

2.1 Brain oscillations

The human brain consists of a large number of highly interconnected neuronal populations that are functionally organized in both short-range, local-area ensembles and long-range, large-scale networks supporting various functions, including cognitive and perceptual [1,2]. These large-scale functional networks, which can exist even "at rest" in the absence of task performance or of explicit external stimuli, involve not only the oscillatory activities of individual neural systems and inter-regional coherence of oscillatory activity, but also the directional interactions between them. Knowledge of brain network activity is important not only to understand how different brain areas work together for cognitive and perceptual processes in health, but also to understand how such coordinated activity breaks down in disease.

Neurons or neuronal populations often show rhythmic or repetitive activity, called oscillation. Neural oscillations can be seen in all measurement levels, e.g. from a single neuron, local field potentials (LFPs) and large-scale brain recordings [2,3]. At the level of single neuron, oscillations can appear either as oscillations in membrane potential or as rhythmic patterns of action potentials, which then produce oscillatory activation of post-synaptic neurons. At the level of neural ensembles, synchronized activity of large numbers of neurons can give rise to macroscopic oscillations, as observed in the electroencephalography (EEG) recordings. Oscillatory activity in groups of neurons generally arises from feedback connections between the neurons that result in the synchronization of their firing patterns. The possible roles of neural oscillations include feature binding, perception, information transfer mechanisms, and the generation of rhythmic motor output.

Macroscopic EEG signals arising from the brain consist of several simultaneous oscilla-

tions; can be subdivided into frequency bands such as delta (1-3 Hz), theta (4-8 Hz), alpha (8-12 Hz), beta (13-30Hz) and gamma (30-80 Hz). Working memory processes seem to be reflected as oscillations within the theta frequencies. Alpha frequency responses can be observed in association with tasks requiring alertness, attention and semantic memory processes [4]. Beta rhythm responses are reported in association with cognitive processing [5]. Gamma brain oscillations have been observed in association with visual, auditory and motor tasks and might exist in a number of brain structures with somewhat different functional/behavioral correlates. The frequency of such oscillations determines the temporal windows of processing and indirectly the size of the neuronal structures involved [6,7]. In a wider time window, more neurons can be recruited from larger brain areas because synaptic and axonal conductance delays are less limiting. Hence, the spatial extent of synchrony is much larger for slow rhythms. Slow oscillations can involve many neuronal groups across widely distributed brain areas, whereas fast oscillations are generally predestined for local information processing due to their shorter time window for information exchange [1,8].

Different neural generators are involved in the generation of these brain oscillations at different frequencies. Hippocampal neural activity seems to be reflected as oscillations within the theta frequency range while the alpha rhythms seem to be mainly generated by corticocortical and thalamocortical neural networks. In general, subcortical structures, especially the thalamus, appear to dominate in the generation and synchronization of oscillatory activity in the lower frequency bands (α, θ, δ and below) [9,10]. The neural synchronization in the high-frequency range (β- and γ- band) is mediated by cortico-cortical connections that reciprocally link cells situated in the same cortical area, but also cells distributed across different areas and even across the two hemispheres [11,12].

Neural oscillations play an important role in many neurological disorders, such as excessive synchronization during seizure activity in epilepsy or tremor in patients with Parkinson's disease (PD). Though there are large numbers of studies investigating the role of synchrony in a wide range of cognitive and executive processes, relatively few investigations have examined the possible relevance of neural synchrony in pathological brain states, such as epilepsy, schizophrenia, autism, and Alzheimer's disease (AD). Oscillatory activity can also be used to control external devices in brain-computer interfaces, in which subjects can control an external device by changing the amplitude of particular brain rhythms.

2.2 Relevance of network studies

Questions regarding the brain functions can only be answered by studying the group dynamics of neurons or neuron populations. Information processed at the neuronal level often needs to be integrated across brain regions to be functionally useful [13]. Nowadays, many researchers are trying to understand how brain networks are organized to support this type of operation [14,15]. Moreover, the dysfunction or deviation from the normal functioning of large-scale brain networks is increasingly observed in many brain disorders [16]. The network approaches have thus become useful for understanding how connected regions work together in cognitive functions. These network approaches are also providing new insights into aberrant brain organization in several neurological disorders such as epilepsy, autism, schizophrenia and others.

The following factors are responsible for the surge of interest of using about network approaches to characterize network level oscillatory interactions and/or activities. At present, various advanced mathematical methods are far more accessible than before to study oscillations. Standard computer software available now makes spectral analysis relatively easy, and modern computers have the necessary speed and memory capacity to apply these techniques to large da-

tasets. Moreover, computational neuroscientists have pushed the experimentalists studying neurophysiology to consider network phenomena rather than focusing their attention primarily on the response recorded from a single electrode. In addition, the ability to record EEG from small regions of the human brain using intracranial methods has demonstrated that prominent oscillations like those long studied in rodents and cats are also present in human cortex and hippocampus [17,18].

Though recent studies have revealed large-scale oscillatory brain networks associated with perceptual decision-making processes in the visual domain [19] and in the auditory-visual domains [20], very little is known in case of the somatosensory domain. The study of fine tactile discrimination in the somatosensory domain is expected to fill scientific knowledge gaps in hierarchical neural processing and to provide useful information for clinical applications. Accurate localization of the seizure onset zones based on the information obtained from intracranial electroencephalography recordings is a complex and imperfect process. Answers to the following questions help to analyze features of seizure networks and to aid in surgical decision-making: (i) Are network activity measures like Granger causality (GC) useful to localize the seizure onset zones? (ii) Can the complexity of the network activity predict the surgical outcome (seizure-freedom or not)? (iii) Can preictal or interictal activities predict a seizure occurrence? In both of the studies, the spectral GC approach was used. GC is a new and effective data-driven way of looking at network interactions, and it enhances our ability to identify key brain structures underlying the organization of a given behavior.

2.3 Electroencephalography and intracranial EEG

Richard Caton published reports on his detection of electrical activity in animal brains [21]. He used the galvanometer over the human scalp to record brain activity in the form of elec-

trical signals in 1875, and was probably the first to do so. Since then, the concept of electro-(electrical activity) encephalo-(signals emitting from the head) and gram or graphy (drawing or writing) combined together established the *"electroencephalogram"* which was henceforth used to denote the neuronal electrical activity of brain.

Hans Berger began his studies of human EEG in 1920. His discovery that the brain generates a low-level sub-audio frequency electrical activity has led to the establishment of a clinical neurophysiological specialty known as electroencephalography. It was between 1926 and 1929 when Berger first obtained good recordings of the alpha waves [22-24] in human brain. He also first measured beta activity. In 1964, the British scientist W. Grey Walter discovered delta waves and theta activity which initiated enormous clinical interest in the diagnosis of brain abnormalities [25]. Electroencephalography (EEG) consists of recording the electrical activity produced by the firing of an ensemble of neurons by means of electrodes attached to the scalp [26].

EEG commonly refers to scalp EEG. Scalp EEG provides a poor spatial resolution of the cerebral location generating the scalp signals because of the smearing of neural electrical potentials introduced by the meninges, cerebrospinal fluid, skull bone and scalp. Stereotactic EEG (SEEG) and intracranial EEG (iEEG) provide solutions to some of the limitations of scalp EEG. SEEG records neural electrical potentials from depth electrodes (reaching potentially deeper and sub-cortical brain regions) consisting of 1-D linear electrode arrays shaped in the form of a needle [27]. IEEG or electrocorticography (ECoG) consists of 2-D grids or 1-D strips placed directly on the cortical surface or the dura. In the context of epilepsy, iEEG and SEEG are essentially two-step procedures. The first step involves identification of the epileptogenic area(s) by means of placements of subdural electrodes [28-31]. If that is successful, the second procedure involves resection of the epileptogenic area [32,33]. Both recording techniques provide better spatial and

temporal resolution and are thus able to better localize pathological cortical generators than scalp EEG. Indeed, the distortions of the EEG scalp potentials produced by the skull-scalp interface are avoided [34]. Further, iEEG and SEEG are not contaminated by the artifacts caused by muscle activity, eye movements and eye blinks [34,35]. The main disadvantage of SEEG and iEEG is invasiveness, which introduces risk of infection, bleeds, strokes, or other complications (<1%) from the surgical procedure, and significant cost [36]. Another fundamental disadvantage is that most of the cortex, besides area(s) under the implanted electrodes, remains unexplored. If the seizure onset zone is not covered, iEEG and SEEG techniques might lead to erroneous conclusions. For this reason, these techniques have limitations in investigating the connectivity of cortical networks for seizure initiation.

2.4 Epilepsy and high-frequency oscillations

Epilepsy is a neurological disorder characterized by recurrent unprovoked seizures. An epileptic seizure is an episode of disorganized electrical activity, typically related to excessive neuronal excitation in the cortex, with a broad range of symptoms, including loss of consciousness, involuntary movements, etc. A person who has experienced only one seizure cannot be qualified as being epileptic, since a healthy brain can be provoked into a seizure under various stresses. Epileptic seizures are unpredictable and may sometimes be resistant to antiepileptic medications, with consequent progressive neurological and cognitive dysfunction. Electrical changes in the brain related to seizures, often referred to as the ictal state, and typically last from seconds to minutes; however, in some instances prolonged seizure activity or a succession of seizures result in a life-threatening condition called status epilepticus. The period between seizures is referred to as the interictal state. Depending on the extent of involvement of the various brain regions, epileptic seizures are classified into two main groups; focal seizures, and generalized

seizures. Focal seizures, also called partial seizures, occur in a localized area of the brain, while generalized seizures are seen in the whole brain.

If the underlying cause of the seizures is known (tumor, trauma etc.), the epilepsy is termed as symptomatic. If the cause of seizures is unknown [computed tomography (CT) or magnetic resonance imaging (MRI) are normal], the epilepsy is termed as idiopathic. Seizures of the temporal lobe usually induce drastic changes to cognitive processes of an individual. Epilepsy of the temporal lobe can cause changes in moods and behavior [37]. The temporal lobe is one of the brain regions that are commonly involved in partial epileptic networks. Abnormal oscillations recorded from the hippocampus are assumed to play an important role in some epileptic syndromes [38]. The treatment of epilepsy involves the use of a palette of antiepileptic drugs (AEDs), as a first step. Medications generally work well in about 50% of the patients. These patients may remain seizure free if they strictly follow the medication regimen. In 20% of the cases, the frequency of seizures decreases greatly. About 30% of the patients continue to experience seizures (intractable) in spite of AEDs [39,40]. Neurosurgery for the resection of the seizure onset zone (SOZ) may a viable option in some cases. The SOZ is defined as the area of the cortex where the onset of a partial seizure is generated. Clinicians traditionally focus on localizing the generators of interictal and ictal events, such as the spike-and-slow-wave complex, for determining the cortical region potentially targeted for resection. A spike is a transient electrophysiological phenomenon that differs clearly from background activity, with typical durations of 10 to 100 milliseconds. A spike-and-slow-wave complex consists of spike followed by a slow wave. Currently, data can be recorded at high sampling rates (>1000 Hz) at a large number of recording sites (>100). Therefore, analysis of epileptic data has been made possible at high-frequency domains of the power spectrum. Recent studies of interictal high-frequency oscillations have re-

vealed what might be new markers of epilepsy, with greater sensitivity than spike-wave events [41,42]. Indeed, it has been proposed that the brain regions sustaining recurrent high-frequency oscillations (HFOs) may correspond to the SOZs.

HFOs are the field potentials that reflect short-term synchronization of neural activity and are believed to play important roles in both normal and pathologic brain function. The frequency spectrum covered by HFOs has been subdivided into so called ripples (80-200 Hz) and fast ripples (FR) (200-500 Hz), thereby defining potential new biomarkers of the SOZ. However, HFOs have been reported in healthy as well as epileptic subjects, thus making it difficult to distinguish between normal and pathologic HFOs (pHFOs) so far. It is assumed by several research groups that ripples reflect physiological HFOs, and that FR reflect pHFOs, although the distinction cannot be based on differences in their respective frequency range alone. The location of their generators also plays a major role. Indeed, ripples observed in the dentate gyrus of the hippocampus are considered as pathologic, because such high-frequency oscillatory bursts are generally not observed if the region is healthy. Oscillatory bursts in the range of 200-600 Hz can be observed in the normal neocortex. Ripples have been recorded in healthy controls [43-46] and are believed to play an important role in synchronizing neuronal activity and might be an essential mechanism to episodic memory [6]. Normal HFOs are believed to reflect the summation of inhibitory postsynaptic potentials (IPSP), produced by discharges of principal cells [47,48]. GABAergic neurons play a pivotal role in generation of HFOs and their local synchronization, whereas glutamatergic connections appear to control their strength, duration and long-range synchronization [49]. The degree of synchronization is highly precise to the scale of milliseconds but never reaches a point where an individual neuron becomes unidentifiable from surrounding cells, due to high synchronicity [50]. The first incidence of pHFOs in the range of 250-600 Hz was report-

ed in patients with mesial temporal lobe epilepsy [43]. FRs were observed during interictal periods, as well as during ictal onsets in rodents, thus strengthening the hypothesis of the role of FRs in epileptogenesis [43,45,51].

HFOs have a frequency in the range of 80 to 500 Hz, a duration in the range of 4 to 6 cycles, and magnitudes of about 3 to 5 standard deviation (SD) from baseline fluctuations at the same location and within the same frequency range [52,53]. HFOs are linked to the seizure onset zone (SOZ), and the surgical removal of regions generating them correlates with a seizure-free post-surgical outcome [54]. Though spikes and sharp-waves are the most significant clinical biomarkers for epilepsy, recent studies on HFOs (≥ 100 Hz) have suggested that the HFO events can be a more reliable indicator for the SOZs [55].

2.5 Measures of oscillatory network activity

Here, we first define spectral measures from two simultaneously measured time series, $x: x_1(1), x_1(2),...,x_1(t),...$ and $y: y_1(1), y_1(2),...,y_1(t),...$, where the sampling rate of measurement is $2 f_s$ (f_s is the maximum measurable frequency, or Nyquist frequency). Using either a parametric or a nonparametric spectral estimation approach [56-58], we can obtain the spectral density matrix ($S(f)$), the transfer function ($H(f)$), and the noise covariance matrix (Σ) from these time series. For nonstationary processes, the wavelet transforms-based nonparametric estimation [56,57] can be used and these quantities become functions of both time and frequency indices. Time-domain total interdependence (TI) between these two processes is a measure to reflect the total amount of mutual information between them and is defined in terms of the integrated spectral coherence C between them ([59]):

$$TI_{x,y} = -\frac{1}{f_s}\int_0^{f_s} \ln\left[1 - C(f)\right] df \qquad (1)$$

The coherence function $C(f)$ is defined as:

$$C(f) = \frac{\left|S_{xy}(f)\right|^2}{S_{xx}(f)S_{yy}(f)}, \tag{2}$$

where $S(f)$ is the spectral matrix that contains cross spectra (S_{xy}, S_{yx}) and auto spectra (power) (S_{xx}, S_{yy}). Granger causality from ***y*** to ***x*** in the spectral domain $[I_{y\to x}(f)]$ can be obtained as:

$$I_{y\to x}(f) = -\ln \frac{S_{xx}(f) - \left(\Sigma_{yy} - \frac{\Sigma_{xy}^2}{\Sigma_{xx}}\right)\left|H_{xy}(f)\right|^2}{S_{xx}(f)}, \tag{3}$$

where, by interchanging *x* and *y*, one can also compute Granger causality from the first node ***x*** to the second node ***y*** at frequency $f: I_{x\to y}(f)$. The time-domain Granger causality $(F_{y\to x})$ is obtained by integration over the entire frequency range:

$$F_{y\to x} = \frac{1}{f_s}\int_0^{f_s} I_{y\to x}(f)\, df. \tag{4}$$

Geweke showed that $TI_{x,y} = F_{x\to y} + F_{y\to x} + F_{x.y}$ [59],where $F_{x.y}$ is instantaneous causality between **x** and **y** unlike $F_{x\to y}$ and $F_{y\to x}$, which are causality for delayed interactions.

These measures can be computed for a number of recording channels in pairwise combinations time window by time window (t_w). For N recordings, the net causal outflow spectra $(OF(t_w))$ from a node *m* defines the driving strength from that node around time t_w:

$$OF_m(t_w, f) = \frac{1}{N-1}\sum_{i=1}^{N}[I_{m\to i}(t_w, f) - I_{i\to m}(t_w, f)], \tag{5}$$

where the self-causality $I_{m\to i}=0$ for all $i=m$. The integrated outflow (iOF) over frequency gives the time-domain outflow. Here, a positive OF refers to the net outgoing information flow away from the node (source) and a negative OF refers to the net incoming flow towards the node (sink).

3 OSCILLATORY ACTIVITY IN NEOCORTICAL NETWORKS DURING TACTILE DISCRIMINATION NEAR THE LIMIT OF SPATIAL ACUITY

3.1 Introduction

Dynamic interactions between widely separated but functionally related brain regions are central for perception and cognition. Interactions among neural systems enable synchronization of neuronal oscillations and collective brain rhythms [1]. Oscillatory synchronization is a suggested mechanism underlying the perception of external stimuli [2,60,61]. Sensory-guided, goal-directed behaviors such as planning appropriate motor responses to incoming stimuli, a process commonly known as perceptual decision-making [62-65], involve multiple sub-processes such as encoding of sensory evidence, planning of actions and mapping of sensory information to action plans. Recent neuroimaging studies have begun to reveal large-scale oscillatory brain networks associated with perceptual decision-making processes in the visual domain [19] and in the auditory-visual domains [20]. Yet little is known about the oscillatory brain networks underlying decision-making processes in the somatosensory domain.

Perceptual decision-making requires conscious stimulus perception and, in the somatosensory domain, it is known to involve functional coordination between somatosensory regions and higher cognitive regions such as parietal and prefrontal cortices [66]. Decision-making, as observed in monkeys performing vibrotactile discrimination tasks [67] , is a distributed function resulting from the joint activity of many higher-order cortical regions, not from serial processing. How the decision-related brain activity emerges and binds parietal and prefrontal cortices is not completely understood. Previous functional magnetic resonance imaging (fMRI) studies [68-70] have specified the brain regions associated with fine tactile spatial perception. These studies also examined directed interactions using blood oxygenation level-dependent (BOLD) data. Howev-

er, brain networks that appear unified in fMRI studies because of slow BOLD hemodynamic responses may in fact include processes that occur on multiple time scales. Thus, how these interactions occur at the neural level on a millisecond time-scale, what frequencies of information flow bind these areas in a network, and the evolution of activity over time are largely unknown.

Past studies provide clues about the timing of somatosensory responses and the feedback of control (attention) signals. The primary somatosensory cortex (SI) responds to electrical stimulation of the finger within 20-60 ms [71,72], parietal cortex and frontal cortices respond within 70–110 ms [73-75] and the brain response at 140 ms is modulated by attention to somatosensory stimuli [76,77]. These findings are consistent with the idea that SI responds to feedforward input under the influence of top-down attentional signals, but where and how the relevant processes take place has not been resolved. Our hypothesis is that a tactile perceptual decision involves an oscillatory network linking somatosensory, parietal and prefrontal regions consistent with the flow of sensory and attention signals. Here, we designed an electroencephalography (EEG) study to test this hypothesis and provide insight into the neural basis of fine tactile spatial discrimination of the kind necessary for Braille reading, using a task near the limit of tactile spatial acuity.

3.2 Materials and methods

3.2.1 Participants

Fifteen neurologically normal right-handed volunteers (12 male, 3 female) participated in this study after giving informed consent. Their ages ranged from 18 to 42 years (mean: 24.7 years, standard deviation: 5.7 years). Two participants were excluded from the final analysis because of poor behavioral performance and/or unmanageable artifacts and noise present in their EEG data. The Institutional Review Boards of Georgia State University and Emory University

approved the experimental protocol.

3.2.2 *Tactile stimulation*

The experimental set-up was similar to that used in earlier fMRI studies [69]. A pneumatic stimulator was used to present tactile stimuli to the right index fingerpad. The tactile stimulus consisted of a three-dot array mounted on a square (20 mm × 20 mm) plate with the middle dot placed vertically equidistant and 1.94 mm to the left or right of the line joining the two outer dots spaced 4 mm apart vertically, as shown in Figure 3.1 (A). Dot height was 0.64 mm above the plate surface. The right index finger was immobilized in the supine position (palmar side up) in a finger mold mounted on the base of the stimulator, using thick, double-sided adhesive tape that also served as padding for comfort. A disk atop the stimulator allowed 180° rotation of a stimulus to facilitate rapid switching between left and right offsets. Care was taken to ensure that the stimulus array was properly centered on the base plate so that this rotation would result in symmetric positioning of the two stimulus alternatives. The stimulus was applied for 1s. A computer program written in Presentation (Neurobehavioral Systems, Albany, CA) controlled stimulation sequences and provided records of stimulus timings for synchronization with EEG recordings. Participants were blindfolded during tactile stimulation, and did not see the stimuli during the study.

3.2.3 Spatial discrimination task

Following the 1s stimulus, the participant responded within the next 2 s [Figure 3.1(A)]. Participants were asked to decide whether the central dot was offset to the left or right and to indicate their responses by left or right mouse-button clicks using their left hands. The offset used (1.94 mm) was near the spatial acuity limit under the conditions of stimulation.

3.2.4 Data acquisition and preprocessing

Prior to setting up for EEG acquisition, participants took part in a practice session to familiarize them with the task. Trials were presented in blocks of 20 (=1 minute) with an equal probability of left and right offsets. Two such blocks comprised the practice session. Following EEG set-up, participants were briefed on the basic principles of EEG and how to minimize introducing contaminants into the ongoing EEG signals.

Continuous EEG was recorded using a Neuroscan system with a 68-channel electrode cap, AgCl sintered electrodes, and SynAmps2 amplifiers at a sampling rate of 1000 Hz/channel (Neuroscan Systems, Charlotte, NC, USA). Analog-to-digital conversion was performed at a resolution of 24 bits. The electrode cap was aligned to standard cranial fiducials and exploring electrodes were referenced against the right mastoid. Electrode impedances were kept below 10 kΩ. Recordings were done for 30 blocks in 7 participants, 20 blocks in 5 and 10 blocks in 3 participants. Behavioral performance was analyzed and participants were categorized as good performers if their accuracy was at least 70% correct. The number of blocks with correct responses was 18.0 ± 2.0 (mean ± standard error).

EEG data were band-pass filtered between 1-100 Hz and notch filtered to remove 60 Hz AC-line noise. Data from bad electrodes was discarded and replaced, when appropriate, by spatial interpolation of the recordings from the neighboring working electrodes.

3.2.5 Data analysis

The analysis of the preprocessed EEG included these main steps: (i) computation of ERPs, (ii) EEG-source reconstruction based on ERPs and distributed dipole modeling, (iii) reconstruction of single-trial source waveforms based on the identified sources and discrete dipole modeling and (iv) computation of power, coherence and Granger causality spectra based on sin-

gle-trial waveforms and the parametric spectral approach [56]. The nonparametric wavelet-based spectral method [56,57] was used to examine the temporal variation of coherence. Details are provided below.

Using the stimulus onset times as reference, the data were segmented into trials of 700 ms duration (100 ms prestimulus and 600 ms poststimulus) and separated into correct and incorrect trials based on responses. For each trial, prestimulus data (100 ms prior to the stimulus) were used for baseline correction. Statistical procedures [78] were used in Matlab to identify outlier trials (3 standard deviations above or below the means) and discard them from the subsequent analysis. EEG trials associated with correct responses were collected from those task blocks that met the above-mentioned 70% correct performance threshold criterion for good performers. EEG trials for incorrect responses were also separated from all possible task blocks from all participants. Paired t-tests at $\alpha = 0.001$ were performed at each time point to test for differences between trials with correct and incorrect responses. These tests were performed separately for each channel and each participant. We regarded the response as being significantly different for correct vs. incorrect responses if the t-tests were significant at least across 20 consecutive time points and 2 adjacent channels (cluster correction). The EEG data were averaged across participants to arrive at grand average ERPs for correct and incorrect responses separately.

The grand average ERPs for correct responses were used in the Brain Electrical Source Analysis (BESA) Research software version 5.3.7 (www.besa.de) to reconstruct EEG sources on the cortical surface. We used the minimum-norm estimates (MNE) approach [79,80] to find the localized sources generating the scalp potentials. For distributed solutions, MNE uses l^2 minimum-norm (Euclidean norm) estimates to constrain the source solution. The locations of the sources can be constrained to the cortical surface and their orientations constrained to be perpen-

dicular to the local cortical surface [81]. Such constraints are based on the neurophysiological information that the sources of EEG signals are postsynaptic currents in cortical pyramidal cells, and that the direction of these currents is perpendicular to the cortical surface [82]. The peak activities of these sources were marked as network nodes for connectivity analysis. Using single-trial EEG data, we fitted dipoles at the peak activation locations of the localized sources with the dipole orientations given in Table 3.1. These dipole orientations were obtained from the MNE approach. We thus obtained single-trial source signal waveforms. The source signals were computed using a four-shell spherical head model and a regularization constant of 1% for the inverse operator. The source signals obtained from the single-trial EEG data were used in the connectivity analysis.

In order to see how neuronal synchrony in specific brain areas varied for correctly perceived stimuli over time, we studied two epochs: an earlier (30-140 ms) and a later (140-210 ms) period. The ERP results showed that the somatosensory response peaked as early as ~30 ms and differed for correct and incorrect responses starting at around 130 ms. For each epoch, we computed power spectra using the source waveforms from each network node. As the power density of EEG roughly follows power-law decay as frequency increases [1,83], modulations of spectral power are typically small in absolute magnitude at higher frequencies. Therefore, we computed the overall power spectrum and then separated the signal into two frequency ranges comprising the beta (12-30 Hz) and gamma (30-100 Hz) bands. This band-specific analysis allowed us to test whether beta and gamma band neuronal oscillations play independent roles in tactile perceptual decision-making as in the visual domain [19]. Band-specific, integrated power averages and the standard errors of the means were computed using data pooled across participants.

Spectral coherence between two oscillatory processes is a measure of statistical interde-

pendence between them and is derived from the normalized cross-spectral density function. Coherence between neural processes reflects frequency-specific inter-areal synchrony between oscillatory neuronal processes. Spectral Granger causality measures the directional influence from one oscillatory process to another [59,84]. These measures can be computed both by parametric and nonparametric methods [56,57]. Here, we applied the parametric method to single-trial EEG-source signals and computed network activity across the distributed neocortical regions found to be sources of the observed scalp-recorded activity. The difficulty of finding an optimal model order in the parametric approach [56] was circumvented by comparing power spectra from the nonparametric and parametric approaches at different model orders and choosing the model order yielding the lowest power difference. We evaluated the patterns of causality spectra by using both bivariate and conditional Granger causality. Conditional Granger causality analysis [56] was performed to distinguish direct and mediated causal influences, and to retain only the direct ones in the Granger causality network. We used the parametric spectral methods for all of these calculations. We used the wavelet transforms-based nonparametric approach [56,57] to determine the temporal changes of coherence that were predictive of the correct responses. The thresholds for statistical significance were computed from surrogate data by using permutation tests and a gamma-function fit [85,86] under a null hypothesis of no interdependence at the significance level $p < 10^{-6}$. We finally computed the net causal inflow by subtracting the Granger causality (obtained from the parametric method) out of the node from that into the node:

$F_m = \sum_{i=1}^{N}(I_{i\to m} - I_{m\to i})$, where N is the total number of nodes in a network and I is the band-integrated Granger causality, with self-causality assumed to be zero. Here, a positive F represents the net incoming information flow towards the node (sink) and a negative F refers to the net outgoing flow away from the node (source). The coherence and Granger causality calcula-

tions were done on the ensemble-average removed source signals between the time intervals 30-210 ms after stimulus onset. To check whether these spectral measures computed from single trial source waveforms after removing stimulus-triggered ensemble averages are affected by trial-to-trial variability in latency and amplitude [87], we applied the analysis of single-trial ERP and ongoing activity (ASEO) algorithm [88] to remove ensemble averages from single-trial source waveforms from all the nodes. We then computed power, coherence and Granger causality again from these ASEO-method treated waveforms and compared these spectral quantities with those obtained from the single trials after removing stimulus-triggered averages as mentioned above.

We included all the behavioral and EEG data of all participants. For each participant, we computed behavioral accuracy defined as the ratio of the number of correct responses (trials) to the total number of responses (trials). The accuracy was then converted into z-scores by using the average accuracy and standard deviation of individual participant results. We computed coherence and Granger causality spectra from the source waveforms for all responses (both correct and incorrect) from all participants. We then extracted coherence and Granger causality peak values to correlate with accuracy. The relationship in the scatterplot was assessed by both Spearman's rank correlation and Pearson's correlation. A correlation was considered significant if $p < 0.05$ for both results. Results are reported in terms of Spearman's rank correlation. A positive correlation indicates that greater accuracy relates to higher network coherence or Granger causality.

3.3 Results

3.3.1 Behavioral results

The overall accuracy for the task among good performers (see Methods) was 88.2 ± 1.9%

(mean ± standard error of the mean). Figure 3.1(B) shows the average accuracy for each good performer.

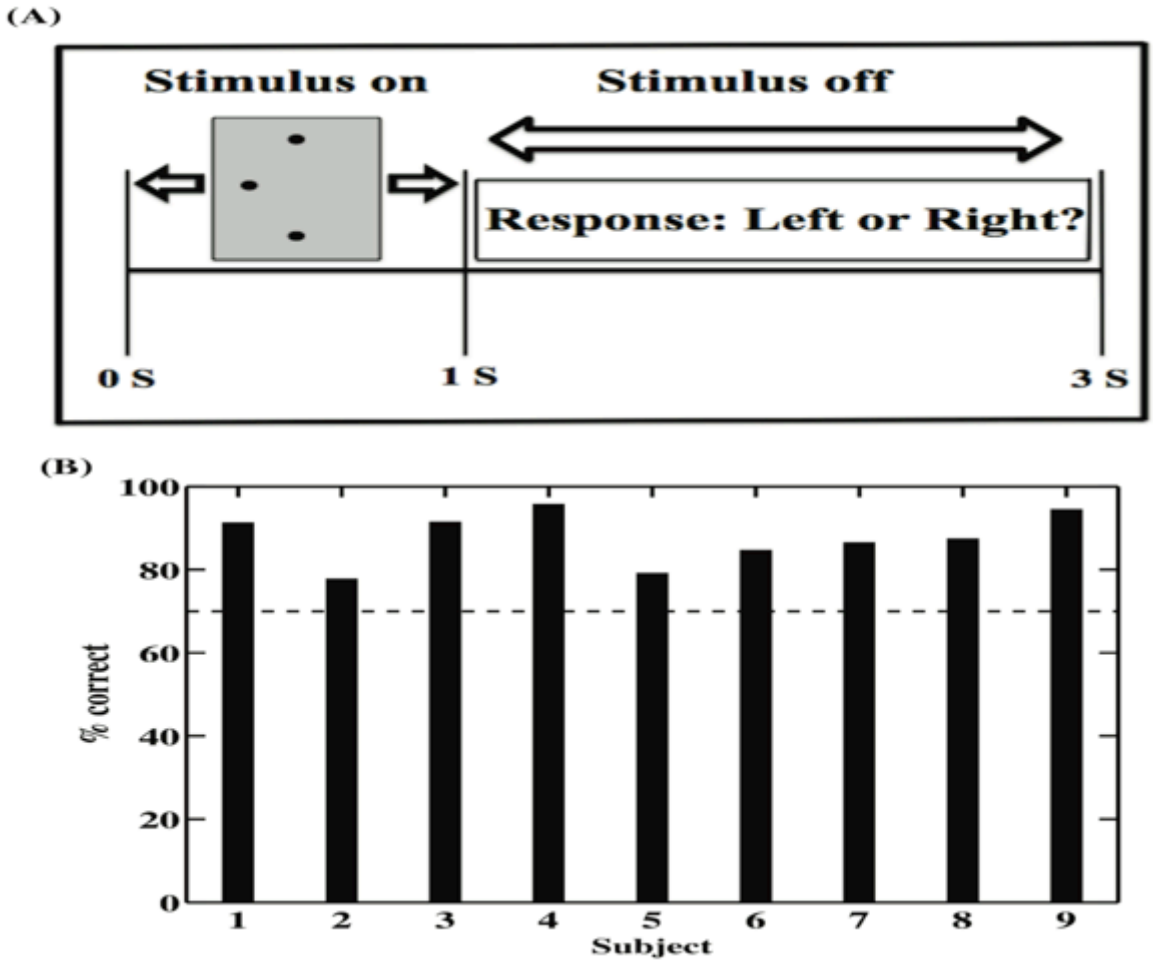

Figure 3.1 **Experimental set-up and behavioral performance.** (A). The middle dot of a raised 3-dot array was offset either to the right or left. A pneumatically driven stimulator presented stimuli to the right index fingerpad for 1s (on-interval) and participants responded within the next 2s (off-interval). (B). Behavioral performance accuracy rates of better performers are displayed here. Better performers have at least 70 % correct responses in two runs.

3.3.2 Electrophysiological results

Group-level average event-related potentials (ERPs): As shown in Figure 3.2, the average ERPs differed significantly between correct (blue traces) and incorrect responses (green traces)

at several scalp locations (shaded regions on the topographical map) during the timeframes indicated by the two vertical dashed lines in the ERP plots. These ERP differences between correct and incorrect responses survived paired t-tests at $p < 0.001$ and cluster-level thresholds (number of consecutive time points > 20 and number of adjacent channels > = 2) as described in the Materials and Methods section. Significant ERP differences in different blocks of channels were noted to begin around 140 ms.

Temporal evolution of cortically localized sources: The average ERPs for correct responses were used in the minimum-norm estimates (MNE) approach [79,80] to reconstruct the inverse EEG solutions. Figure 3.3 shows the locations of peak source activity (in dashed circles) as it traversed the cortical surface (first row), and the locations and orientations of the fitted dipoles used to obtain the single-trial source waveforms (second row). The earliest peak of cortical activity occurred in left SI at around 45 ms after stimulus onset, followed by activation in the right occipital region, in an area consistent with the location of the lateral occipital complex (LOC) at 130 ms, and then in the location of the right posterior intraparietal sulcus (pIPS) at 160 ms. Finally, at 175 ms, activation was seen in left dlPFC. Table 3.1 lists the ERP source locations, dipole orientations of the source model and activation time of cortical sources. The fitted dipoles at locations and orientations shown explained approximately 82% of the variance in the EEG signal for trials with correct responses.

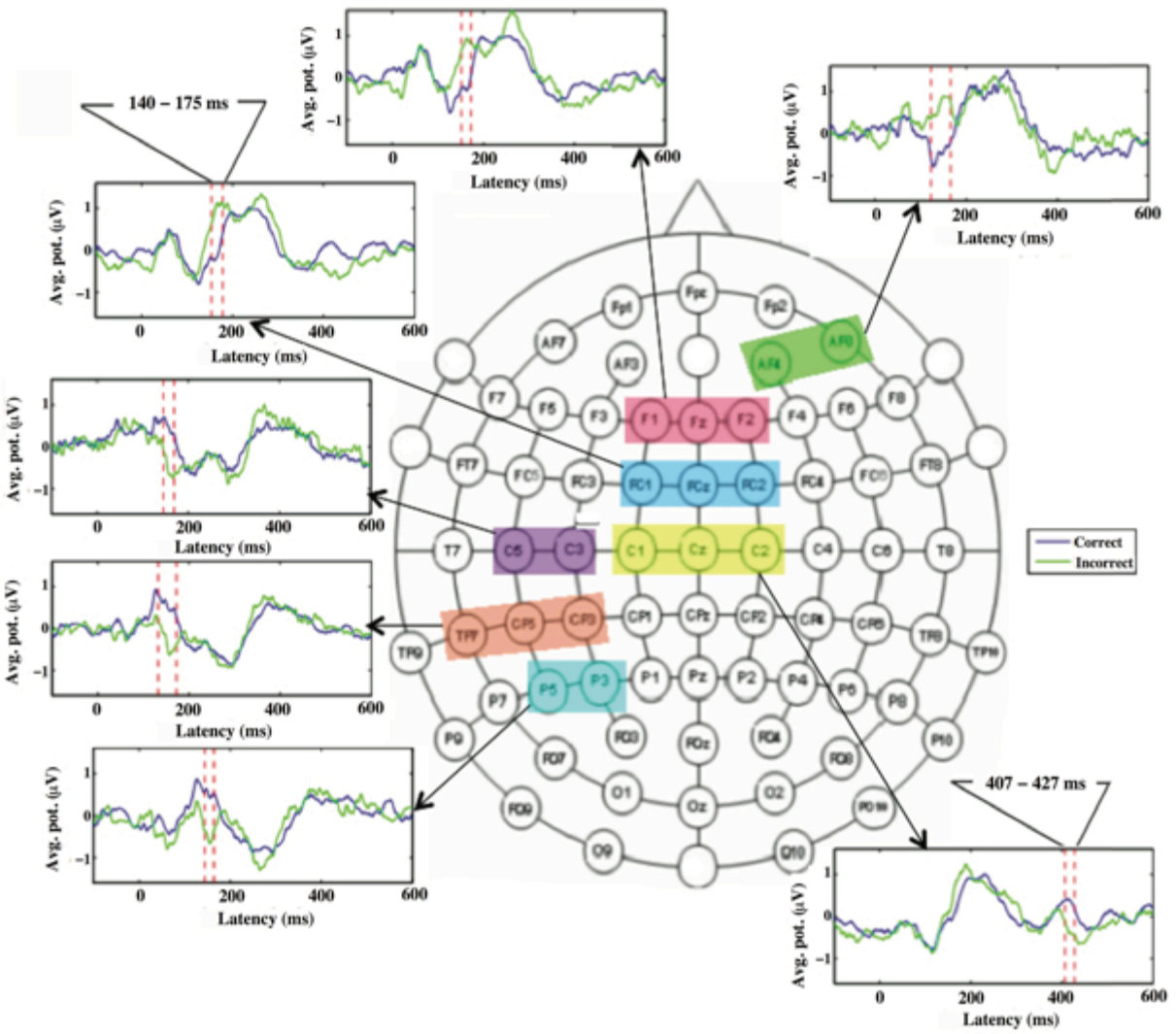

Figure 3.2 **Event-related potentials (ERPs).** The shaded regions covering two or three labeled circles, in the 68-electrode EEG recording montage, show the locations in sensor space where ERPs differed significantly for trials with correct and incorrect responses in the approximate timeframe 130 - 175 ms. The average waveforms, at representative sites from the shaded regions, are also shown for correct and incorrect responses.

Power spectra: Figure 3.4 (A-B) shows how source-level power in the beta- (12 - 30Hz) and gamma band- (30 - 100 Hz) frequency bands varied in the network nodes (SI, LOC, pIPS and dlPFC) during earlier (30 - 140 ms) and later (140 - 210 ms) periods of trials associated with correct responses. Significant power changes are detailed in Table 3.2. SI showed a significant

decrease in power over time in both bands. In contrast, power in both pIPS and dlPFC increased in the gamma band but decreased in the beta band over time. LOC spectral power did not change significantly over time.

Table 3.1: The anatomical location, dipole orientation (components) and activation timeframes of localized sources obtained for correctly perceived stimuli using the minimum-norm estimate (MNE) approach.

Regions	**Talairach coordinates (mm)**			**Dipole orientation (components)**			**Activation time (ms)**
	x	**y**	**z**	**x**	**y**	**z**	
Primary somatosensory cortex (SI)	**-43.1**	**-23.4**	**59.6**	**0.6**	**0.2**	**0.8**	**40 - 50**
Lateral occipital complex (LOC)	**51.6**	**-57.3**	**-9.1**	**-0.6**	**-0.4**	**0.6**	**118 - 132**
Posterior intraparietal sulcus (pIPS)	**21.9**	**-44.6**	**66.4**	**-0.5**	**0.6**	**0.7**	**150 - 170**
Dorsolateral prefrontal cortex (dlPFC)	**-23.5**	**24.5**	**52.4**	**-0.3**	**-0.5**	**0.8**	**160 - 210**

Table 3.2: The significance level (p-value and corresponding t - value in parentheses, marked in boldface) for spectral power differences between later (140-210 ms) and earlier (30-140 ms) periods during correct responses (obtained from paired t-tests).

Regions	beta band (12 - 30 Hz)	gamma band (30 - 100 Hz)
Primary somatosensory cortex (SI)	**1.86×10^{-4} (-5.83)**	**6.3×10^{-4} (-5.42)**
Lateral occipital complex (LOC)	0.14 (1.61)	0.08 (-1.95)
Posterior intraparietal sulcus (pIPS)	**1.17×10^{-4} (-6.95)**	**5.5×10^{-3} (3.77)**
Dorsolateral prefrontal cortex (dlPFC)	**3.49×10^{-4} (-5.93)**	**4.0×10^{-4} (5.80)**

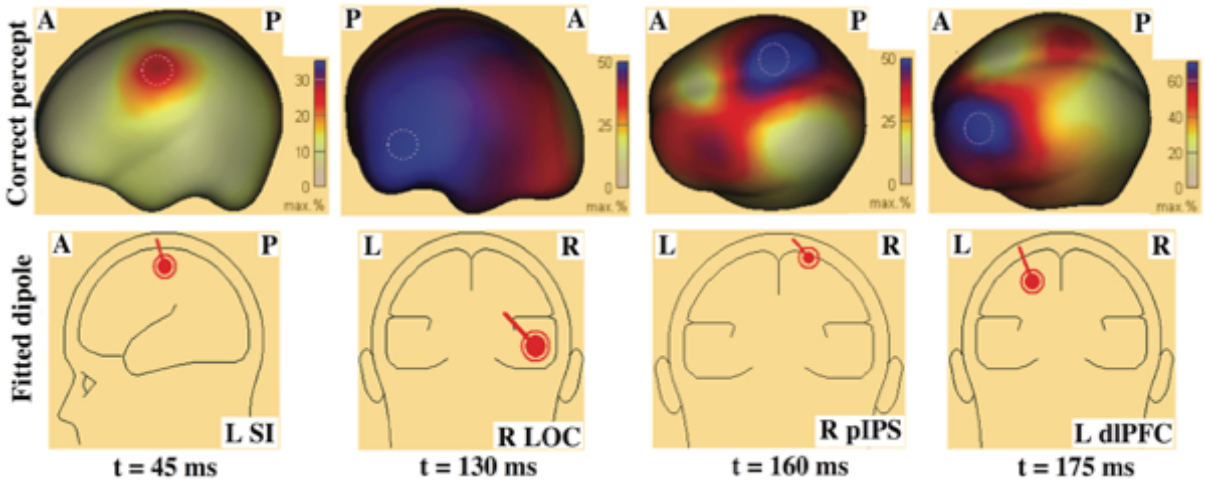

Figure 3.3 **Spatiotemporal profiles of peak source-level electrophysiological activity during trials with correct responses.** The top row represents minimum-norm estimate (MNE) sources with peak activity over L SI at 45 ms, R LOC at 130 ms, R pIPS at 160 ms and L dlPFC at 175 ms. The bottom row represents the corresponding fitted dipoles with their orientations. Abbreviations as in text.

Coherence spectra: Beta band coherence between the node-pairs SI-LOC, LOC-pIPS, SI-pIPS and pIPS- dlPFC was significantly higher for correct compared to incorrect responses ($p<0.01$) (not shown) and for the later period in comparison to the earlier period ($p<0.05$) [Figure 3.4(C)]. In contrast, beta band and gamma band coherences decreased over time for the SI-dlPFC node-pair ($p<0.05$). Gamma band coherence between pIPS and dlPFC was significantly higher for the later period in comparison to the earlier period ($p<0.05$) [Figure 3.4 (D)]. Gamma band coherence between pIPS and dlPFC during trials with correct responses was significantly higher than that in trials with incorrect responses, from as early as 117 ms and lasting until 158 ms (see Appendix A and Figure A6 therein).

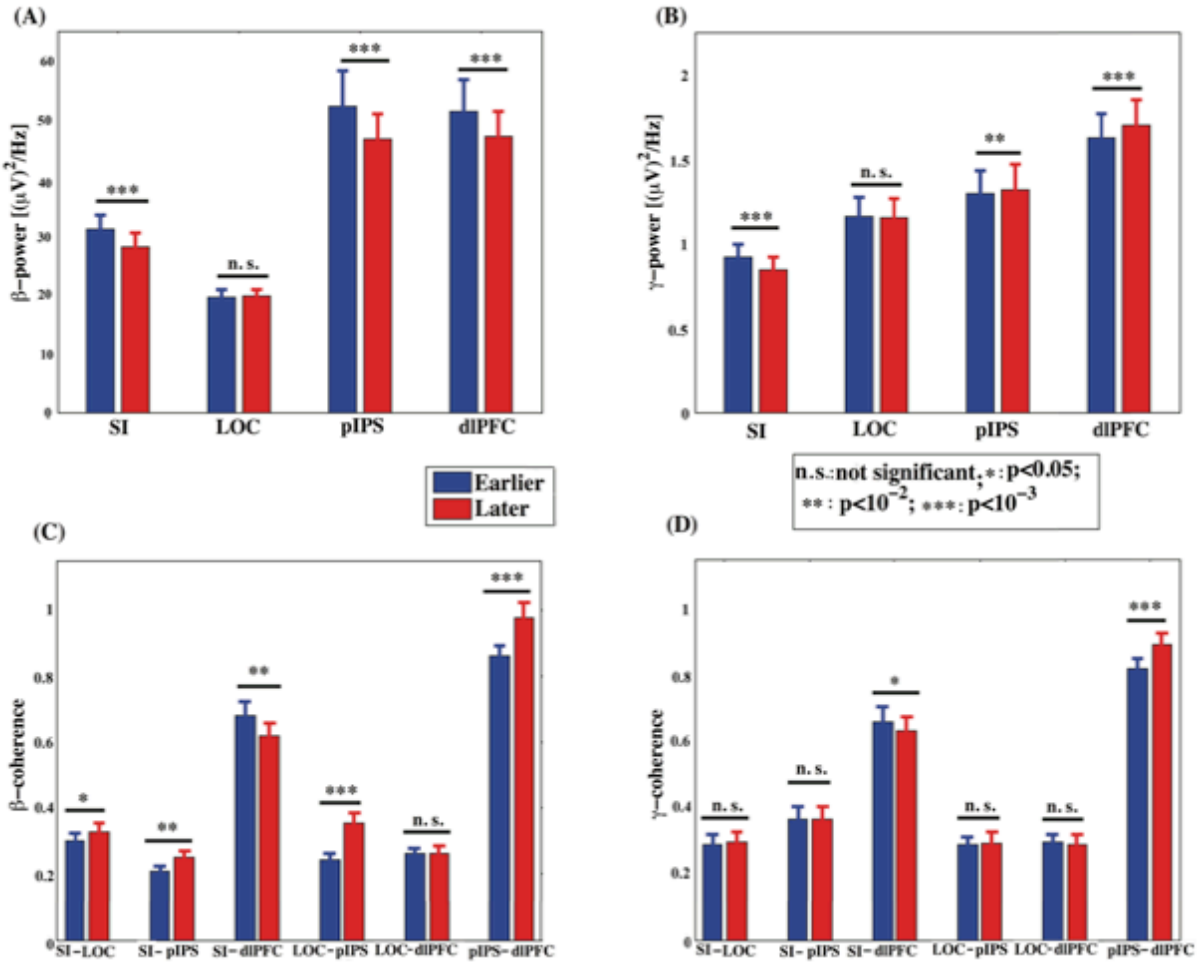

Figure 3.4 **Spectral power and coherence.** Beta band (12- 30 Hz) (A), and gamma band (30-100 Hz) (B) spectral power during earlier (30-140 ms) and later (140 – 210 ms) periods for correct response trials. Power increases occurred only in the gamma band activity of pIPS and dlPFC. (C-D). For correct responses, pIPS-dlPFC coherence increased significantly in the later period for both β and γ**.** Error bars are standard error of the mean (S.E.M.).

Beta band and gamma band Granger causality spectra: We computed Granger causality spectra to assess oscillatory network interactions among the four nodes of activity: SI, LOC, pIPS and dlPFC. Because of the frequency band-specific relevance of oscillations in perceptual

decision-making [19], we computed Granger causality spectra and separated the spectra into beta (12-30 Hz) and gamma (30-100 Hz) bands (Figure A1 in Appendix A shows some of the results

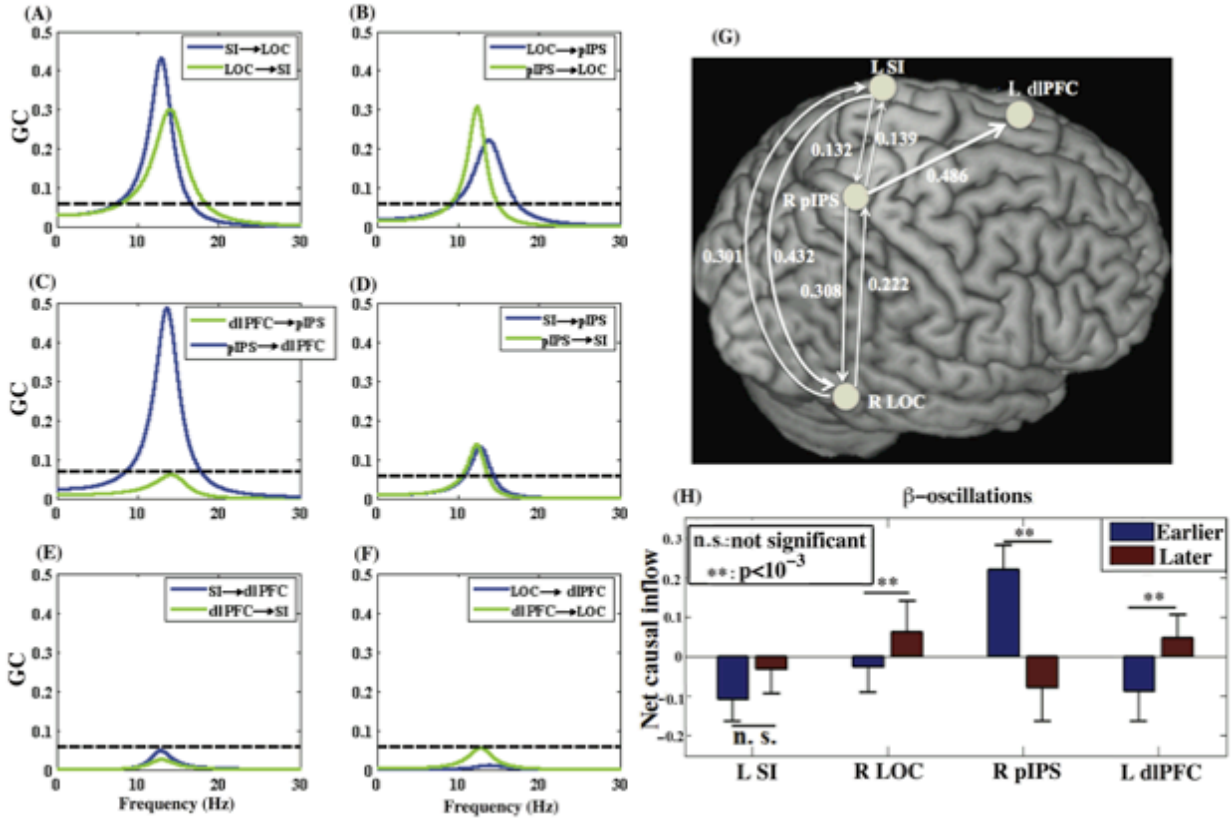

Figure 3.5 **Granger causality and net causal flow in the frequency range (0 – 30 Hz).** (A-F) Granger causality spectra when participants responded correctly; the peak causal influence is seen at roughly 13-16 Hz (low beta range). Significance thresholds (shown by dotted lines) as in text. (G) Schematic representation of the beta band Granger causality network graph associated with correct responses, based on the bivariate (pairwise) and trivariate (conditional) Granger causality results. (H) Significant ($p<0.001$) changes in net causal inflow between earlier and later durations. Error bars are standard error of the mean (S.E.M.).

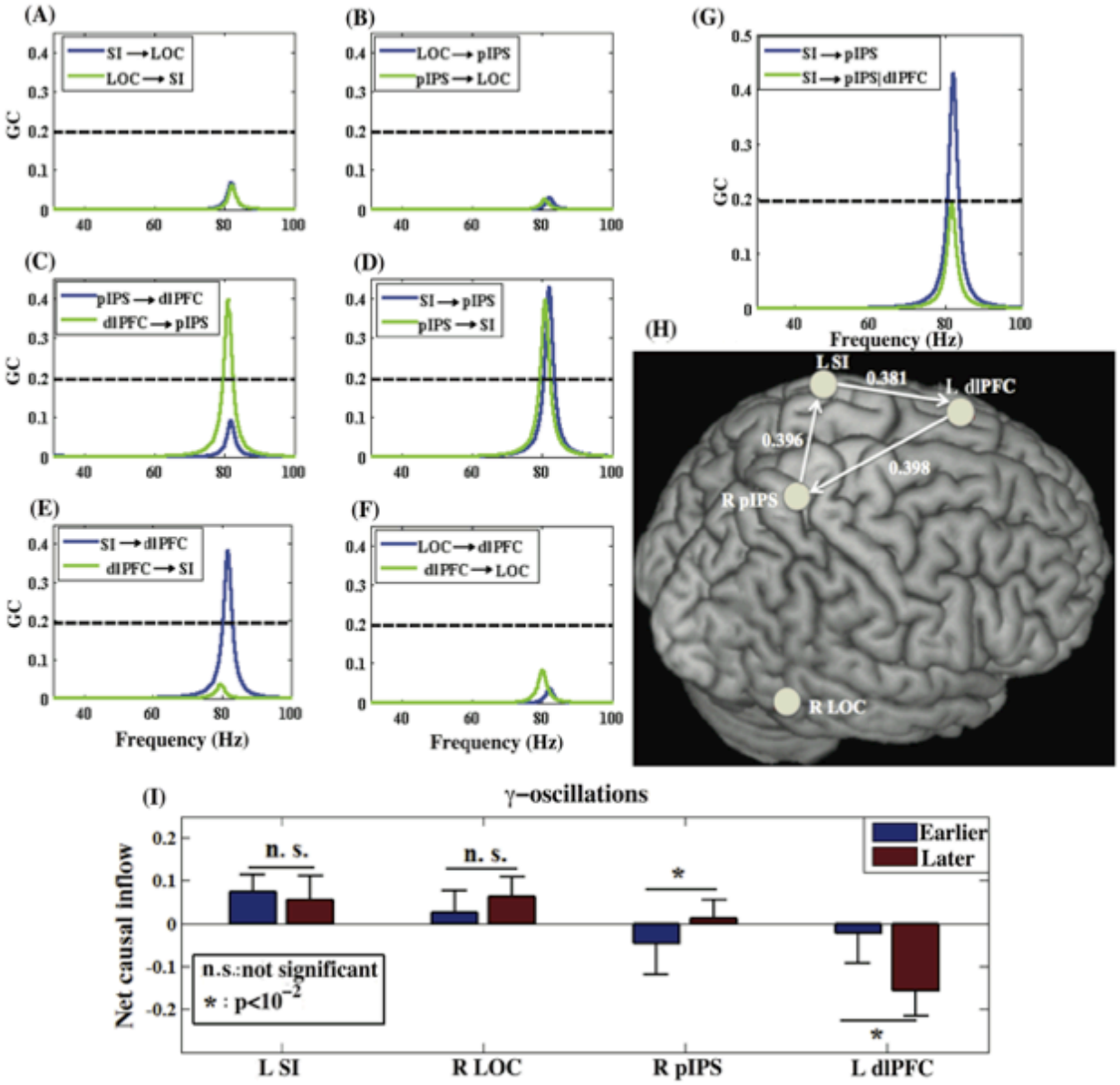

Figure 3.6 **Granger causality and net causal flow in the gamma band (30 – 100 Hz).** (A-F). Granger causality spectra when participants responded correctly. Significance thresholds (shown by dotted lines) as in text. (G) The conditional Granger causality spectra SI→pIPS|dlPFC (means SI to pIPS after factoring out mediation through dlPFC) (green line). (H) Schematic representation of the gamma band network activity associated with correct responses based on the bivariate and trivariate (conditional) Granger causality results. (I) Changes in net causal inflow (total incoming causal flow minus total outgoing flow for a node) between earlier and later durations. Error bars are standard error of the mean (S.E.M.).

from a participant before separating frequency band-specific activities). To better assess the spectral specificity and temporal evolution of neuronal effects, we also performed time-frequency analyses separately for both beta and gamma band oscillations and examined the power spectra, coherence spectra and Granger causality spectra (see Appendix A and Figures A7-A8 therein for details).

Figure 3.5 (A-F) shows Granger causality spectra in the beta band and the net causal flow for the four-node network as a function of frequency within the beta band associated with correct responses. In this band, there was bidirectional information flow between each of the three node-pairs involving SI, LOC and pIPS. Among these regions, the LOC received comparatively stronger influences from the pIPS and SI compared to outflow to these regions. The causal influence was unidirectional from the pIPS to dlPFC. The Granger causality spectral peaks occurred around 15 Hz. The dominant information flow here was, overall, consistent with the pattern of temporal evolution of the MNE source activation shown in Figure 3.3 (see Appendix A and Figure A3 therein for further details of dominance in flow patterns). Figure A4 shows the absence of organized feedforward or feedback network activity in the absence of task performance (prestimulus durations). We performed conditional Granger causality analysis to rule out mediated interactions between all possible node-pairs. Figure 3.5 (G) shows the Granger causality network graph associated with correct responses. Figure 3.5 (H) shows the net beta band causal flow in the earlier and later epoch at each node. The pIPS functioned predominantly as a target in the earlier period with the LOC and dlPFC functioning mainly as sources; this pattern reversed in the later epoch. SI functioned as a source in both epochs, without a significant change in net causal flow over time.

Similarly, we also evaluated the patterns of pairwise and conditional Granger causality and

net causal inflow in the gamma band (Figure 3.6). Gamma band frequency oscillations around 80 Hz held SI, pIPS and dlPFC in the network while the LOC was excluded. Causal influence was directed from SI to dlPFC to pIPS and back to SI as a closed loop during correct responses [Figure 3.6 (H)]. The interaction from SI to pIPS was found to be mediated through dlPFC, since the causality from SI to pIPS after factoring out mediation through dlPFC (SI→ pIPS|dlPFC) [Figure 3.6 (G)] was not significant. As shown in Figure 3.6 (I), there were significant causal inflow differences between the earlier (30-140 ms) and later (140-210 ms) epochs in the pIPS and dlPFC (Table 3.3). The pIPS functioned mostly as a source of information flow in the earlier timeframe but as a target in the later timeframe, whereas the dlPFC became a more dominant source over time. SI and LOC showed no significant changes over time. These results of spectral peaks obtained from single trial waveforms after removing stimulus-triggered averages showed excellent agreement with the spectral quantities computed from the single trials after removing ensemble averages using the ASEO-method [88] (see Figure A2 for the spectral power and causality computed from the ASEO-method treated trials). Following the method of time-shifted surrogates used in previous studies [89,90], we verified that these networks were not affected by any residual volume conduction in reconstructed source signals (see Appendix A for additional information and Figure A5 therein for details).

Brain-behavior relation: Behavioral accuracy (expressed in z-score) was found to be significantly positively correlated with measures of network activity in both beta and gamma bands. The performance was correlated with beta band coherence for SI-LOC, and pIPS- dlPFC [as shown in Figure 3.7 (A-B)] and with gamma band coherence for pIPS-dlPFC and SI-dlPFC [Figure 3.7 (C-D)]. Similarly, behavioral accuracy was also correlated with beta band Granger causality from pIPS to dlPFC [Figure 3.8 (A)] and with gamma band Granger causality from

dlPFC to pIPS, and SI to dlPFC [Figure 3.8 (B-C)]. All the results of brain and behavior relationships are shown in Figures A9-A12.

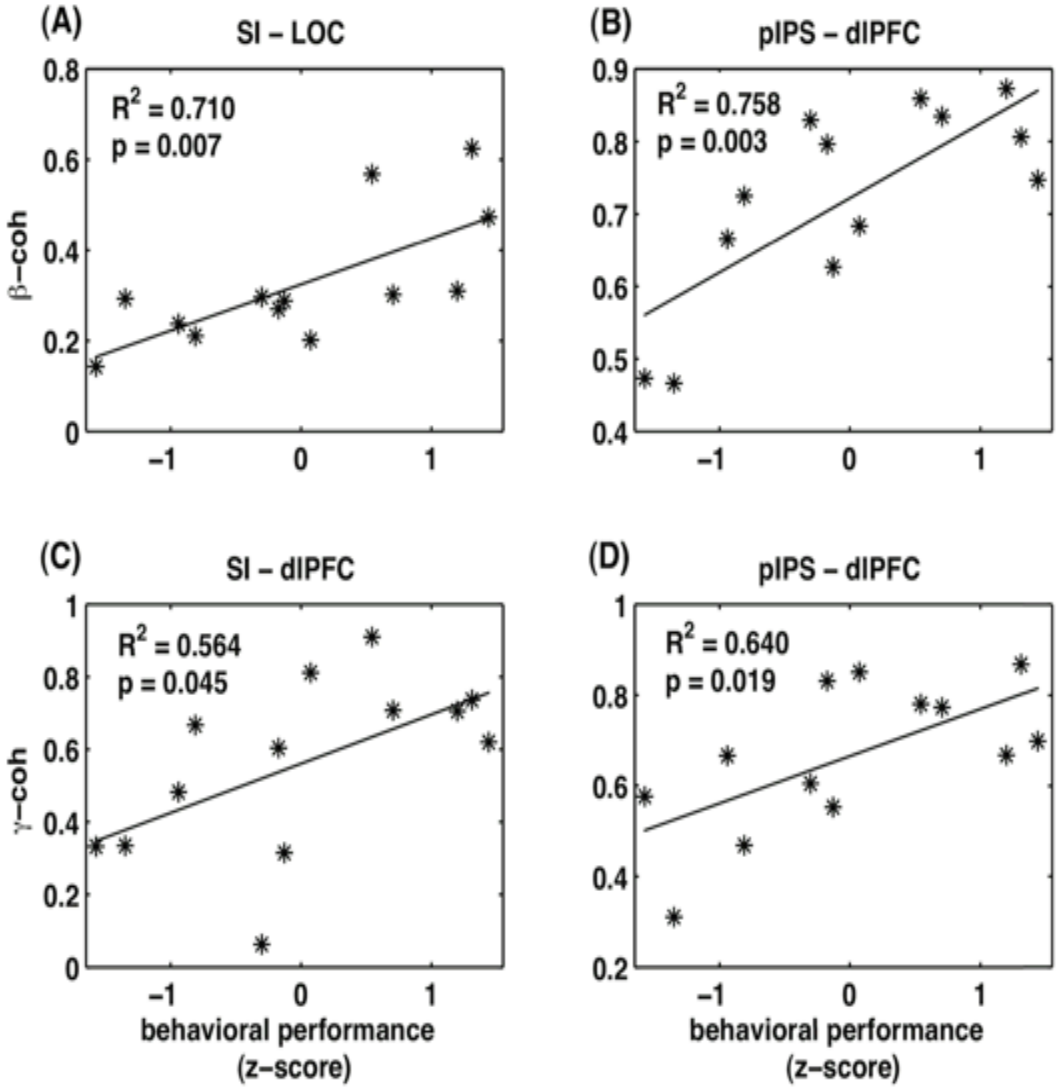

Figure 3.7 **Relation between coherence and behavioral performance.** Pairs of nodes showing positive correlations of beta band (A-B) and gamma band (C-D) coherence with behavioral performance ($p < 0.05$).

Table 3.3: The p-value and corresponding t - value (in parentheses) with significance denoted by boldface, for spectral power differences between later (140-210 ms) and earlier (30-140 ms) periods during correct responses (obtained from paired t-tests).

Regions	beta band (12 - 30 Hz)	gamma band (30 - 100 Hz)
Primary somatosensory cortex (SI)	**1.86×10^{-4} (-5.83)**	**6.3×10^{-4} (-5.42)**
Lateral occipital complex (LOC)	0.14 (1.61)	0.08 (-1.95)
Posterior intraparietal sulcus (pIPS)	**1.17×10^{-4} (-6.95)**	**5.5×10^{-3} (3.77)**
Dorsolateral prefrontal cortex (dlPFC)	**3.49×10^{-4} (-5.93)**	**4.0×10^{-4} (5.80)**

3.4 Discussion

Fine tactile discrimination involves somatosensory processing, focusing attention on stimulus features, encoding the acquired sensory information, visualizing the stimulus features, and eventually forming decisions expressed in motor responses, as elaborated in previous studies [66,67]. Here, we obtained two important results that point towards unifying principles consistent with the sequence of these processes. First, ~15 Hz beta network oscillatory activity was dominantly feedforward from somatosensory to occipital to parietal to prefrontal regions, similar to the propagation of average cortical activity, probably reflecting accumulation and maintenance of sensory information. Second, ~80 Hz gamma network oscillations occurred in a recurrent closed loop from prefrontal to posterior parietal to somatosensory and back to prefrontal regions, implying involvement of this loop in attentional selection of task-relevant sensory evidence. Accuracy of tactile discrimination was significantly correlated with measures of network activity in both bands. These results provide direct evidence of recurrent information processing of sensory

and attentional signals as in somatosensory awareness [91] and in other forms of decision-making [92,93]. These findings, together with previous studies in the visual [19] and auditory-visual domains [20] suggest common oscillatory network mechanisms for perceptual decision-making across various sensory modalities. Further, these results are consistent with earlier fMRI studies of somatosensory perception: An fMRI study [69] with a similar stimulation protocol to this

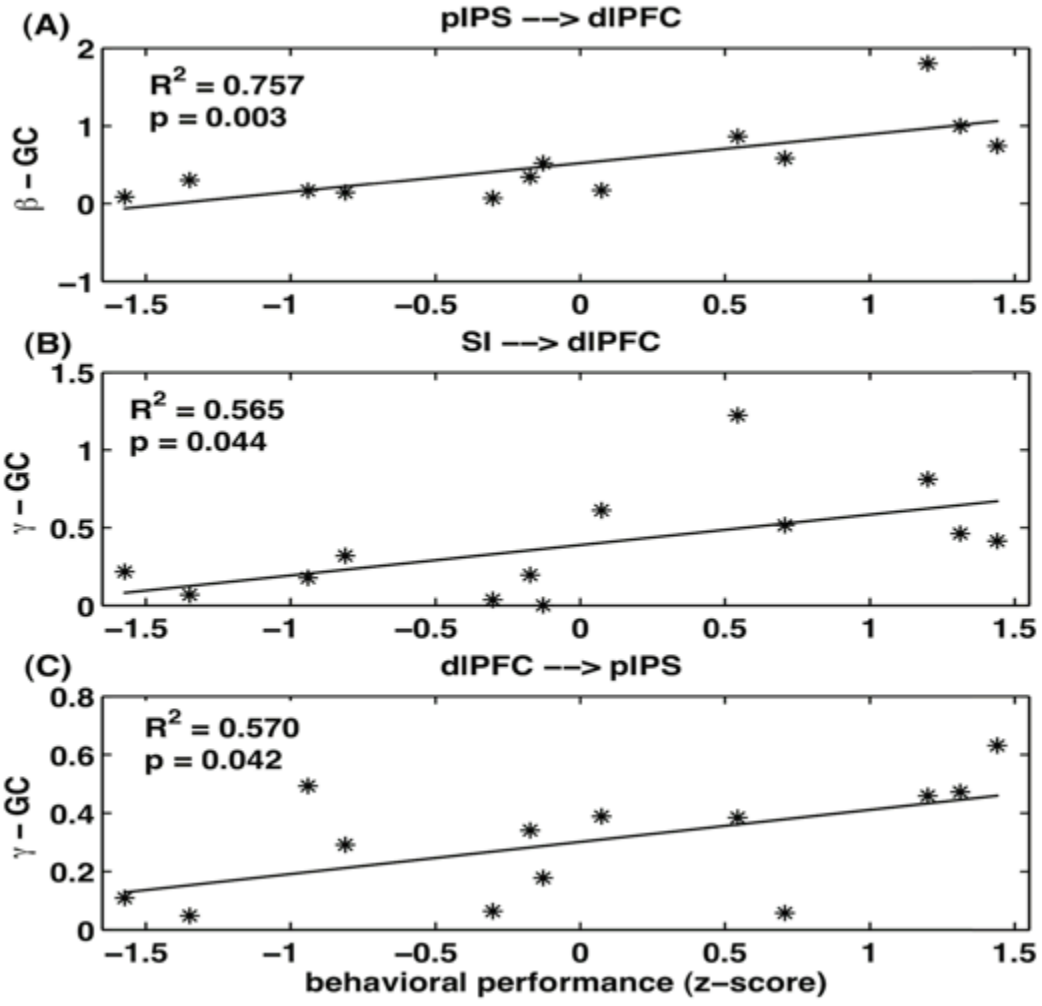

Figure 3.8 **Relation between Granger causality and behavioral performance.** Beta band (A) and gamma band (C-D) Granger causality relationships among node pairs ($p < 0.05$).

study found that the paths predicting acuity converged from the left postcentral sulcus (PCS) and right frontal eye field (FEF) onto the right pIPS, consistent with interaction between feedforward somatosensory signals and feedback control signals. Similarly, other fMRI studies on haptic perception revealed evidence for both bottom-up projections from somatosensory cortex and top-down paths from prefrontal and parietal cortex to the LOC [94-96]. Our results provide a new understanding of the role of oscillatory interactions within these somatosensory and frontoparietal networks during tactile perceptual decision-making.

3.4.1 Cortical sources of neural activity

Sensor-level brain responses associated with correct and incorrect perception differed around 130-175 ms after stimulus onset. MNE-localized cortical sources from these responses propagated from left SI at around 45 ms to the right LOC at 130 ms, to the right pIPS at 160 ms and finally to left dlPFC at 175 ms, outlining a feedforward sweep. Contralateral SI activation within the 30-50 ms timeframe is consistent with a previous ERP study [97] for tactile stimuli varying in shape. The LOC is known for visuo-tactile convergence of information relating to object shape [98-101]. The right LOC activation found here at around 130 ms could be associated with visualizing tactile stimulus features [97]. Previous studies have found LOC activation more consistently in the right hemisphere [69,100-103]. As for SI, the right pIPS and left dlPFC activations were somewhat delayed relative to those observed with electrical stimulation of the median nerve [71-75], which excites peripheral afferents synchronously at a more proximal location. The pIPS activation may reflect the role of posterior parietal cortex in tactile perception [69,96,100] and spatial attention [104,105]. Activation seen in left dlPFC at around 175 ms may indicate a role for this region in working memory (WM), or in encoding and maintaining decisions [106,107] until a motor response is generated.

Processing of either consciously perceived stimuli [108-110] or imperceptible sensory stimuli [110-113] involves a widespread network, including SI [110-113] and several areas higher in the processing hierarchy [111,114,115]. The data of the present study suggest that the neural correlates distinguishing correct percepts from incorrect percepts emerge at later stages and higher levels of sensory processing, after ~140 ms. Hence our results not only support the notion that early SI activation is insufficient to distinguish trials with correct from those with incorrect responses, but also shows that processing of these trial types differs significantly starting around ~140 ms after stimulus presentation when the signal is processed in parietal and frontal cortices [116].

3.4.2 Oscillatory power

We observed ~15 Hz (beta band) and ~80 Hz (gamma band) spectral power peaks 30-210 ms after stimulus onset. These oscillations reflect distinct aspects of synchronization among neuronal populations during perception, attention and memory maintenance [117,118] and are observed during a variety of processes, including those associated with somatosensation, WM and attention [19,119-121]. Spectral power differed before and after 140 ms in all regions except LOC (Fig. 3.4). SI demonstrated a decrease in power in both beta and gamma bands, whereas both pIPS and dlPFC showed gamma band increases but beta band decreases. Gamma-power increases in pIPS and dlPFC during trials with correct responses could be due to changes in attentional control, working memory maintenance and verbal encoding of decision reports [122]. Gamma power increase with a concomitant beta power decrease compared to the baseline was also observed in a tactile delayed-match-to-sample task [119]. The gamma and beta power changes observed here in pIPS and dlPFC between different phases of the tactile decision-

making task could be due to a change in level of top-down attentional control [105] and a change in WM maintenance to update WM contents [121].

3.4.3 Oscillatory network activity

Coherence and Granger causality spectral analyses showed that inter-areal brain synchronization and interactions during a tactile perceptual decision-making task were consistent with mediation by ~15Hz beta band and ~80 Hz- gamma band neural oscillations. Measures of network activity, especially those pertaining to the dlPFC in both bands, were significantly correlated with the accuracy of task performance (Figure 3.7 and Figure 3.8). These frequencies (15 Hz and 80 Hz) of oscillatory activity are close to the ones observed in an EEG study of multisensory perception [20]. The beta band network in our study included all four active nodes in somatosensory, lateral occipital, parietal and prefrontal cortex while the gamma band network excluded the lateral occipital cortical node but included the other three. A similar beta oscillatory network was observed in a somatosensory-motor task [86] and in a WM task [123]. The parietal and prefrontal coherence in the gamma band increased over time, consistent with a well-known role of gamma oscillations in perceptual binding [4,124]. The information flow at ~15 Hz was dominantly feedforward, reflecting sensory-driven processes. On the other hand, ~80 Hz gamma band information flow was directed in a recurrent loop from dlPFC to pIPS to SI and SI to dlPFC, implying involvement in attentional selection of relevant sensory information and sensory updating. These results of organized oscillatory network activity are based on the analysis of post-stimulus brain activity. The pre-stimulus periods lacked the same level of organization (see Figure A4 in the Appendix A). However, the pre-stimulus brain activity can be modulated by top-down attention, which has been shown in the somatosensory domain [125] and in the visual domain [126,127]. The inter-areal and laminar neural circuitry in the brain support the natural occurrence of gamma

and beta oscillatory activities and their modulations in cognitive and perceptual tasks that engage top-down attentional control signals [49].

To summarize, the present study extends our understanding of the neocortical dynamics underlying perceptual decision making in the somatosensory domain, with regard to the time frame of averaged evoked potentials and the fast oscillatory networks that appear to organize evoked activity across widespread cortical regions. We found that fine tactile discrimination is mediated by distinct but overlapping ~15 Hz beta and ~80 Hz gamma band large-scale oscillatory networks. The beta-network was dominantly feedforward from somatosensory to lateral occipital to posterior parietal to dorsolateral prefrontal cortex, similar to the propagation of average cortical activity, implying its role in accumulating and maintaining relevant sensory information and mapping to action. The gamma band network activity, occurring in a recurrent loop from the prefrontal to posterior parietal to somatosensory and back to prefrontal cortex, likely carried out attentional selection of task-relevant sensory evidence. Measures of network activity in both bands were correlated with accuracy of task performance. These findings provide important insights into the neural mechanisms that mediate fine tactile spatial discrimination of the kind that is necessary for Braille reading.

4 LOCALIZING EPILEPTIC SEIZURE ONSETS WITH GRANGER CAUSALITY

4.1 Introduction

Of 2**.** 5 million people with epilepsy in the United States, at least 30% have seizures such as refractory temporal lobe epilepsy that cannot be controlled with medication, and are therefore potential candidates for epilepsy surgery [61,128]. But 10%–40% of patients who undergo pre-surgical evaluation have seizures that are not localized by the use of scalp electroencephalography (EEG), multimodal imaging, and magnetoencephalography (MEG). Many of these patients undergo intracranial electroencephalography (IEEG) recording with grid and depth electrodes. However, the increasing numbers of electrodes implanted by neurosurgeons in recent years, often totaling over 100 per patient, have not always produced greater clarity. Sampling of the seizure onset zone may still be incomplete. IEEG seizures may appear nonlocalized by conventional visual standards. Complete resection or disconnection of an apparent, nonlesional, extratemporal focus leads to a cure in less than 50% of cases. Traditional criteria for the estimation of IEEG seizure onset may be inadequate for many patients.

A conventional evaluation for epilepsy surgery uses IEEG to record a number of seizures, typically three to ten, over a period of 1–4 weeks during an inpatient stay in the epilepsy-monitoring unit. From the recorded information, the epilepsy monitoring team and neurosurgeons try to estimate the seizure onset zone (SOZ) in preparation for surgery. Suggested methods for the evaluation of IEEG include extending expert analysis of conventional visual EEG frequencies to direct current (dc) shift to high beta (20–30 Hz) to gamma (30–100 Hz) frequencies, and more recently to interictal high-frequency (> 80 Hz) oscillations (HFOs) [62-64]. Epilepsy surgery restricted mainly to the brain regions of HFOs has often lead to seizure freedom [63,129]. However, HFOs are also commonly observed in a normal brain state [64]. Various

measures (linear and nonlinear, univariate and bivariate) have been used to discriminate a preictal state from an interictal period [130]. The univariate methods have not always been sufficient in identifying the crucial ictal portion. The bivariate methods used so far have not been able to reveal the importance of high-frequency network activity in localizing epileptic seizure onsets. Nonlinear time series techniques have been mostly applied to predict seizures from the ictal activity of brain potential recordings [102,103,118,131-133]. However, the suitability of nonlinear measures to characterize brain potential recordings in predicting seizures has been questioned [122,134].

The activity of pathological neuronal systems and their network interactions lie at the heart of epileptic seizure and its propagation over the brain [61]. Current IEEG monitoring practice is still in the process of realizing the underlying network mechanisms of the generation and propagation of epileptic seizures. A limited number of studies have applied network correlational measures such as correlation and coherence to epilepsy data [85,86,135,136]. Here, considering neuronal network dynamics and HFOs at the heart of seizure generation and propagation over the brain, we applied multivariate spectral interdependency techniques to IEEG recordings of eight patients, including the directional measure Granger causality (GC), and assessed their effectiveness in the localization of seizure onset times and zones.

Fourier and wavelet transform-based nonparametric methods were recently extended to obtain Granger causality spectra [56-58]. Granger causality spectra can be used to examine the strengths, directions, and frequencies of interactions between oscillatory stochastic processes. Clive J. Granger, 2003's Nobel Laureate in Economics, had formulated the statistical definition of time-domain causality between two jointly stationary processes in 1969 using a parametric modeling scheme of time series data [137,138]. The frequency-domain Granger causality under

the same parametric estimation approach was proposed by Geweke in 1982 [59]. The parametric and nonparametric approaches to spectral analysis of time series data are complementary to each other [56,57]. We used both parametric and nonparametric approaches for optimal estimation of spectral quantities such as power, coherence, and Granger causality from spatially distributed IEEG recordings. We also computed total interdependence (TI) by integrating coherence over the entire frequency range [59,84] and net causal outflow (OF) associated with each recording electrode. With these measures, we evaluated where and when seizures started and how they propagated over the recording electrodes implanted in the subdural space and directly within the brain.

4.2 Materials and methods

4.2.1 Patient selection

IEEGs were analyzed from eight patients who had undergone electrode implantation between 2010 and 2012, using combinations of standard depth electrodes and subdural grids, recording from a total of 40 -128 electrodes at a sampling rate of 500 Hz. Raw data was saved at a passband from dc to 500 Hz. Prior to digitization, analog data was passed through a type II Chebyshev filter with 3db point at 240 Hz. Patients were studied retrospectively, in order to examine the general features of spectral measures in IEEG. These records were chosen because seizures appeared to have a consistent pattern of propagation, in which the onset was nonetheless ambiguous in terms of visual criteria including classic EEG frequencies, dc shifts, and gamma activity. EEG segments for analysis ranged from 5 to 20 s in duration, chosen to proceed to earliest visual manifestation of the seizure, and extending to include its visible propagation to at least two electrodes. Additional samples were taken at earlier times if high-frequency GC could be detected at the onset of the initial data segment, and separate 8 samples were taken at times remote from

known seizures, to evaluate the possible presence of GC interictally. The spectral power, coherence and GC analyses were done on deidentified data without any specific assumptions about the seizure onset zones established by the clinical visual criteria.

In the prospective portion of the study, two patients were chosen based on the condition of ambiguous visual onset, i.e., ictal activity was consistent across multiple seizures but visual criteria for seizure onset were inadequate or contradictory. Additional information was considered important for surgical decision-making when a single definitive site of resection could not be selected on the basis of iEEG augmented by combinations of clinical semiology, 3T anatomic magnetic resonance imaging (MRI), positron emission tomography (PET), single-photon emission computed tomography (SPECT), magnetoencephalography (MEG), neuropsychological assessment, and/or functional MRI (fMRI) mapping. The Emory University Institutional Review Board approved this study.

4.2.2 Spectral interdependency measures

We applied spectral Granger causality analysis to IEEG recordings and computed wavelet power, TI, GC spectra, and OF spectra in moving time windows of length 0. 5 s (250 time points). Here, power provides us the information about the level of synchrony of the underlying neural system within a recording site, coherence about synchrony between the neuronal systems, and GC about the directed influence from one neuronal system to another. In this study, the net outgoing information flow away from the node (source) is represented by a positive OF and the net incoming flow towards the node (sink) is represented by a negative OF. This interpretation is valid within the same patient's data and fine temporal resolution. However, we think that very coarse temporal resolution of the recordings may lead to spurious causalities, as was indicated in previous studies [67,84,139].

4.3 Results

4.3.1 Retrospective cases

IEEG segments were selected from patients undergoing clinical evaluation for epilepsy surgery. These segments included clinically identified ictal (seizure) activities and preictal (before the seizure) activity. Figure 4.1 shows a sample of multichannel IEEG time series that includes a seizure event. In this case, the seizure was clinically determined to start at around 9 s, as marked by the green vertical line in Fig. 4.1.

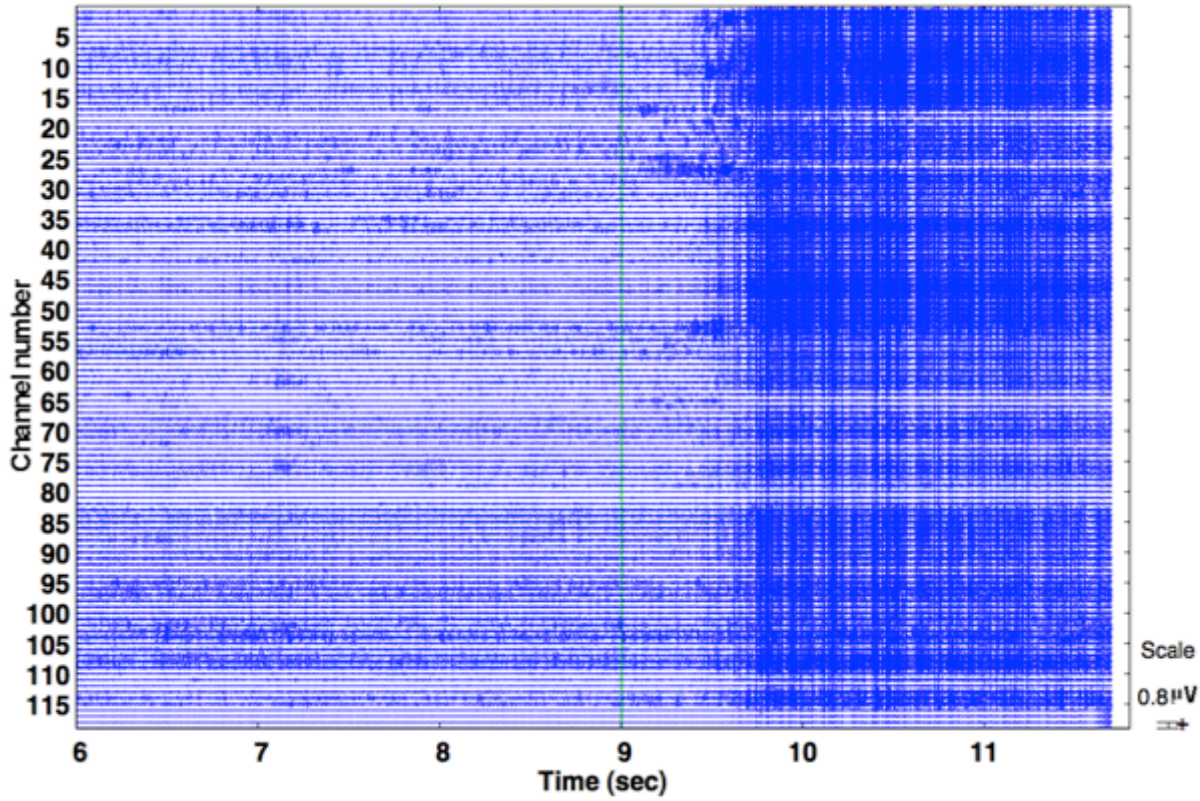

Figure 4.1 Sample time series: Multi-channel IEEG recordings with a seizure event in a patient. A green vertical line at t = 9.0 s marks the beginning time of a visually identified seizure event.

We computed wavelet power, coherence, TI, spectral and temporal GC, and net causal outflow OF as defined above from all patients separately. For this representative patient, these

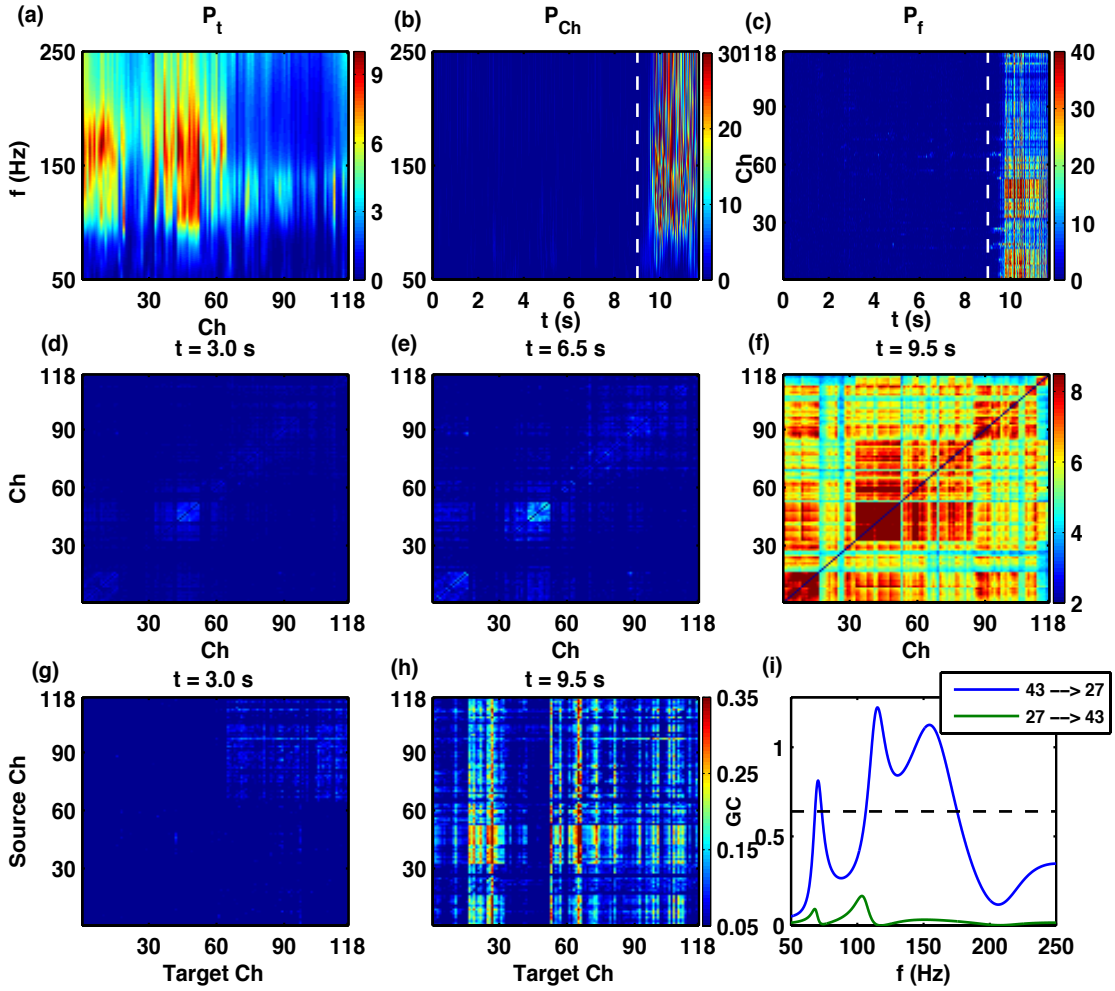

Figure 4.2 Spectral power averages, total interdependence (TI), and time-domain Granger causality (GC). (a)–(c) Wavelet power (z score) averaged over entire time (a), over recording channel (b), and over frequency (c). The white dashed lines in (b) and (c) represent the seizure onset times assessed by using traditional visual criteria. (d)–(f) TI at different times (t = 3.0, 6.5, and 9.5 s). In the ictal period (t = 9.5 s) the seizure has already spread to the entire network (f). (g)–(h) Time-domain GC in preictal period (t = 3.0 s) and the ictal period (t = 9.5 s). (i) Frequency-domain Granger causality spectra for two selected channels, 43 and 27, in which the former sends a dominantly stronger causal influence to the latter at around t = 9.5 s. The horizontal dashed line represents the threshold level at significance $p < 10^{-6}$, obtained by permutation tests.

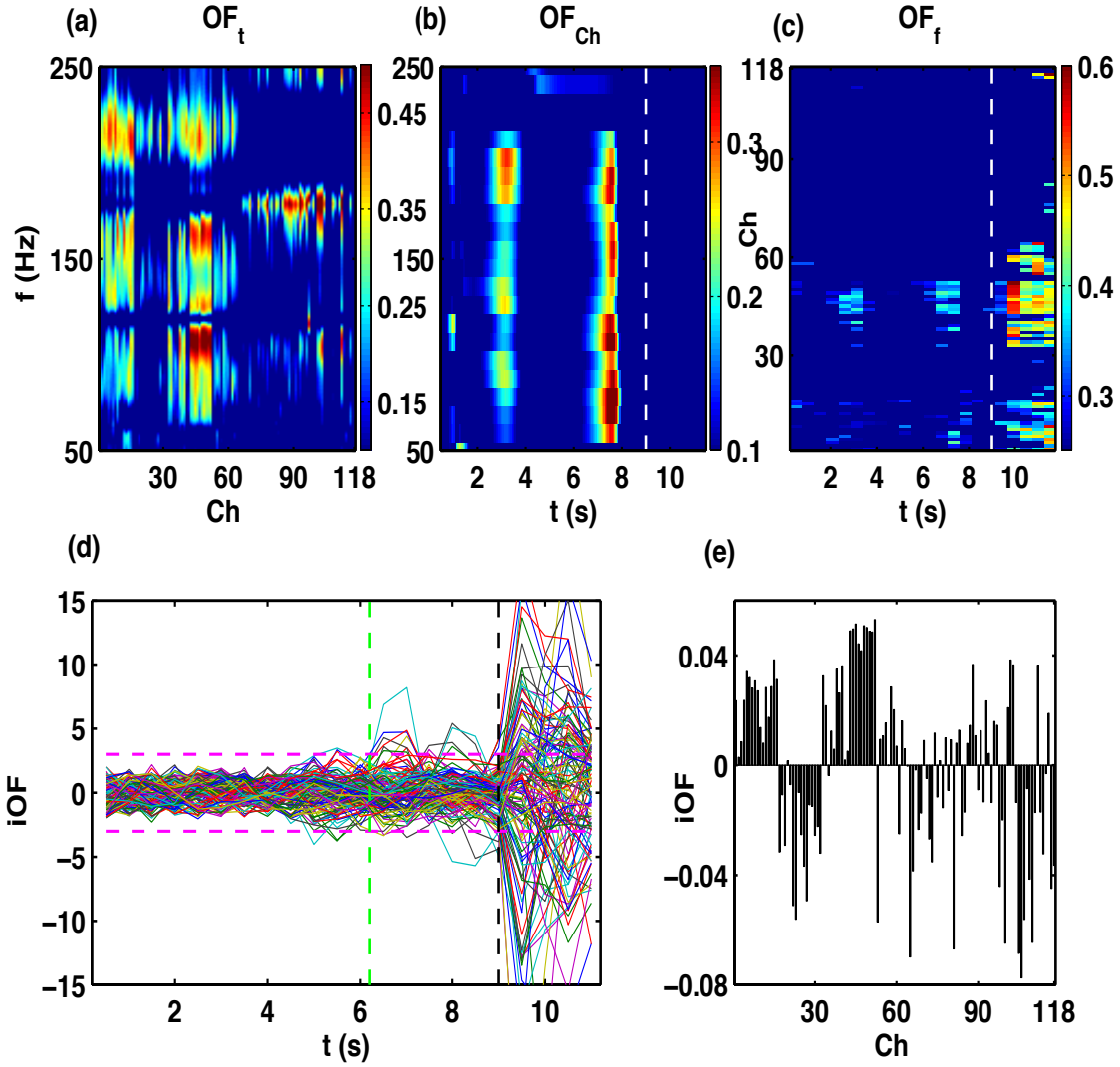

Figure 4.3 The net causal outflow (OF) averaged over entire time (a), over recording channel (b), and over frequency (c). The white dashed lines [(b) and (c)] represent the seizure onset times assessed by the traditional visual criteria. (d) Integrated net causal outflows (iOF, expressed in z score). iOF crosses three standard deviations (marked by horizontal dashed lines) ~3 s earlier (marked by a vertical green line at around 6 s) than the time assessed by using the traditional criteria (marked by a dashed black line). (e) iOF after the time of significant causality from all IEEG recordings of the same representative patient. Here, a channel with a positive value represents a causality source channel whereas one with a negative value represents a sink channel.

quantities are shown in Figs. 4.2 and 4.3. The wavelet power [Figs. 4.2(a) –4.2(c)] shows that there was high-frequency (~150 Hz) activity in a limited group of electrodes early during the seizure. Compared to t = 3. 0 s (preictal period) in Fig. 4.2(d) and t = 6. 5 s (~ seizure onset time from the GC approach) in Fig. 4.2(e), the whole network was affected by the seizure propagation at 9**.** 5 s (ictal period) as shown by TI [Fig. 4.2(f)]. A group of recordings (around channel 40) acted as strong sources of GC [Fig. 4.2(h)]. For instance, channel 43 was exerting a stronger causal influence to 27 than the other way around [Fig. 4.2(i)]. Figures 4.3(a) –4.3(e) show that the net causal outflow can identify the locations and time of seizure onset. Here, electrodes around channel 40 propagated high-frequency activities approximately 3 s before it was clinically recognized by using any visual criterion. The difference in the causal outflow between the times of seizure and before seizure for a strongest causality source remained positive for all patients P1–P8 (shown in Fig. 4.4). For individual outflow spectra from all patients and for further ***TI, iGC,*** *and* ***iOF*** results, please see the Appendix B. In all patients, high-frequency GC relationships could be defined among groups of electrodes prior to the onset of any visible ictal activity. GC calculation shows the seizure occurred anywhere between 2.0 and 12.5 s (mean ± standard error of mean = 6**.** 3 ± 1**.** 4 s) earlier than the time it was determined visually as determined by the 3 times the standard deviation (SD) criteria. For these seizure samples, the net causal outflow has exceeded 3 SD and the positive predictive value of this finding prior to visible seizure onset is 100%. For the interictal data, which was comparable in length to the ictal data far away from seizures, the net causal outflow never exceeded 2.5 SD. Here, the most striking finding was the frequent demonstration of strong causality at frequencies approaching 200 Hz. The clinicians in the epilepsy-monitoring unit were unable to visualize this activity using any combination of gain, time scale, and filter settings. Even on Fourier spectral graphs, it was detectable only by careful

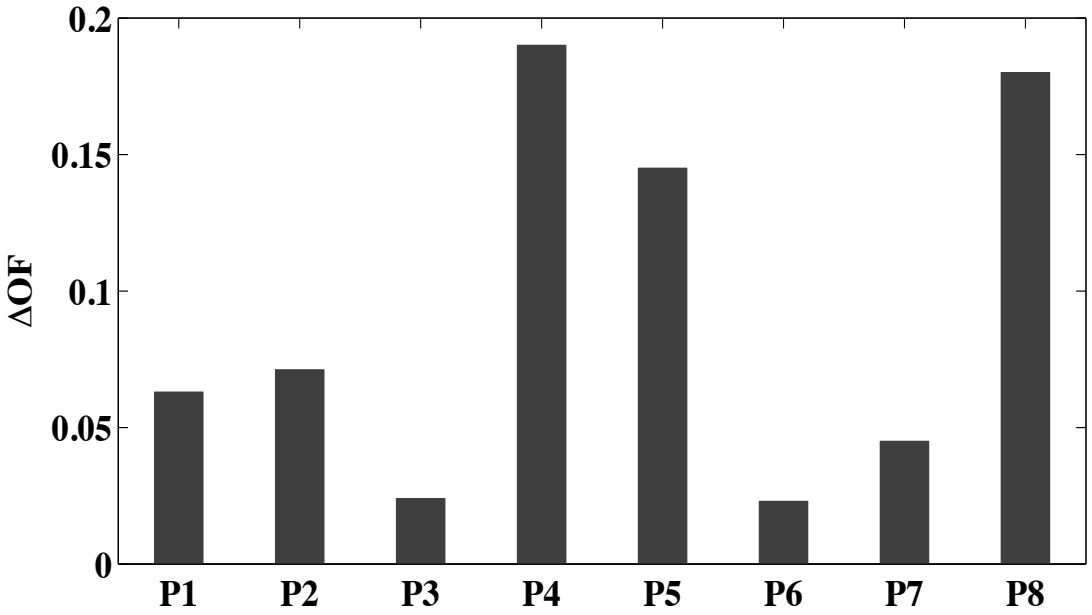

Figure 4.4 Integrated causal outflow differences (Δ**OF**) in a source channel between ictal and preictal periods in eight patients (P1–P8). Positive differences in all patients suggest that the causality can always increase in going from the preictal to the ictal periods.

adjustment of display parameters. These results show that high-frequency GC could often be defined among groups of electrodes long before the onset of any visible ictal activity.

4.3.2 Prospective cases

Prospective Case 1 was a 32-year-old left handed man with medically refractory partial seizures and secondary generalization of 3 year duration. MRI showed prominent right hippocampal sclerosis plus Dandy-Walker malformation, hyperplastic cerebellum, and numerous areas of heterotopic gray matter that were particularly prominent in the right posterior occipital and parietal regions. MEG localized interictal epileptiform activity to the right posterior perisylvian region. PET scan showed relative hypometabolism in the medial and inferior right temporal lobe.

Scalp EEG showed delayed onset of ictal activity in the right posterior temporoparietal region. Neuropsychological testing revealed cognitive impairment in the areas of verbal and spatial memory, naming, motor skills, information processing speed, and verbal fluency. IEEG recorded 8 clinically and electrographically stereotyped seizures with earliest visible onset in the form of fast narrow spikes and beta activity from a single right occipital grid electrode, ROg61, which was otherwise remote from all other early ictal discharges in the temporal lobe. ROg61 was followed by HFOs involving electrodes in right anterior and mid-temporal strips, the latter evolving to ictal beta and then more widespread ictal discharges (Figure 4.5A). In this case, we used GC to test a simple binary hypothesis concerning electrode ROg61: that it was either a causal source or sink in relation to the sampled electrodes in RAsT and RMsT (Figure 4.5 (B-C)). The GC result indicated that ROg61 was in fact a causal sink among these electrodes, with the strongest causal source being RAsT5. Based in part on this result, we chose to ignore the early discharge in ROg61 (along with the extensive anatomic abnormalities in the right parietal and occipital lobes) and perform a standard right temporal lobectomy. The patient remains seizure free and back at work one year later.

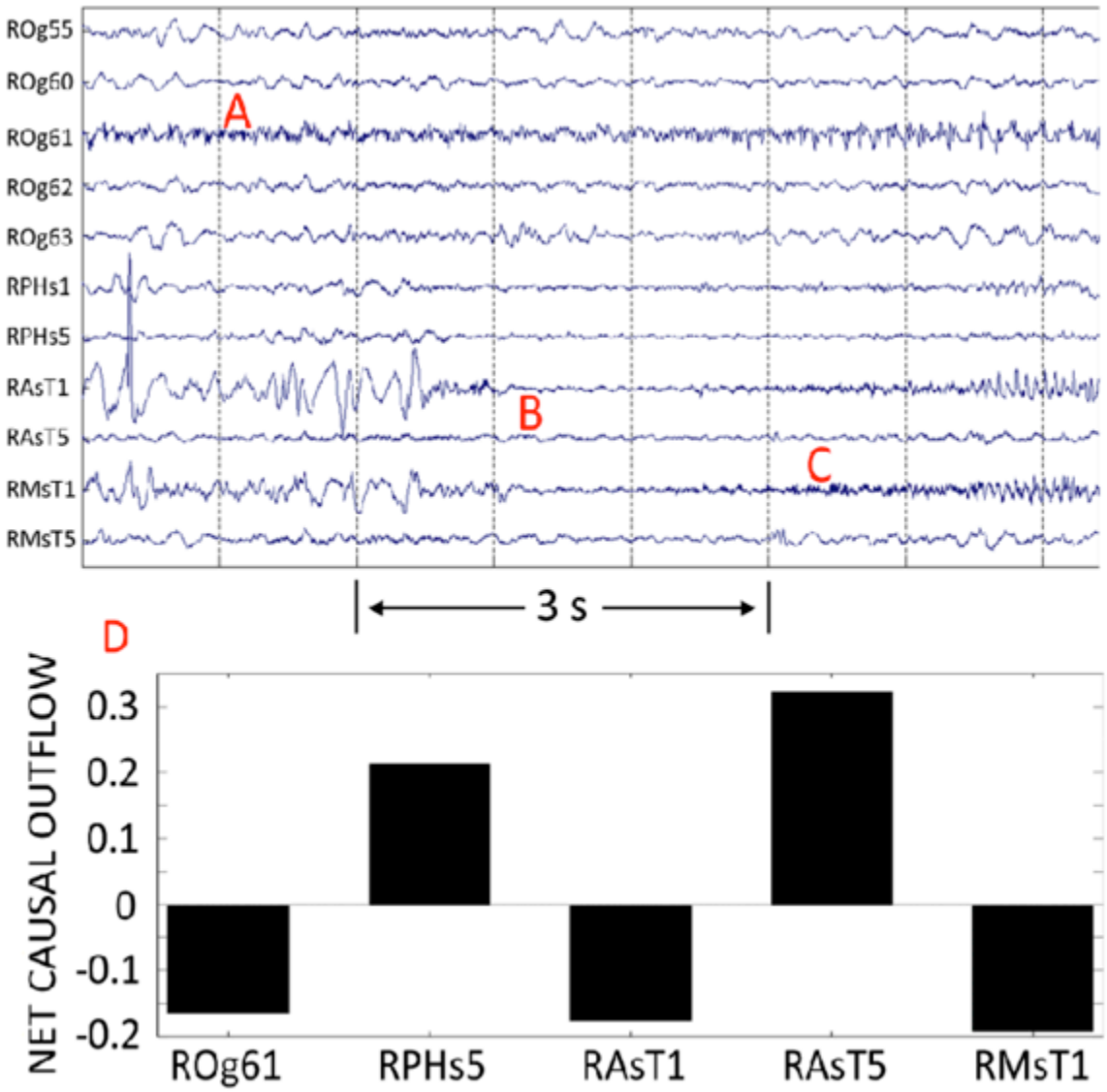

Figure 4.5 Visible ictal onset in the first prospective patient. HF = 240, LF = 1, nominal sensitivity = 100 µV/mm. ROg = portions of a Right Occipital grid, RPHs = Right Parahippocampal strip, RAsT = Right Anterior Subtemporal strip, RMsT =Right Midtemporal strip. A. The earliest visually-apparent activity consists of fast narrow spikes at right occipital grid electrode ROg61, preceding ictal activity in the right temporal lobe. B. Electrodecrement in parahippocampal and anterior-mesial temporal strips. C. High frequency oscillations progressing to ictal beta in anterior and mid-temporal strip electrodes RAsT1 and RMsT1. D. GC comparison limited to the electrodes that appear most involved in the initial ictal discharge, showing ROg61 and the 4 strongest sources in A - C. Despite being visible earliest and at highest frequency, ROg61 is a causal sink over the selected time interval (~7.5 s)—while the strongest causal sources are

the fifth, rather than the first, anterior and mid-temporal strip electrodes. This finding was interpreted as evidence against ROg61 representing the ictal onset zone or a major node in seizure propagation.

Prospective Case 2 is a 35-year-old left handed man with complex partial seizures and rare secondary generalization following reported H. influenza meningitis in infancy, and later febrile seizures at age 3. 3T anatomic MRI showed marked atrophy of the right mammillary body and fornix, with no hippocampal abnormality. PET scan showed bilaterally symmetric hypometabolism in the mesial temporal lobes. Wada test indicated left hemisphere dominance for language, and neuropsychological evaluation was considered mildly suggestive of right hemisphere dysfunction. Scalp video-EEG of seven seizures suggested onset predominantly from the right parieto-temporal-occipital region, with interictal epileptiform discharges in the right frontotemporal, midtemporal, and parieto-temporal-occipital regions. IEEG recording was made from multiple strip, grid, and amygdalohippocampal depth electrodes designed to cover areas of the right hemisphere extending from the frontal to the parietal and inferior temporal-occipital region. Based on visual criteria, the seizure onset zone was considered likely to lie in the posterolateral temporal and occipital areas. A formal epilepsy surgery conference considered further electrode implants in that region extending dorsal to the parietal lobe, versus an extensive cortical resection sparing the amygdala and hippocampus. However, later review of GC results suggested that preictal activity was unexpectedly prominent in the amygdala and hippocampal depths (Figure 4.6), while head-to-head comparison of the most prominent GC sources at the time GC became significant (Figure 4.7) indicated that the strongest causal source was a depth electrode in the amygdala, followed by hippocampal depth electrodes. In comparison, posterior temporal and occipital neocortical electrodes were relative GC sinks. Considering this result, a second epilepsy surgery conference changed the recommendation to a standard right anterior temporal lobecto-

my, including the amygdala and hippocampus, and neocortex below right temporal grid electrode 1; with plans to revisit the posterior neocortical regions only if the first resection was unsuccessful. This patient had a single atypical postoperative seizure without loss of consciousness at 24 hours, has returned to full employment, and has reported a few brief auras without alteration in behavior or consciousness in the six months since surgery.

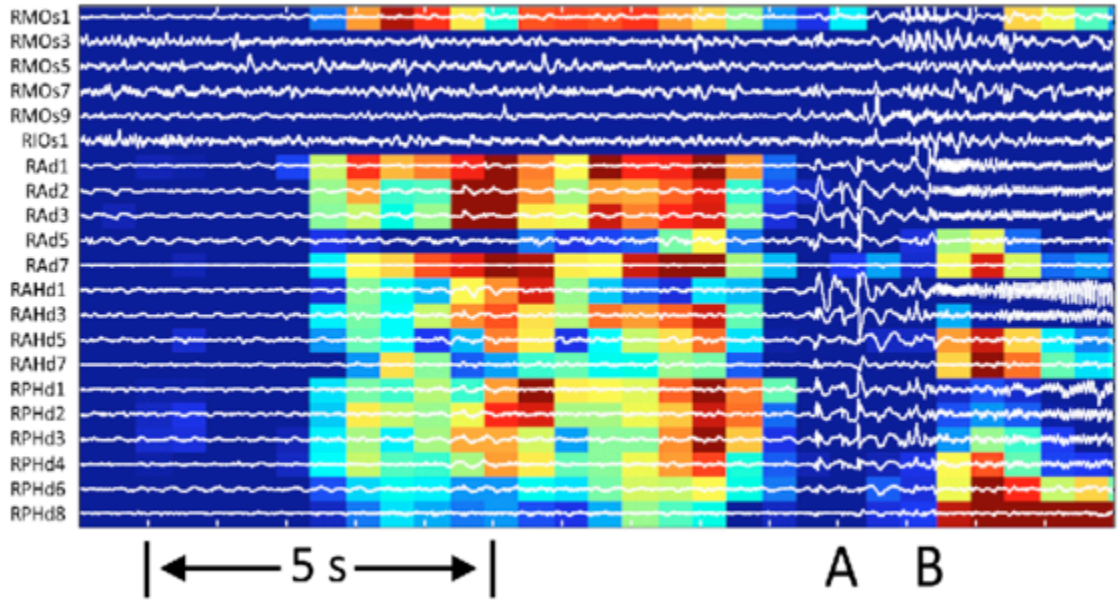

Figure 4.6 GC outflow sources overlaid on selected channels of IEEG for 12 seconds before and during visible ictal onset in the second prospective patient. Display parameters as in Figure 4.5. RMOs is a right mid-occipital strip; RIOs1 is the most ventral electrode of an inferior occipital strip; RAd, RAHd, and RPHd are amygdalar, anterior hippocampal, and posterior hippocampal depths respectively. A short train of spikes (A), more widespread than is visible in these selected channels, is followed one second later by a widespread polymorphic ictal discharge (B).

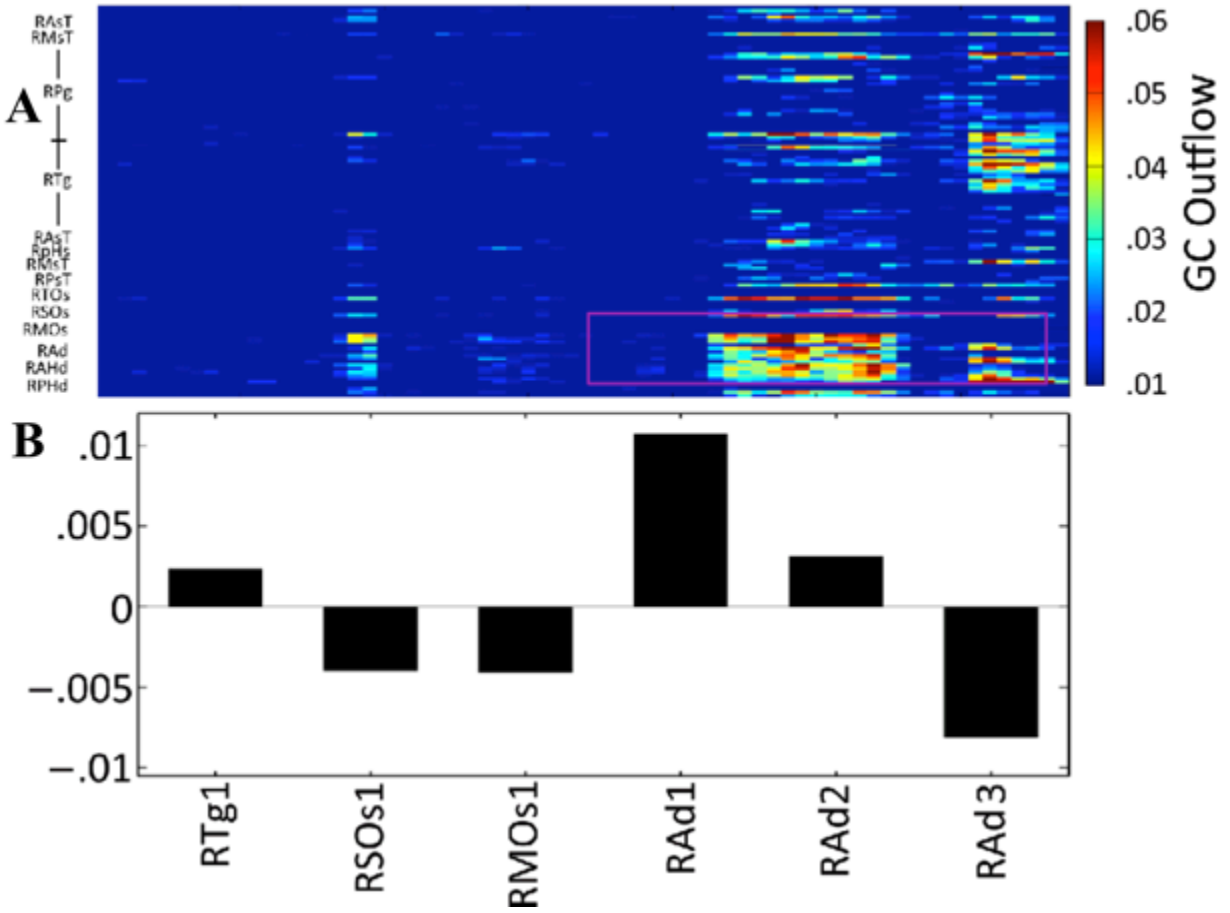

Figure 4.7 A. GC outflow sources for all sampled electrodes in the same patient as Figure 4.6, extending from 30 seconds prior to visible ictal onset to 4 seconds after. The section outlined in purple corresponds to the data selected in Figure 4.6. Additional electrodes: RAsT =Right Anterior Temporal strip; RMsT = Right Mid-Temporal strip; RPg =Right Parietal grid; RTg = Right Temporal grid; RPsT = Right Posterior Temporal strip. B. Pairwise GC outflow comparison limited to the 6 most prominent GC source electrodes, computed prior to ictal onset. The first amygdalar depth electrode is the dominant source, with the second amygdalar depth electrode next. RSOs1 and RMOs1, two sites of apparent visible ictal onset, are relative sinks. RTg1, a weaker relative source, was within the area of the subsequent anterior temporal resection.

Though the spectral Granger causality (GC) and related techniques applied to iEEG at HFO frequencies helped to identify seizure onset zones and times, the greatest impediment to it is the enormous number of calculations needed to evaluate causal relationships among large numbers of channels at high sampling rates. With a dedicated computer requiring roughly one

hour of processing for every second of data, it is challenging even to complete a single ictal analysis prior to explantation of iEEG electrodes. It demands the need of enough computing power, may be use of networked computers or even using the Matlab Cloud for computation, to examine many hours of interictal EEG for significant GC independent of seizures. Moreover, no form of mathematical analysis can identify seizure onsets where we don't have an electrode.

4.4 Conclusions

Identifying targets for the surgical resection in epilepsy remains a complex and imperfect process. Recent cases of seizure-free outcomes after resection of HFO-generating brain tissues [63,64] hint toward the main characteristics of the epileptogenic zones and are highly encouraging. Here, we provide evidence that high-frequency network activities are the precursors of epileptic seizures and a careful evaluation of causal relationships from iEEG recordings can supplement the conventional visual inspection in identifying seizure onset zones for surgery. These findings suggest that high-frequency (>80 Hz) events in iEEG recordings that are close to hidden seizure onset zones can be observed and their causal relationships with the rest of the recordings can assist in surgical localization, thereby increasing cure rates.

5 SUMMARY AND FUTURE OUTLOOK

Using scalp electroencephalography (EEG) recordings combined with source reconstruction techniques, we found that the fine tactile discrimination involves somatosensory processing, focusing attention on stimulus features, encoding the acquired sensory information, visualizing the stimulus features, and eventually forming decisions expressed in motor responses. The correct stimulus perception was found to involve the primary somatosensory cortex, lateral occipital complex, posterior intraparietal sulcus and dorsolateral prefrontal cortex in different temporal millisecond time-scales. We found that ~15 Hz beta band oscillatory networks, dominantly feedforward from somatosensory to lateral occipital to parietal to prefrontal regions, and ~80 Hz gamma band oscillatory networks, occurring in a recurrent closed loop from prefrontal to posterior parietal to somatosensory and back to prefrontal regions, coordinate activity between these regions mediating sensory and cognitive processing to arrive at tactile perceptual decisions. These findings provide important insights into the neural mechanisms and the role of oscillatory interactions within these somatosensory and frontoparietal networks that mediate fine tactile spatial discrimination of the kind that is necessary for Braille reading and hence may inform design of the effective sensory aid devices for the visually impaired. In visually impaired populations, how these neural mechanisms and oscillatory interactions happen remains to be explored.

Applying spectral Granger causality analysis to intracranial electroencephalography (iEEG) recordings in patients during seizures, we found that the high-frequency network activity helps to identify seizure onset times and zones. This technique has potential to increase understanding of preictal network activity and to help improve surgical outcomes. This study involved primarily retrospective patients, but can be applied to the clinical problem of identifying the seizure onset zones, at frequencies including HFOs, in cases where inception appears to be ambigu-

ous or nearly simultaneous in widely separated regions of the brain. Preictal and early ictal GC from individual recording electrodes can be characterized by the strength of causal outflow, spatial distribution, and hierarchical causal relationships. The GC source/sink comparisons will support the exclusion of early ictal regions that may not be the dominant causal sources, and contribute to planning of more limited surgical resections. Building up a systematic algorithm implementing these network calculations which provides the information about the seizure onset zones and times may become a useful addition to the multiplicity of techniques that contribute to increased efficacy and decreased morbidity in the surgical treatment of epilepsy.

REFERENCES

[1] G. Buzsaki and A. Draguhn, Science **304**, 1926 (2004).

[2] F. Varela, J.-P. Lachaux, E. Rodriguez and J. Martinerie, Nat. Rev. Neurosci. **2**, 229 (2001).

[3] C. M. Gray and D. A. McCormick, Science **274** (5284), 109 (1996).

[4] P. J. Uhlhaas and W. Singer, Neuron **52** (1), 155 (2006).

[5] M. Karrasch, M. Laine, P. Rapinoja and C. M. Krause, Neurosci Lett **366**, 18 (2004).

[6] G. Buzsaki, *Rhythms of the Brain*. (Oxford University Press, New York, 2006).

[7] A. von Stein and J. Sarnthein, Int. J. Psychophysiol. **38**, 301 (2000).

[8] P. L. Nunez, Behav. Brain Sci. **23**, 371 (2000).

[9] R. R. Llinas and M. Steriade, J. Neurophysiol. **95**, 3297 (2006).

[10] M. Steriade, *Cellular substtates of brain rhythms.* (Lippincott Williams and Wilkins, Philadelphia, 2005).

[11] A. K. Engel, P. Konig, A. K. Kreiter and W. Singer, Science **252** (5009), 1177 (1991).

[12] S. Lowel and W. Singer, Science **255** (5041), 209 (1992).

[13] M. M. Mesulam, Brain **121**, 1013 (1998).

[14] E. Bullmore and O. Sporns, Nat. Rev. Neurosci. **10** (3), 186 (2009).

[15] P. Hagmann, L. Cammoun, X. Gigandet, R. Meuli, C. J. Honey, V. J. Wedeen and O. Sporns, Plos Biol. **6**, e159 (2008).

[16] D. Zhang and M. E. Raichle, Nat. Rev. Neurol. **6**, 15 (2010).

[17] A. Ekstorm, J. Caplan, E. Ho, K. Shattuck, I. Fried and M. Kahana, Hippocampus **15**, 881 (2005).

[18] S. Raghavachari, J. E. Lisman, M. Tully, J. R. Madsen, E. B. Bromfield and M. J. Kahana, J. Neurophysiol. **95** (3), 1630 (2006).

[19] M. Siegel, A. K. Engel and T. H. Donner, Front. Hum. Neurosci. **5** (21), 1 (2011).

[20] J. F. Hipp, A. K. Engel and M. Siegel, Neuron **69** (2), 387 (2011).

[21] R. Caton, Br. Med. J. **1**, 62 (1877).

[22] H. Berger, Eur. Arch. Psychiatry Clin. Neurosci. **87**, 527 (1929).

[23] H. Berger, Eur. Arch. Psychiatry Clin. Neurosci. **94**, 16 (1931).

[24] H. Berger, Eur. Arch. Psychiatry Clin. Neurosci. **98**, 231 (1933).

[25] W. G. Walter, Eur. Arch. Psychiatry Clin. Neurosci. **206**, 309 (1964).

[26] E. Niedermeyer and F. da Silva, *Electroencephalography: Basic Principles, Clinical Applications, and Related Fields.* (Lippincot Williams & Wilkins, 2004).

[27] P. Kahane, E. Landré, L. Minotti, S. Francione and P. Ryvlin, Epileptic Disord. **2**, 16 (2006).

[28] P. Adelson, P. Black, J. Madsen, U. Kramer, M. Rockoff and J. Riviello, Pediatr. Neurosurg. **22** (4), 174 (1995).

[29] E. Behrens, J. Zentner, D. van Roost, A. Hufnagel, C. E. Elger and J. Schramm, Acta Neurochir. **128**, 84 (1994).

[30] A. A. De Salles, B. E. Swartz, T. T. Lee and A. V. Delgado-Escueta, Stereotact. Funct. Neurosurg. **62** (1-4), 226 (1994).

[31] H. Luders, I. Awad, R. Burgess, E. Wyllie and P. Van Ness, Epilepsy Res. Suppl. **5**, 47 (1992).

[32] L. F. Quesney, F. Cendes, A. Olivier, F. Dubeau and F. Andermann, Adv. Neurol. **66**, 243 (1995).

[33] R. Wennberg, F. Quesney, A. Olivier and T. Rasmussen, Electroencephalogr. Clin. Neurophysiol. **106** (4), 357 (1998).

[34] G. Pfurtscheller and R. Cooper, Electroenceph. Clin. Neurophysiol. **38**, 93 (1975).

[35] J. Lachaux, D. Rudrauf and P. Kahane, J. Physiol. **97**, 613 (2003).

[36] V. A. Zaccariotti, H. W. Pannek, H. Holthausen and F. Oppel, Neurol. Res. **21** (5), 463 (1999).

[37] D. Blumer and D. Benson, *Personality changes with frontal and temporal lobe lesions.* (Grune & Stratton, New York, 1975).

[38] J. Ibarz, G. Foffani, E. Cid, M. Inostroza and L. Prida, J. Neurosci. **30** (48), 16249 (2010).

[39] J. A. Cramer, R. Fisher, E. Ben-Menachem, J. French and R. H. Mattson, Epilepsia **40** (5), 590 (1999).

[40] P. Kwan, G. J. Sills and M. J. Brodie, Pharmacol. Ther. **90**, 21 (2001).

[41] M. Brazdil, J. Halamek, P. Jurak, P. Daniel, R. Kuba, J. Chrastina, Z. Novak and I. Rektor, Epilepsy Res **90**, 28 (2010).

[42] M. Zijlmans, J. Jacobs, R. Zelmann, F. Dubeau and J. Gotman, Neurology **72**, 979 (2009).

[43] A. Bragin, J. Engel, C. L. Wilson, I. Fried and G. W. Mathern, Epilepsia **40**, 127 (1999).

[44] A. Bragin, C. L. Wilson, R. J. Staba, M. Reddick, I. Fried and J. Engel, Ann. Neurol. **52**, 407 (2002).

[45] R. J. Staba, C. L. Wilson, A. Bragin, I. Fried and J. Engel, J. Neurophysiol. **88**, 1743 (2002).

[46] R. J. Staba, C. L. Wilson, A. Bragin, D. Jhung, I. Fried and J. Engel, Ann. Neurol. **56**, 108 (2004).

[47] G. Buzsaki, Z. Horvath, R. Urioste, J. Hetke and K. Wise, Science **256**, 1025 (1992).

[48] A. Ylinen, A. Bragin, Z. Nadasdy, G. Jando, I. Szabo, A. Sik and G. Buzsaki, J. Neurosci. **15**, 30 (1995).

[49] G. Buzsaki and X. J. Wang, Ann. Rev. Neurosci. **35**, 203 (2012).

[50] J. Engel, A. Bragin, R. Staba and I. Mody, Epilepsia **50**, 598 (2009).

[51] J. Jacobs, P. LeVan, R. Chander, J. Hall, F. Dubeau and J. Gotman, Epilepsia **49**, 1893 (2008).

[52] A. Gardner, G. Worrell, E. Marsh, D. Dlugos and B. Litt, Clin. Neurophysiol. **118**, 1134 (2007).

[53] J. Jacobs, R. Zelmann, J. Jirsch, R. Chander, C. Chatillon, F. Dubeau and J. Gotman, Epilepsia **50** (7), 1780 (2009).

[54] J. Jacobs, R. Staba, E. Asano, H. Otsubo, J. Y. Wu, M. Zijlmans, I. Mohamed, P. Kahane, F. Dubeau, V. Navarro and J. Gotman, Prog. Neurobiol. **98** (3), 302 (2012).

[55] R. J. Staba, M. Stead and G. A. Worrell, Neurotherapeutics **DOI:10.1007/s13311-014-0259-0** (2014).

[56] M. Dhamala, G. Rangarajan and M. Ding, Neuroimage **41** (2), 354 (2008).

[57] M. Dhamala, G. Rangarajan and M. Ding, Phys. Rev. Lett. **100** (1) (2008).

[58] M. Ding, Y. Chen and S. Bressler, **(eds. B. Schelter, M. Winterhadler, J. Timmers)**, 437 (2006).

[59] J. Geweke, J. Am. Stat. Ass. **77** (378), 304 (1982).

[60] A. K. Engel, P. Fries and W. Singer, Nat. Rev. Neurosci. **2**, 704 (2001).

[61] W. Singer, Neuron **24**, 49 (1999).

[62] J. I. Gold and M. N. Shadlen, Trends Cogn. Sci. **5**, 10 (2001).

[63] J. I. Gold and M. N. Shadlen, Annu. Rev. Neurosci. **30**, 535 (2007).

[64] H. R. Heekeren, S. Marrett and L. G. Ungerleider, Nat. Rev. Neurosci. **9** (6), 467 (2008).

[65] M. Usher and J. L. McClelland, Psychol. Rev. **108** (3), 550 (2001).

[66] B. Pleger and A. Villringer, Prog. Neurobiol. **103**, 76 (2013).

[67] R. Romo and V. de Lafuente, Prog. Neurobiol. **103**, 41 (2013).

[68] K. Sathian, G. Deshpande and R. Stilla, J. Neurosci. **33** (12), 5387 (2013).

[69] R. Stilla, G. Deshpande, S. LaConte, X. Hu and K. Sathian, J. Neurosci. **27** (41), 11091 (2007).

[70] R. Stilla, R. Hanna, X. Hu, E. Mariola, G. Deshpande and K. Sathian, J. Vis. **8** (10), 1 (2008).

[71] T. Allison, G. McCarthy, C. C. Wood, T. M. Darcey, D. D. Spencer and P. D. Williamson, J. Neurophysiol. **62** (3), 694 (1989).

[72] F. Mauguiere, I. Merlet, N. Forss, S. Vanni, V. Jousmaki, P. Adeleine and R. Hari, Electroen. Clin. Neuro. **104**, 290 (1997).

[73] N. Forss, R. Hari, R. Salmelin, A. Ahonen, M. Hamalainen, M. Kajola, J. Knuutila and J. Simola, Exp. Brain Res. **99** (2), 309 (1994).

[74] N. Forss, I. Merlet, S. Vanni, M. Hamalainen, F. Mauguiere and R. Hari, Brain Res. **734**, 229 (1996).

[75] F. Mauguiere, I. Merlet, N. Forss, S. Vanni, V. Jousmaki, P. Adeleine and R. Hari, Electroen. Clin. Neuro. **104** (4), 281 (1997).

[76] L. Garcia-Larrea, A. C. Lukaszewicz and F. Mauguiere, Psychophysiology **32** (6), 526 (1995).

[77] R. Zopf, C. M. Giabbiconi, T. Gruber and M. M. Müller, Cognitive Brain Res. **20** (3), 491 (2004).

[78] M. Junghofer, T. Elbert, D. N. Tucker and B. Rockstroh, Psychophysiology **37**, 523 (2000).

[79] M. Hamalainen and R. J. Ilmoniemi, Med. Biol. Eng. Comput. **32**, 35 (1994).

[80] J.-Z. Wang, S. J. Williamson and L. Kaufman, IEEE T. Bio-Med. Eng. **39** (7), 665 (1992).

[81] A. M. Dale and M. I. Sereno, J. Cogn. Neurosci. **5** (2), 162 (1993).

[82] M. Hamalainen, R. Hari, R. J. Ilmoniemi, J. Knuutila and O. V. Lounasmaa, Rev. Mod. Phys. **65** (2), 413 (1993).

[83] W. J. Freeman, L. J. Rogers, M. D. Holmes and D. L. Silbergeld, J. Neurosci. Methods **95** (2), 111 (2000).

[84] M. Ding, Y. Chen and S. L. Bressler, *Granger causality: basic theory and application to neuroscience. Handbook of Time Series Analysis: Recent Theoretical Developments and Applications* (Wiley-VCH, Berlin, 2006).

[85] R. C. Blair and W. Karniski, Psychophysiology **30** (5), 518 (1993).

[86] A. Brovelli, M. Ding, A. Ledberg, Y. Chen, R. Nakamura and S. L. Bressler, Proc. Natl. Acad. Sci. U. S. A. **101** (26), 9849 (2004).

[87] X. Wang, Y. Chen and M. Ding, Neuroimage **41** (3), 767 (2008).

[88] L. Xu, P. Stoica, J. Li, S. L. Bressler, X. Shao and M. Ding, IEEE Trans. on Biomed. Eng. **56** (1), 111 (2009).

[89] L. Faes, G. Nollo and A. Porta, Entropy **15** (1), 198 (2013).

[90] M. Lindner, R. Vicente, V. Priesemann and M. Wibral, BMC Neurosci. **12**, 119 (2011).

[91] R. Auksztulewicz, B. Spitzer and F. Blankenburg, J. Neurosci. **32** (3), 799 (2012).

[92] M. C. Klein-Flugge and S. Bestmann, J. Neurosci. **32** (24), 8373 (2012).

[93] L. P. Selen, M. N. Shadlen and D. M. Wolpert, J. Neurosci. **32** (7), 2276 (2012).

[94] G. Deshpande, X. Hu, R. Stilla and K. Sathian, Neuroimage **40** (4), 1807 (2008).

[95] G. Deshpande, X. Hu, S. Lacey, R. Stilla and K. Sathian, Neuroimage **49** (3), 1991 (2010).

[96] S. Peltier, R. Stilla, E. Mariola, S. LaConte, X. Hu and K. Sathian, Neuropsychologia **45** (3), 476 (2007).

[97] J. N. Lucan, J. J. Foxe, M. Gomez-Ramirez, K. Sathian and S. Molholm, Hum. Brain Mapp. **31** (11), 1813 (2010).

[98] A. Amedi, G. Jacobson, T. Hendler, R. Malach and E. Zohary, Cereb. Cortex **12**, 1202 (2002).

[99] A. Amedi, R. Malach, T. Hendler, S. Peled and E. Zohary, Nat. Neurosci. **4** (3), 324 (2001).

[100] R. Stilla and K. Sathian, Hum. Brain Mapp. **29** (10), 1123 (2008).

[101] M. Zhang, V. D. Weisser, R. Stilla, S. C. Prather and K. Sathian, Cogn. Affect. Behav. Neurosci. **4** (2), 251 (2004).

[102] R. C. Coghill, I. Gilron and M. C. Iadarola, J. Neurophysiol. **85**, 2602 (2001).

[103] S. P. Tomlinson, N. J. Davis, H. M. Morgan and R. M. Bracewell, Neuropsychologia **49** (9), 2703 (2011).

[104] M. Corbetta and G. L. Shulman, Nat. Rev. Neurosci. **3** (3), 201 (2002).

[105] M. Siegel, T. H. Donner, R. Oostenveld, P. Fries and A. K. Engel, Neuron **60** (4), 709 (2008).

[106] B. Opitz, A. Mecklinger and A. D. Friederici, Learn. Memory **7** (2), 85 (2000).

[107] F. Roux, M. Wibral, H. M. Mohr, W. Singer and P. J. Uhlhaas, J. Neurosci. **32** (36), 12411 (2012).

[108] J. S. Feinstein, M. B. Stein, G. N. Castillo and M. P. Paulus, Conscious. Cogn. **13** (2), 323 (2004).

[109] R. Marois, D.-J. Yi and M. V. Chun, Neuron **41**, 465 (2004).

[110] A. Sahraie, L. Weiskrentz, J. L. Barbur, A. Simmons, S. C. R. Williams and M. J. Brammer, Proc. Natl. Acad. Sci. U. S. A. **94**, 9406 (1997).

[111] F. Blankenburg, B. Taskin, J. Ruben, M. Moosmann, P. Ritter, G. Curio and A. Villringer, Science **299**, 1864 (2003).

[112] B. W. Colder and L. Tanenbaum, Cogn. Brain Res. **8**, 177 (1999).

[113] K. J. Meador, P. G. Ray, J. R. Echauz, D. W. Loring and G. J. Vachtsevanos, Neurology **59**, 847 (2002).

[114] M. Brazdil, I. Rektor, P. Daniel, M. Dufek and P. Jurak, Clin. Neurophysiol. **112**, 650 (2001).

[115] L. Naccache and S. Dehaene, Cereb. Cortex **11**, 966 (2001).

[116] R. Schubert, F. Blankenburg, S. Lemm, A. Villringer and G. Curio, Psychophysiology **43** (1), 31 (2006).

[117] P. J. Uhlhaas, G. Pipa, B. Lima, L. Melloni, S. Neuenschwander, D. Nikolic and W. Singer, Front. Integr. Neurosci. **3**, 17 (2009).

[118] X. J. Wang, Physiol. Rev. **90** (3), 1195 (2010).

[119] M. Bauer, R. Oostenveld, M. Peeters and P. Fries, J. Neurosci. **26** (2), 490 (2006).

[120] O. Jensen, J. Kaiser and J. P. Lachaux, Trends Neurosci. **30** (7), 317 (2007).

[121] B. Spitzer and F. Blankenburg, Proc. Natl. Acad. Sci. U. S. A. **108** (20), 8444 (2011).

[122] S. Hanslmayr, T. Staudigl and M. C. Fellner, Front. Hum. Neurosci. **6**, 74 (2012).

[123] R. F. Salazar, N. M. Dotson, S. L. Bressler and C. M. Gray, Science **338** (6110), 1097 (2012).

[124] W. Singer, Ann. NY. Acad. Sci. **929**, 123 (2001).

[125] Y. Zhang and M. Ding, J. Cogn. Neurosci. **22** (2), 307 (2009).

[126] A. Bollimunta, J. Mo, C. E. Schroeder and M. Ding, J. Neurosci. **31** (13), 4935 (2011).

[127] J. Mo, C. E. Schroeder and M. Ding, J. Neurosci. **31** (3), 878 (2011).

[128] F. Varela, J.-P. Lachaux, E. Rodriguez and J. Martinerie, Nat Rev Neurosci **2**, 229 (2001).

[129] J. Y. Wu, R. Sankar, J. T. Lerner, J. H. Matsumoto, H. V. Vinters and G. W. Mathern, Neurolology **75**, 1686 (2010).

[130] T. H. Donner, M. Siegel, P. Fries and A. K. Engel, Curr Biol **19** (18), 1581 (2009).

[131] K. Lehnertz, J. Biol. Phys. **34**, 253 (2008).

[132] R. Quian Quiroga, J. Arnhold, K. Lehnertz and P. Grassberger, Phys. Rev. E **62** (2), 8380 (2000).

[133] J. C. Sackellares, D. S. Shiau, L. D. Iasemidis, P. M. Pardalos and W. Chaovalitwongse, Ann. Neurol. **52** (3), S65 (2002).

[134] Y.-C. Lai, M. A. Harrison, M. Frei and I. Osorio, Phys. Rev. Lett. **91** (6), 068102 (2003).

[135] H. Luders, R. P. Lesser, D. S. Dinner, H. H. Morris and G. Klem, Electroencephalography and clinical neurophysiology **61** (3), S72 (1985).

[136] C. R. Clark, A. C. McFarlane, P. Morris, D. L. Weber, C. Sonkkilla, M. Shaw, J. Marcina, H. j. Tochon-Donguy and G. F. Egan, Biol Psychiatry **53** (6), 474 (2003).

[137] C. W. J. Granger, Econometrica **37** (3), 424 (1969).

[138] O. Hauk, Neuroimage **21** (4), 1612 (2004).

[139] D. A. Smirnov and B. P. Bezruchko, Europhys. Lett. **100**, 10005 (2012).

APPENDICES

Appendix A

Appendix A.1: Power, coherence and causality spectra

From the single source trials producing correct responses, ensemble averages signal was removed and spectral quantities (power, coherence and Granger causality spectra) associated with nodes (L SI, R LOC, R pIPS and L dlPFC) and their networks were computed for all participants. Figure A1 shows some of the results from one participant before separating frequency band-specific activities for further analyses. There are two spectral peaks, one at around 15 Hz and the other at around 80 Hz in the power, coherence and Granger causality spectra. To see whether trial-to-trial variability has any effect on the spectra, we removed ensemble averages from single trials by using the ASEO method [88] and computed these spectral quantities. Although the magnitude of these quantities decreased in the ASEO-treated data, the results did not change significantly. Figure A2 shows power and some of Granger causality spectra obtained after using ASEO method.

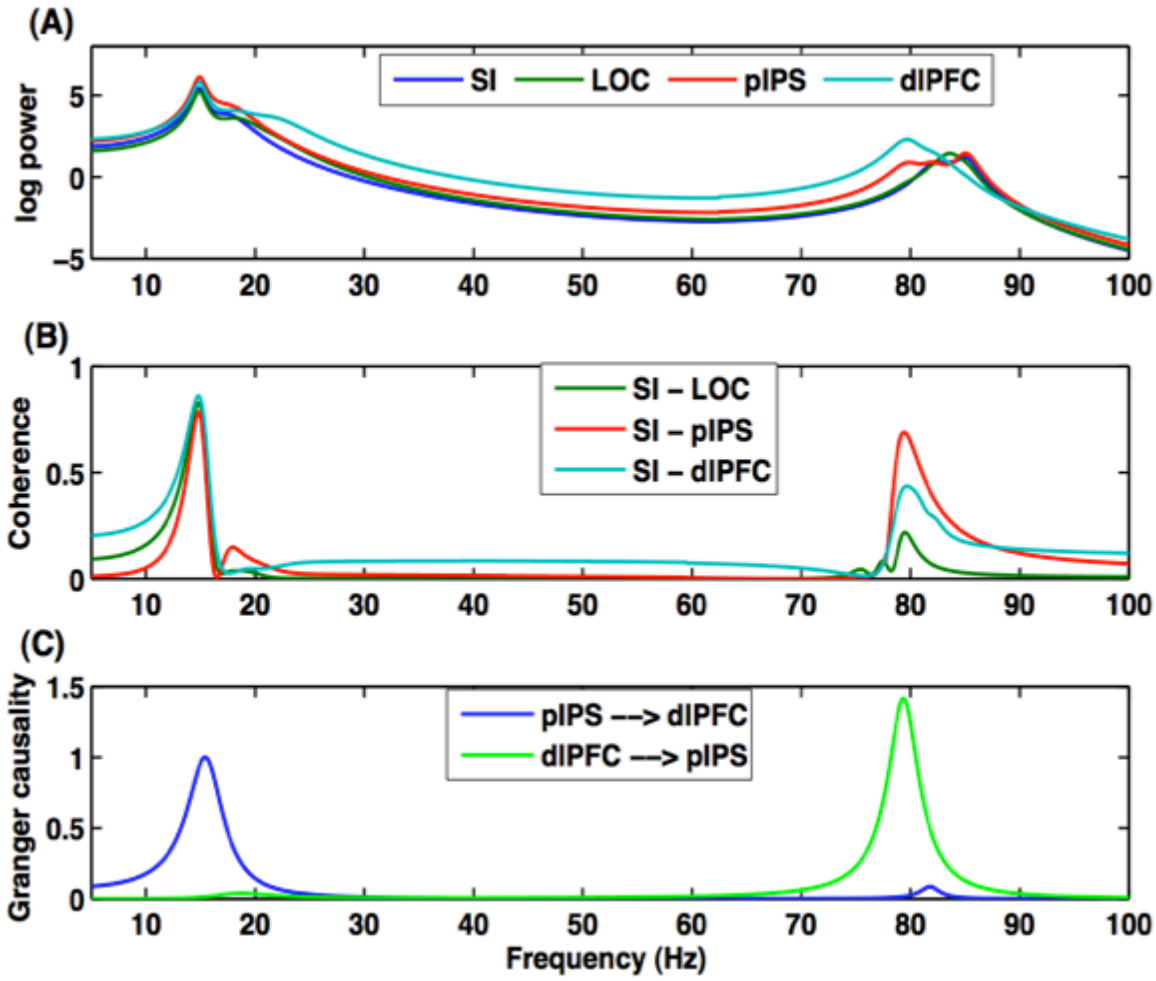

Figure A1: Power spectra (A), coherence spectra (B) and Granger causality spectra (C) from a participant while performing a tactile discrimination task and providing the correct response.

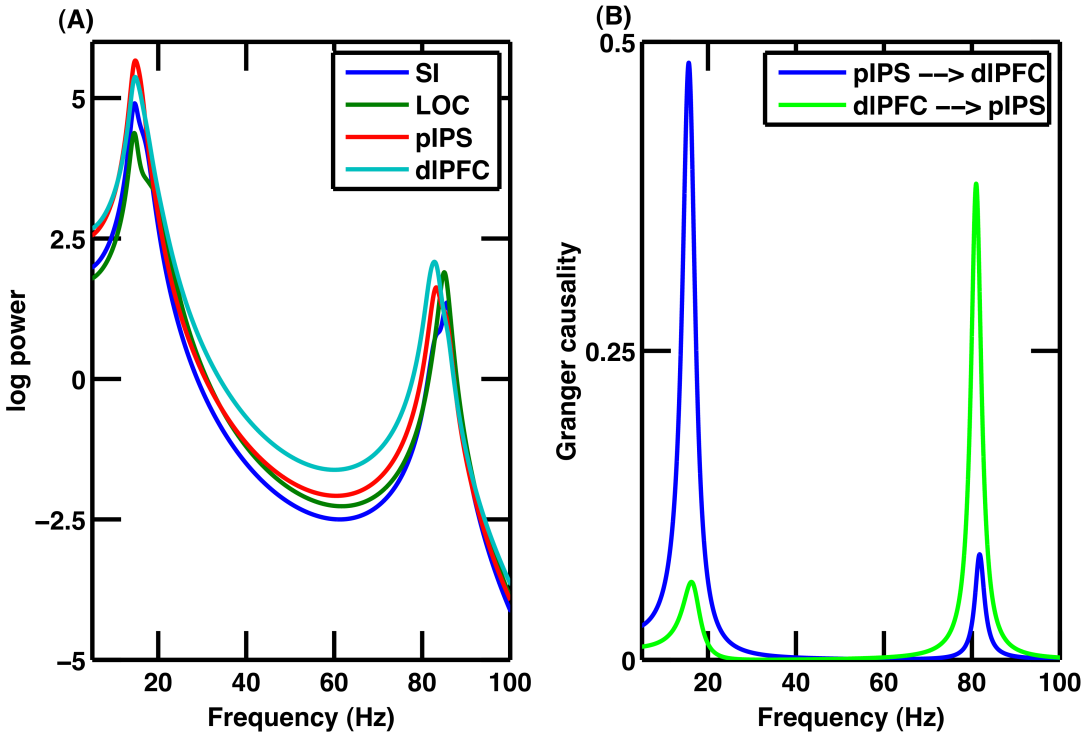

Figure A2: Power spectra from all four nodes (A), and Granger causality spectra (B) from a pair of nodes (pIPS and dlPFC). These spectral measures were calculated from the single trial source waveforms after removing ensemble averages with the ASEO method. The Granger causality spectral peaks, though reduced in magnitudes, remain significant at ~15 Hz in beta and ~80 Hz in gamma frequency bands as in the traditional method.

Appendix A.2: Dominant causal influences: feedforward or feedback or both?

To determine whether there was asymmetry between feedback and feedforward directed connectivity during tactile perceptual decision-making; we performed pairwise tests for the Granger causality values between feedforward and feedback connections in each participant in the post-stimulus period (30 to 210 ms). The net direction of interaction in the beta band network turned out to be feedforward ($p < 0.05$), whereas in the gamma band, it was found that there was no dominant feedforward or feedback interaction ($p > 0.05$) [Figure A3 (A-B)].

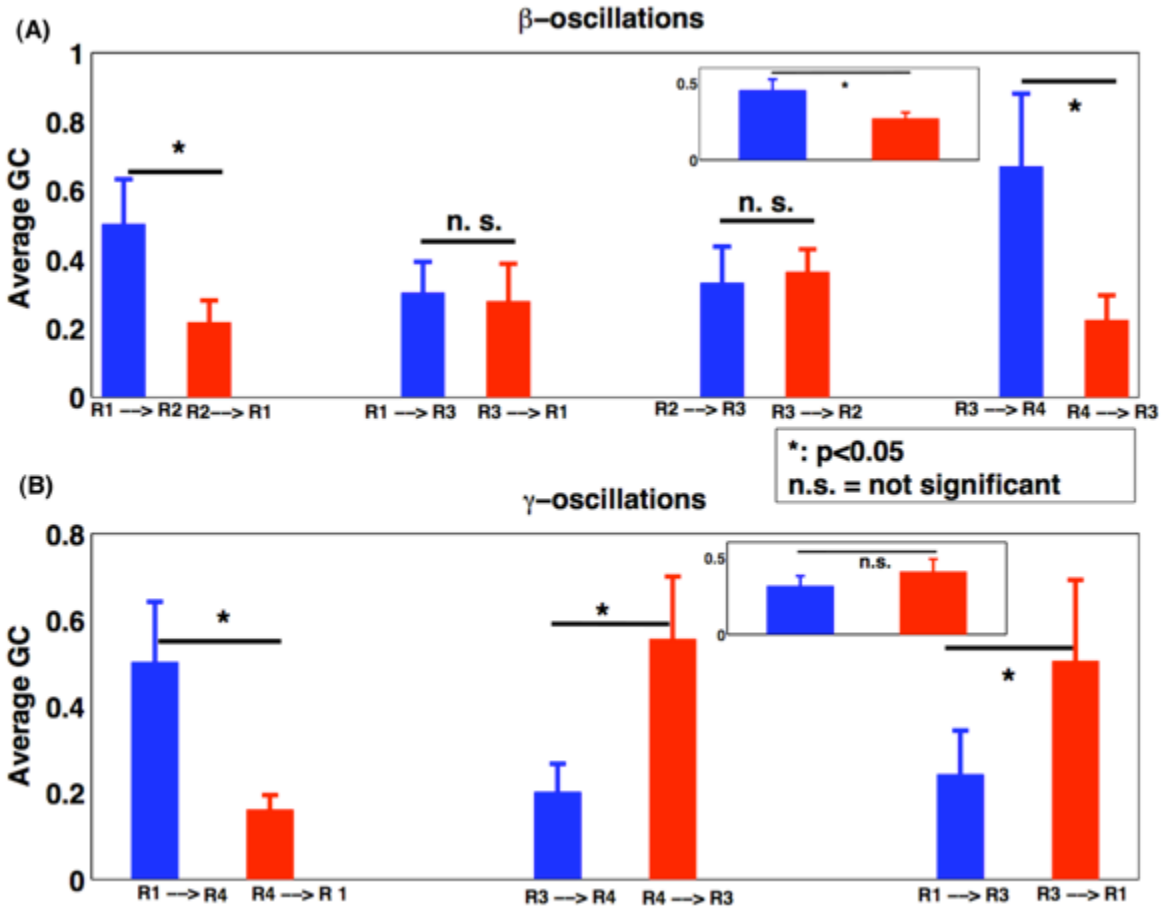

Figure A3**:** Post-stimulus symmetrical and asymmetrical network activity in the beta band (A) and the gamma band (B). Here, R1= L SI, R2 = R LOC, R3 = R pIPS and R4 = L dlPFC. Inset in (A) shows the overall feedforward interaction (blue) is significantly greater than the feedback interaction (red) in the beta band. The inset in (B) shows that there was no dominance of feed-forward over feedback interactions, or the other way around; it was rather a recurrent loop for interaction (from SI to dlPFC, then to pIPS and to SI). Here, * indicates the significance of $p < 0.05$ and n.s. means not significant. Error bars are standard error of mean (S. E. M.).

Beta band network activity [Fig. A3 (A)]: Bidirectional interactions (feedback and feed-forward) between SI and pIPS and between LOC and pIPS did not differ significantly. However, the feedforward interaction from SI to LOC was significantly stronger than the feedback interaction from LOC to SI. Also, the feedforward network interaction from pIPS to dlPFC differed

significantly compared to the feedback network interaction from dlPFC to pIPS. As shown in the inset [Fig. A3 (A)], the overall feedforward network interaction (blue) was significantly different from the feedback network interaction.

Gamma band network activity [Fig. A3 (B)]: The direction of interactions from SI to dlPFC, dlPFC to pIPS, pIPS to SI differed significantly from dlPFC to SI, pIPS to dlPFC, SI to pIPS respectively [Fig. A3 (B)]. But there was no dominance of feedforward over feedback interactions, or the other way around [inset Fig. A3 (B)].

Appendix A.3: Absence of organized feedforward or feedback network activity in the prestimulus durations

In order to confirm that the observed network interaction patterns and Granger-causality based interactions could not be observed in the absence of task performance, we analyzed the data from the prestimulus period (-100 to 0 ms), computing Granger causality in the beta and gamma bands. As shown in Figure A4 (A-B), there was an absence of organized feedforward or feedback network activity in the prestimulus durations in both beta and gamma bands.

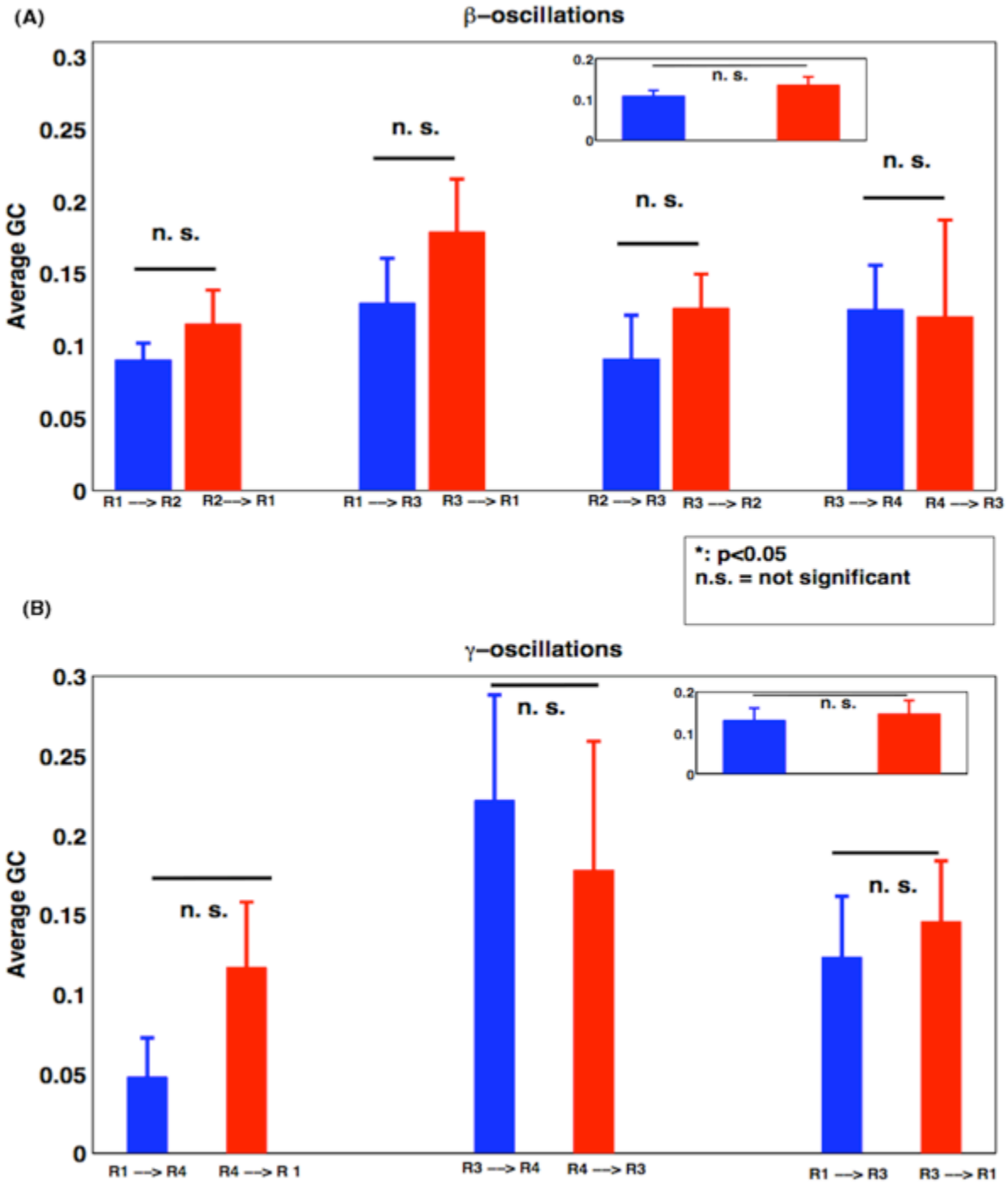

Figure A4: Prestimulus network in beta band (A) and gamma band (B). Abbreviations and colors as in Figure A3. Neither the feedforward and feedback network interactions nor the overall feed-forward and feedback direction of interactions (insets) were significantly different ($p<0.05$) during the prestimulus period. R1, R2, R3, and R4 as in Fig. A3. Error bars are S.E.M.

Appendix A.4: Network activity is not a result of residual volume conduction in the source signals

We used the procedure used in previous studies [89,90] of time-shifting driven signals to evaluate and rule out potential effects of residual volume conduction in the reconstructed source signals. The comparison between the average maximum Granger causality values of the original time series and the distribution of its values obtained for a set of 50 time-shifted surrogates for correct trials associated with two nodes (pIPS and dlPFC) showed the directed causal influences were not the result of volume conduction (Fig. A5).

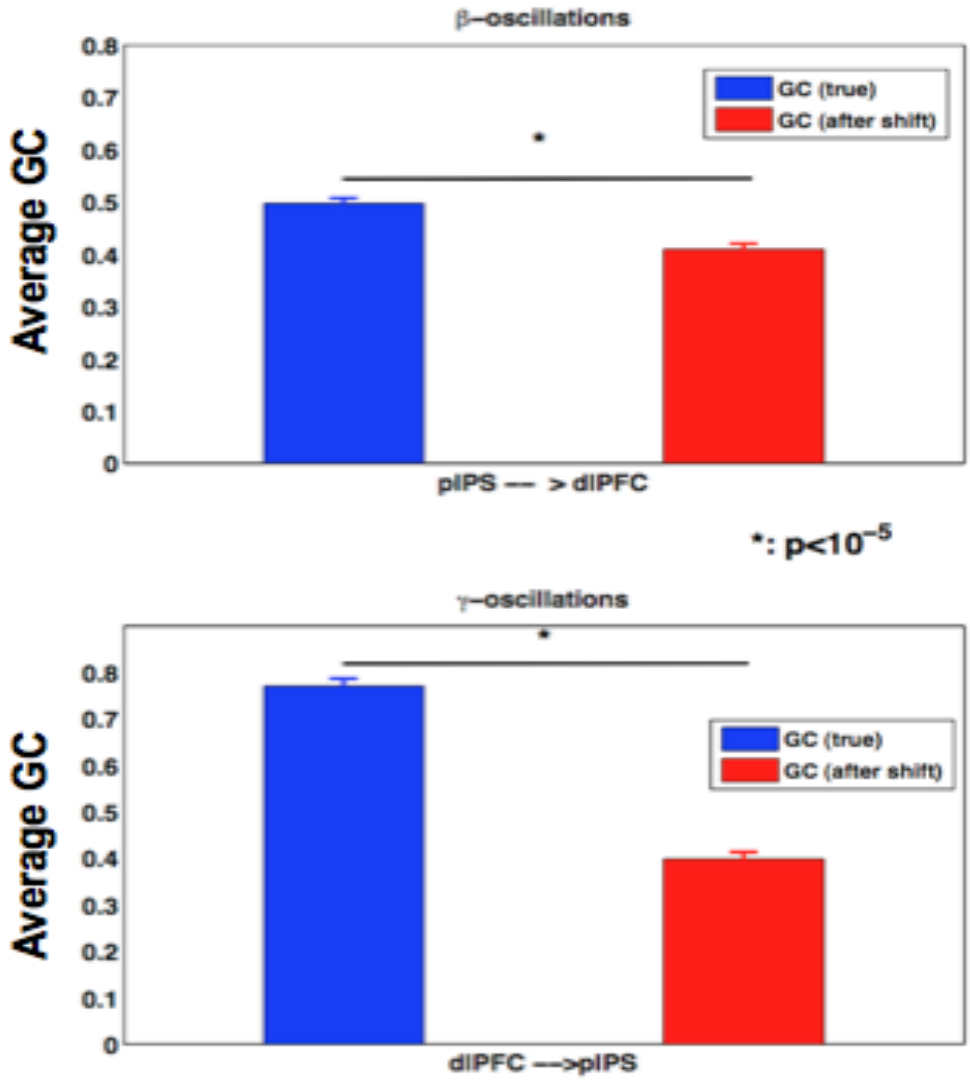

Figure A5: Effect of any residual volume conduction in the source signals: true Granger causality (blue) and that obtained after shifting the time points (red). Here time points were shifted by, t =1, 2, 3, 4, 5 points to generate surrogate time series and to test the hypothesis that Granger causality would strengthen by time-shifting the driven signals if volume conduction effects were present in the data.

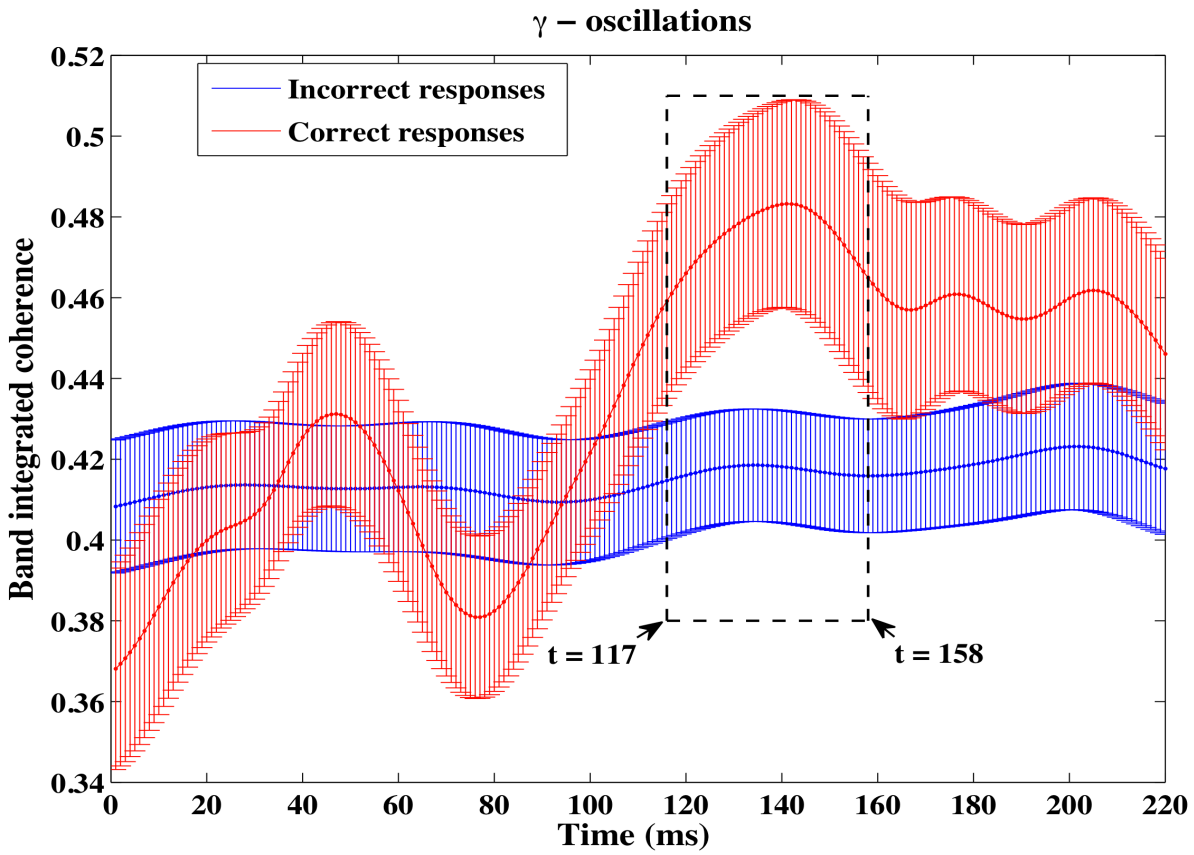

Figure A6: Gamma coherence (pIPS – dlPFC) during trials with correct and incorrect responses

Appendix A.5: Time-frequency maps of power, coherence and causality spectra

We performed time-frequency analyses separately for both beta and gamma band oscillations and examined the power spectra, coherence spectra and Granger causality spectra to better assess the spectral specificity and temporal evolution of neuronal effects for the duration of -100 to 600 ms.

Beta-oscillations: All the activation nodes demonstrated peak power at around 15 Hz, with pIPS showing the highest value and LOC, the lowest [Fig. A7 (1st column)]. Fig. A7 (2nd column) shows the coherence spectra peaking at around 15 Hz. From pairwise Granger causality spectra (3rd and 4th columns of Fig. A7), the interactions between SI and LOC, and between

LOC and pIPS, were bidirectional, while that between pIPS and dlPFC was unidirectional, all at around 15 Hz.

Gamma-oscillations: All nodes displayed peak power at around 80 Hz, with the highest power at dlPFC [Fig. A8 (1st column)]. The coherence spectra [Fig. A8 (2nd column)] for pIPS-dlPFC and SI-dlPFC were coherently modulated at around 80 Hz. The 3rd and 4th columns of Fig. A7 show the pairwise Granger causality spectra for a pair of network nodes.

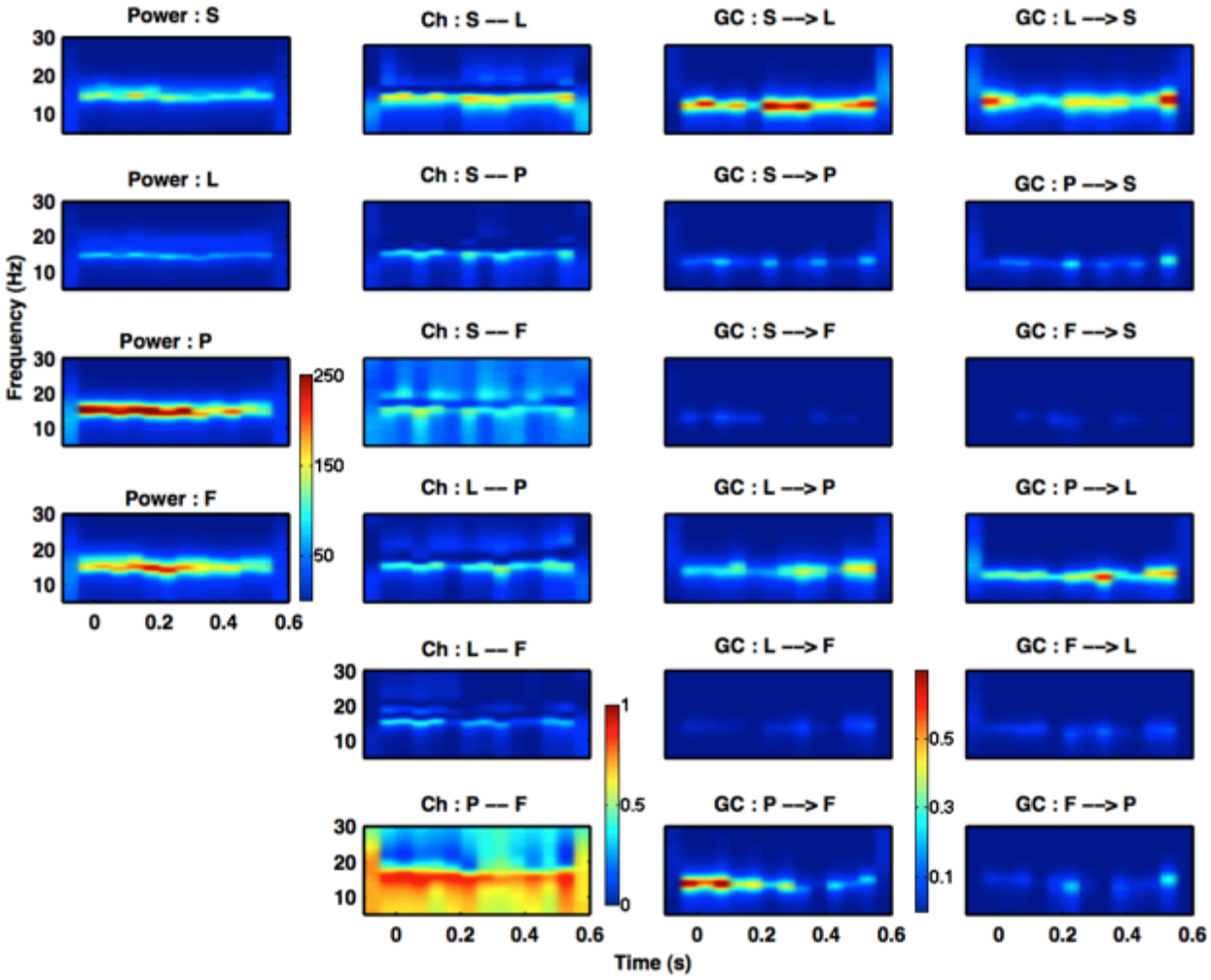

Figure A7: Time-frequency analysis, beta-oscillations. The first column shows power, the second column shows coherence (Ch), and the third and fourth columns show pairwise Granger causality (GC), where S = SI, L = LOC, P = pIPS, and F = dlPFC. Power, coherence and Granger causality spectra show peaks at around 15 Hz.

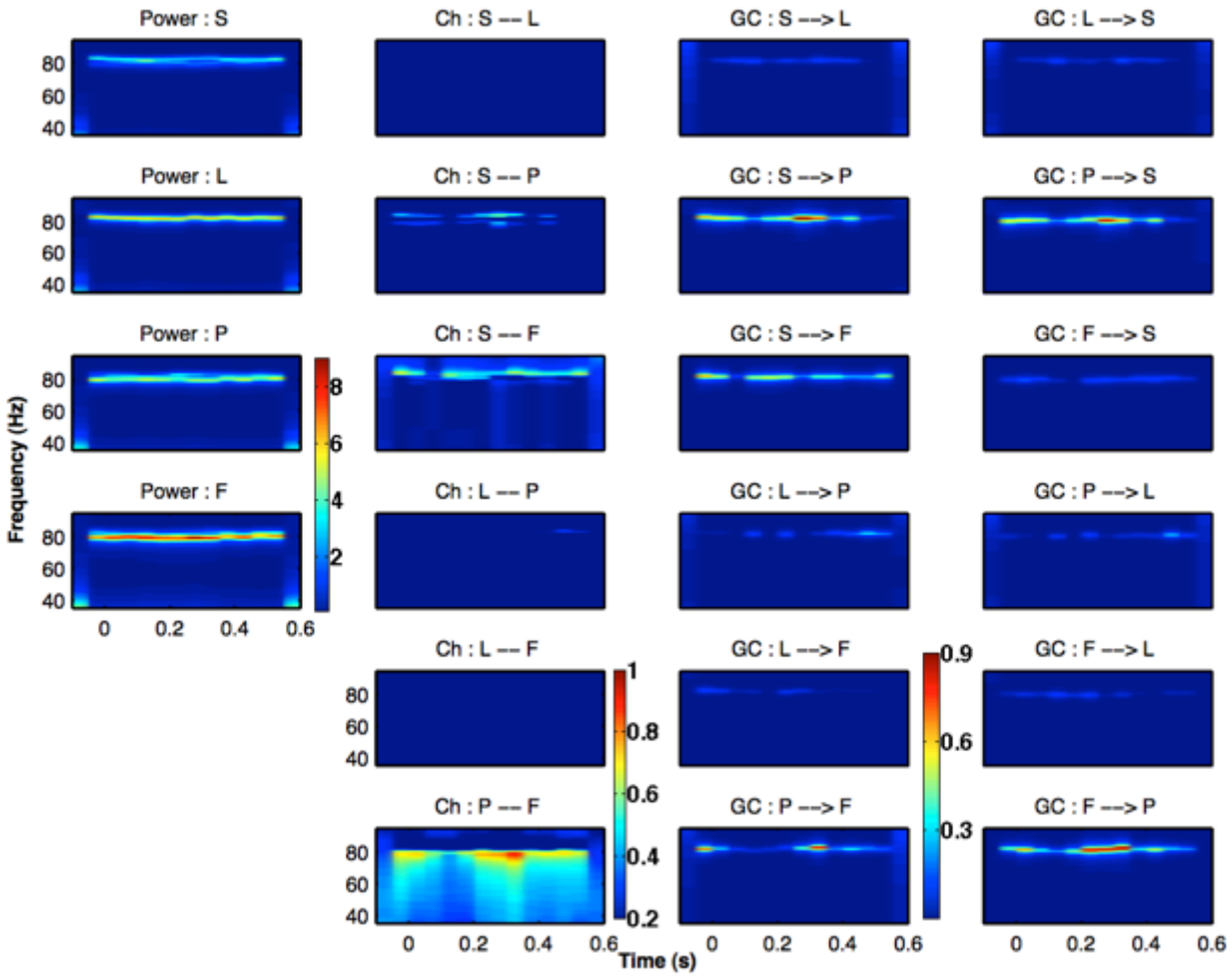

Figure A8: Time-frequency analysis, gamma-oscillations. The first column shows power (P), the second column, coherence (Ch), and the third and fourth columns, pairwise Granger causality (GC). S, L, P, and F as in Fig. A7. Power, coherence, and Granger causality spectral peaks occur at around 80 Hz.

Appendix A.6: Brain-behavior correlation

Here, we include all the results (significant and not significant) trying to establish brain and behavior relationships. We looked at the relationship between task performance accuracy and network activity (coherence and Granger causality). Source waveforms were collected both for correct and incorrect response trials from all network nodes and were used to compute the coherence and the causality spectra across subjects. We computed coherence and Granger cau-

sality values separately for both beta and gamma bands from each participant to examine the relationship between behavioral and electrophysiological data. The coherence values in the beta band (Fig. A9) and gamma band (Fig. A10) are plotted here as a function of average performance accuracy (z-score), for each pair of nodes. We found significant positive correlations between coherence and behavioral performance for SI-LOC and pIPS-dlPFC in the beta band and for pIPS-dlPFC and SI-dlPFC in the gamma band.

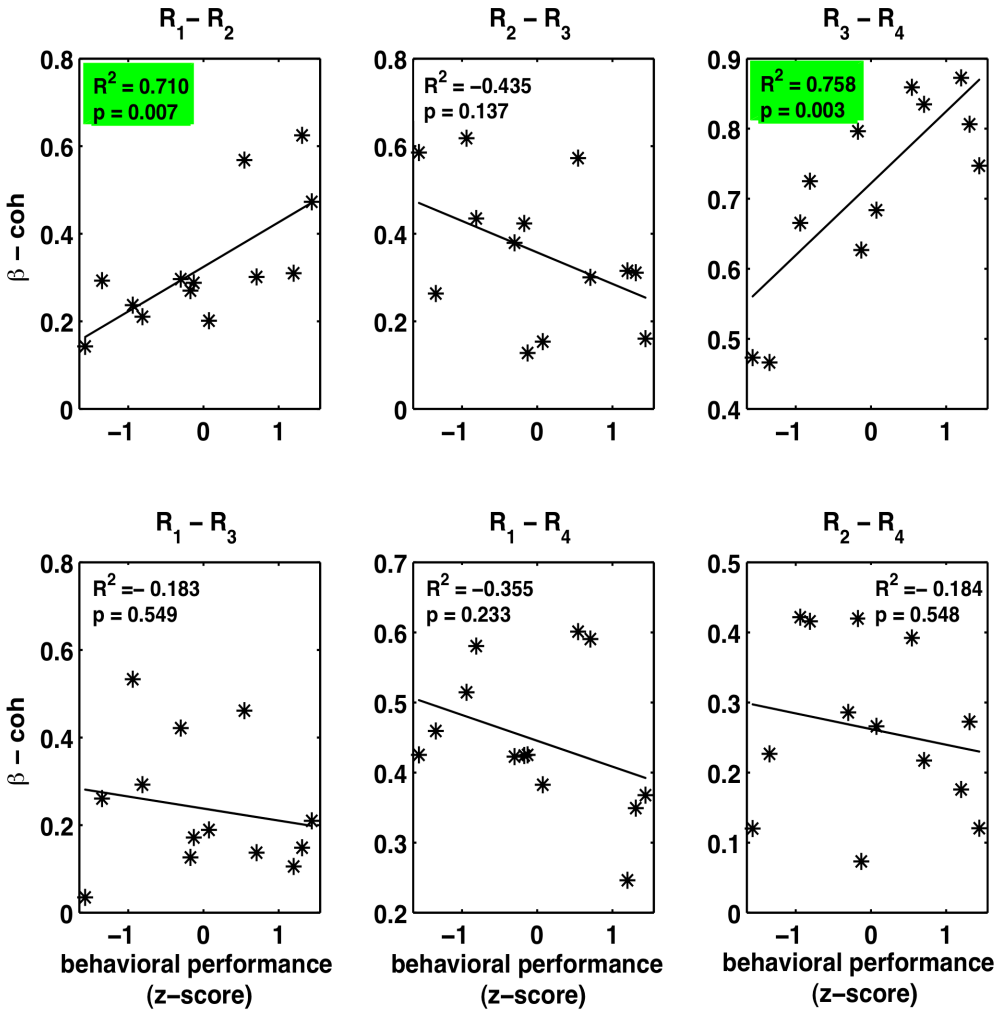

Figure A9: Relation between coherence and behavioral performance in the beta band. The highlighted subplots show pairs of nodes where coherence was significantly positively correlated with behavioral accuracy (green highlights). R1, R2, R3, and R4 as in Fig. A3.

Figures A11 and A12 represent the Granger causal influences as a function of average accuracy in the beta and gamma bands, respectively. In the beta band, the Granger causal influence from pIPS to dlPFC was positively correlated with accuracy whereas the Granger causal influences from SI to LOC and LOC to pIPS tended to be significant. In the gamma band, the Granger causal influences from dlPFC to pIPS and SI to dlPFC were positively correlated with accuracy whereas the Granger causal influences from pIPS to SI tended to be significant.

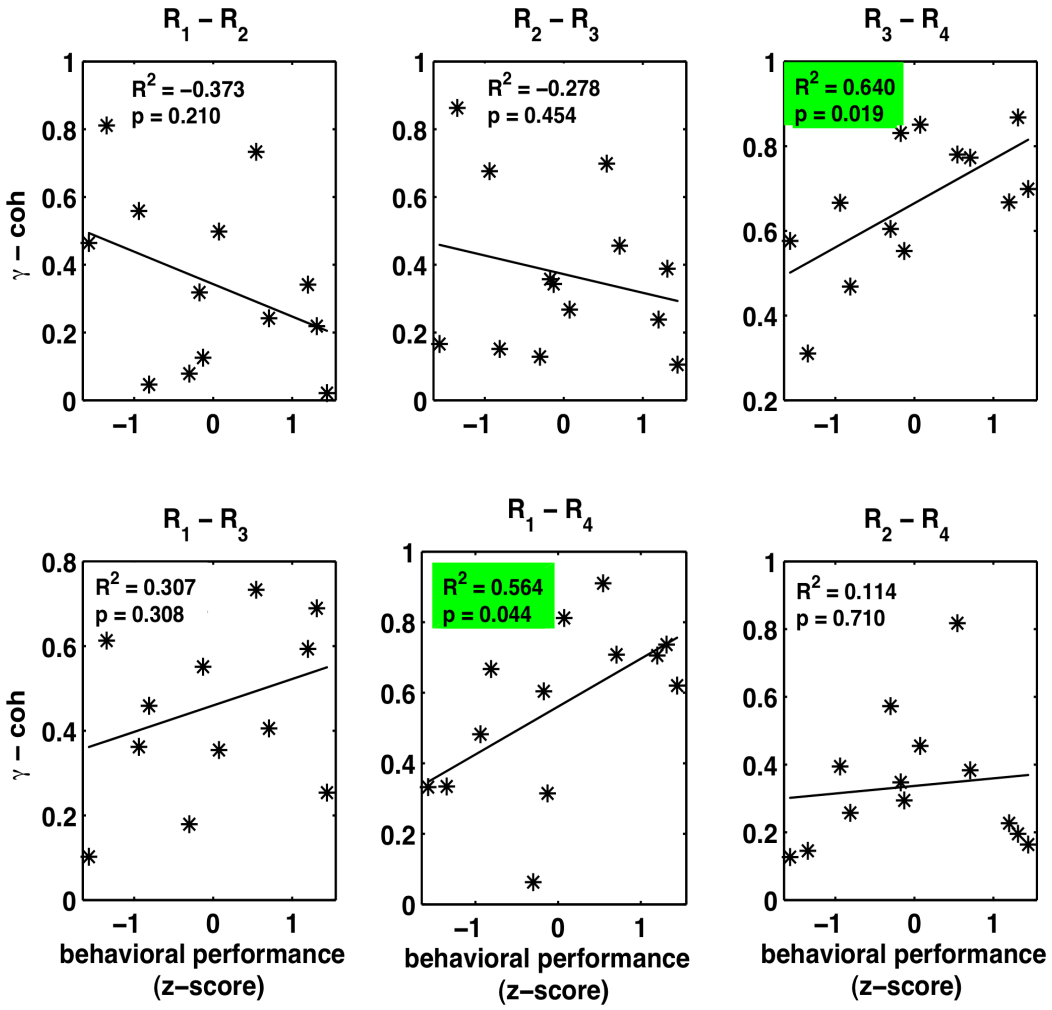

Figure A10: Relation between coherence and behavioral performance in the gamma band. The subplots highlighted in green represent pairs of nodes with significant positive correlations between coherence and behavioral accuracy. R1, R2, R3, and R4 as in Fig. A3.

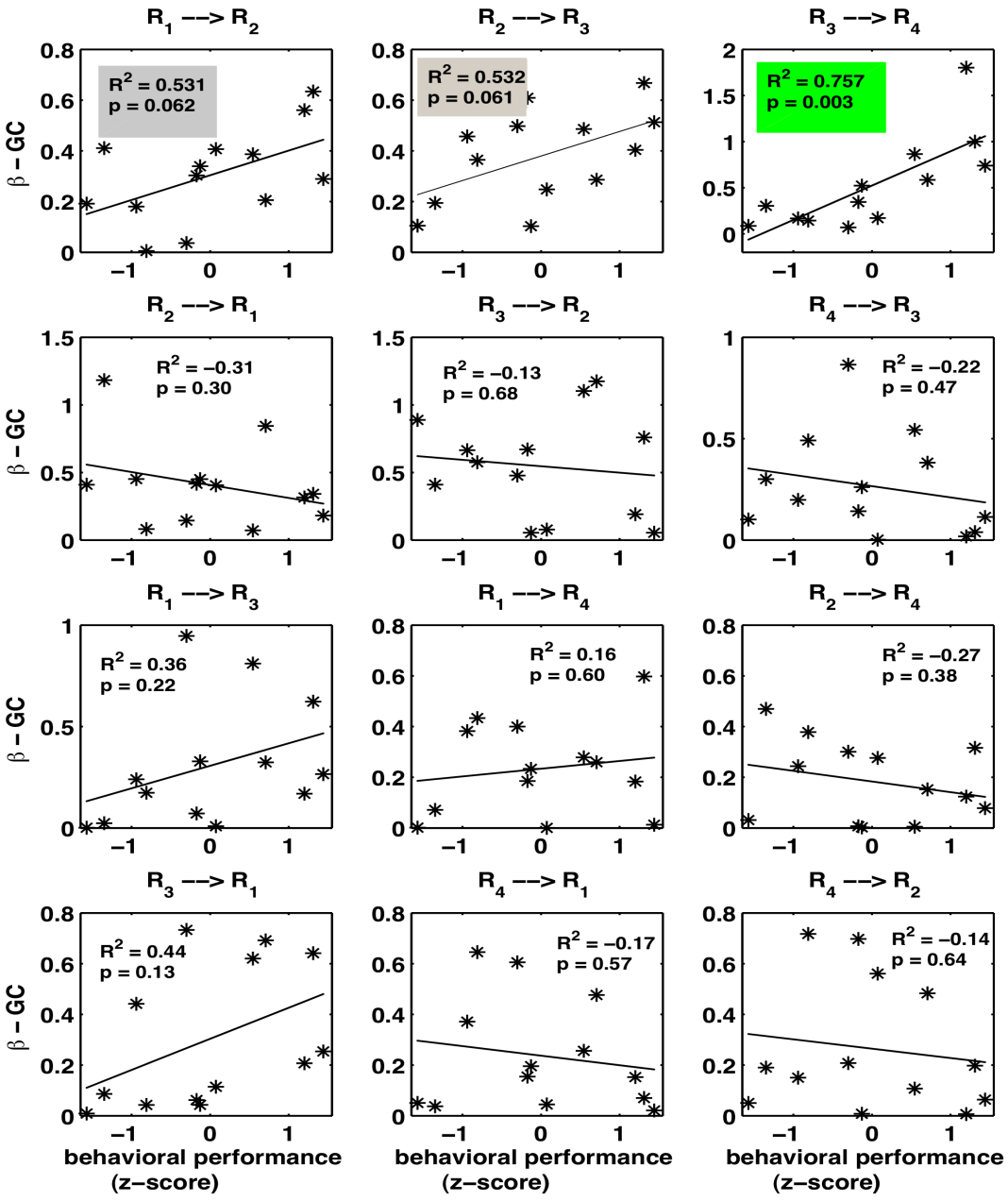

Figure A11: Relation between Granger causal influences and behavioral performance in the beta band. The highlighted subplots show Granger causal influences significantly positively correlated with behavioral accuracy (green) or tending to be significantly correlated (gray). R1, R2, R3, and R4 as in Fig. A3.

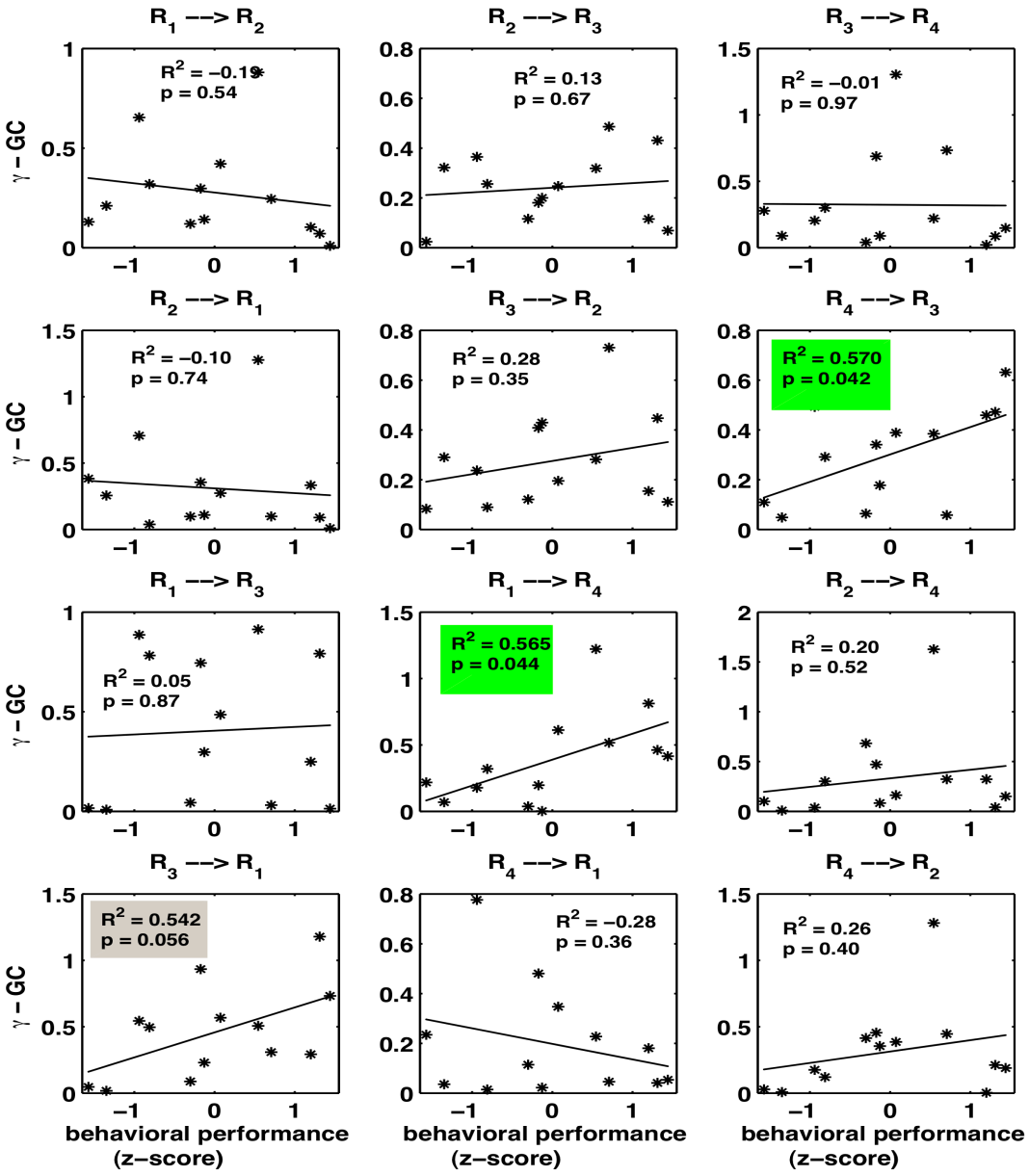

Figure A12: Relation between Granger causal influences and behavioral performance in the gamma band. The highlighted subplots either show Granger causal influences significantly positively correlated with behavioral accuracy (green) or tending to be significantly correlated (gray color). R1, R2, R3, and R4 as in Fig. A3.

Appendix B

Here, we report additional results (Figures B1-B11 below): (i) Granger causality results for all patients P1-P8 in Figures (B1- B8) (A-D), (ii) total interdependence (TI) at different time windows in patient P4 shown in Figure B9 (A-D), (iii) integrated net-causal outflows (iOF) and inflows after the time of significant causality in patient P4 shown in Figure B10 (A-C), and (iv) integrated Granger causality (iGC) and integrated outflows (iOF) after the time of significant causality in patient P5 in Figure B11. The results from patient P4 as a representative patient are included in the main manuscript.

Appendix B.1: Granger causality results for all patients P1-P8

Figures B1-B8. Here, figures (A-C) show the net causal outflow averaged over time (A), over frequency (B) and over recording channel (C), and figure (D) shows net causal outflow over time from all electrodes. The white dashed lines in (B-C) and black dashed line in (D) represent the onset time of seizure assessed by using traditional visual criteria (from clinical evaluation). The green dashed line in (D) represents the time when net causal outflows cross the 3 standard deviations from our calculation. In all patients, the Granger causal relationships at high frequency (>80 Hz) could be defined among groups of electrodes. In these patients, the high frequency causality started to appear around 2.0 s to 12.5 s (patients' average ± standard error = 6.3 ± 1.4 s) before the onset of clinically identified ictal activity. Abbreviations used here are: f = frequency, Ch = channel, OF = net causal outflow, OF_t = outflow averaged over time, OF_f = outflow averaged over frequency, and OF_{Ch} = outflow averaged over channel.

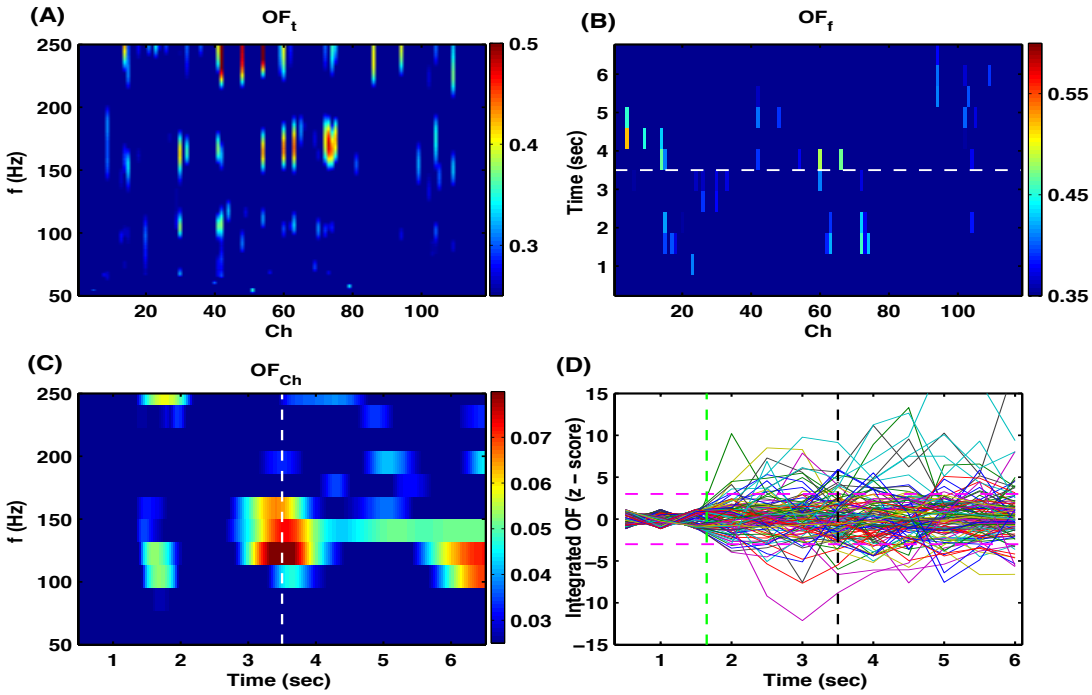

Figure B1: Patient 1

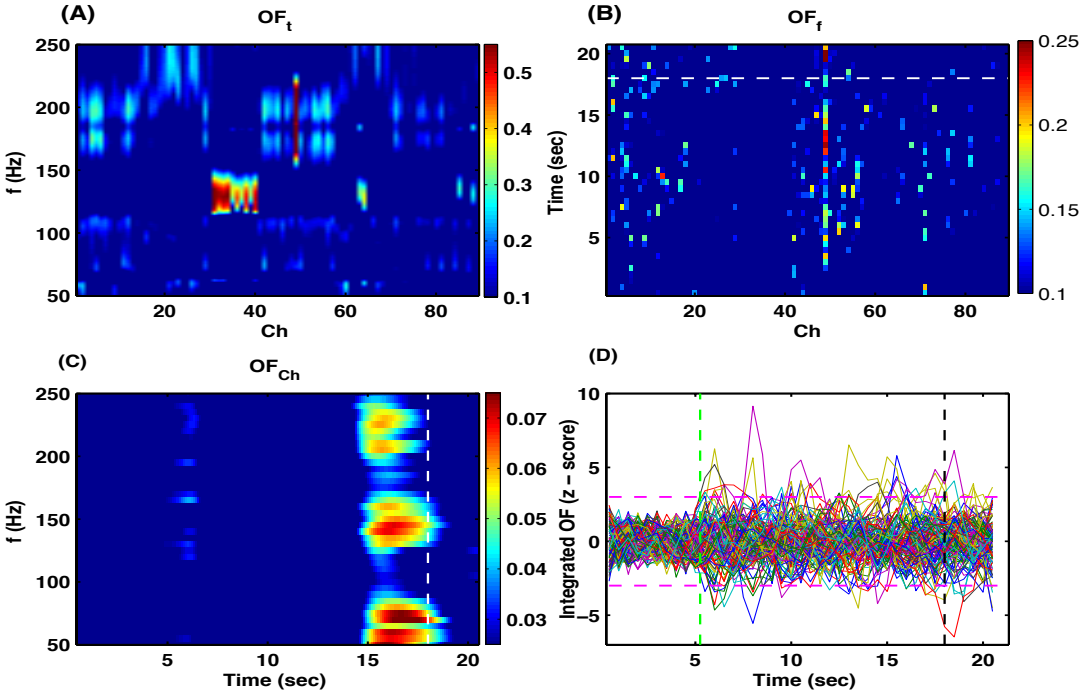

Figure B2: Patient 2

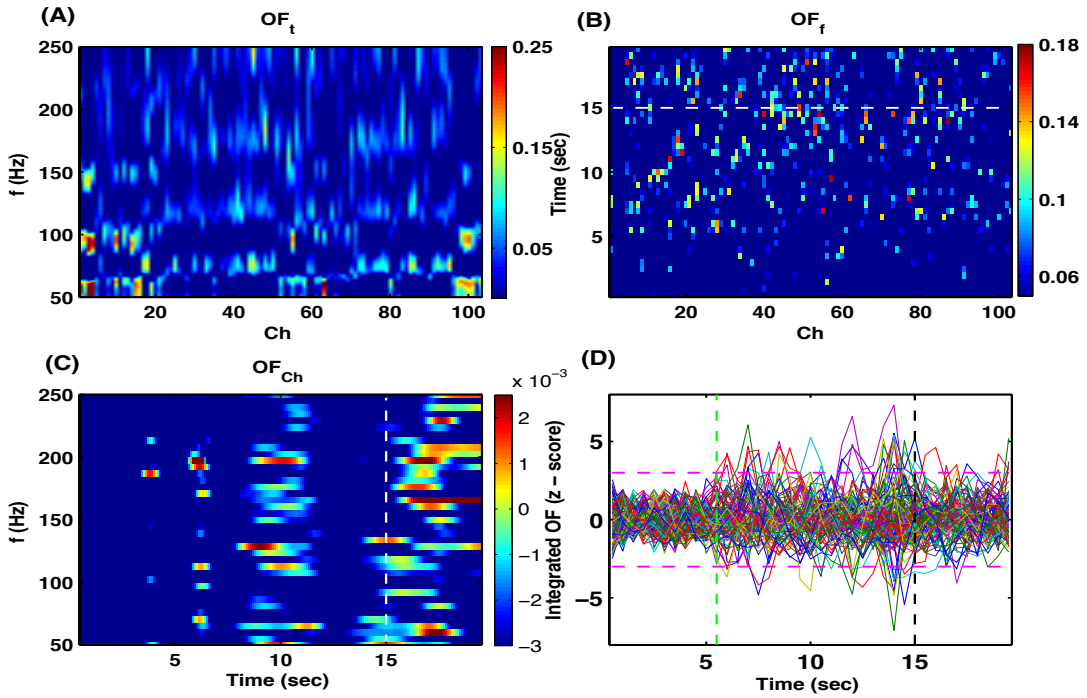

Figure B3: Patient 3

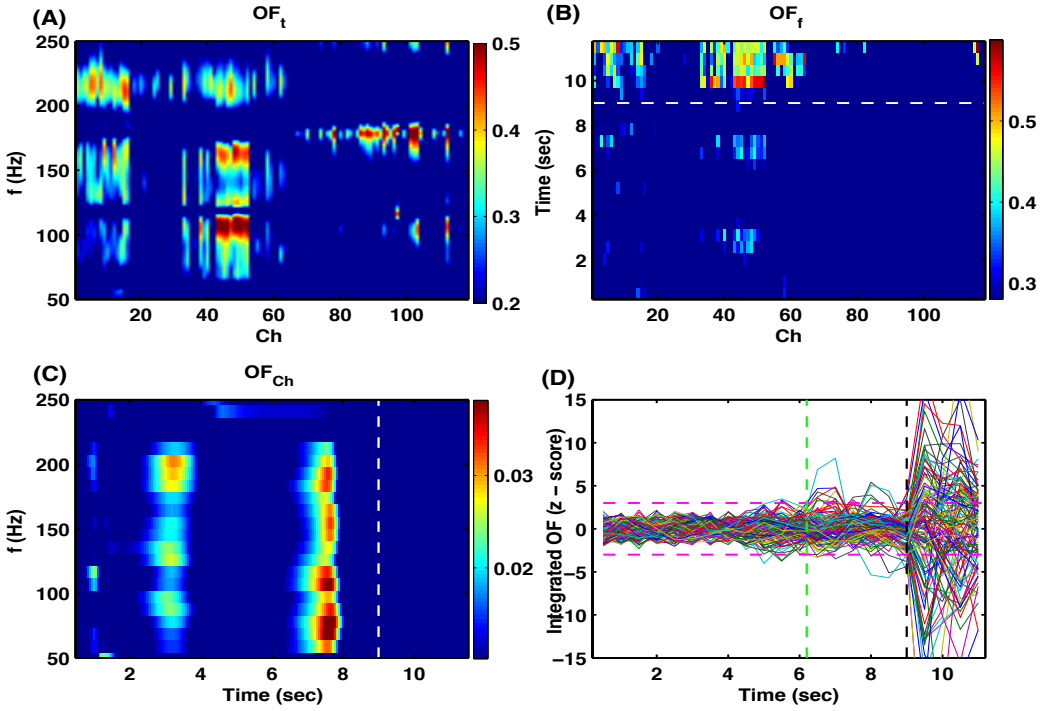

Figure B4: Patient 4

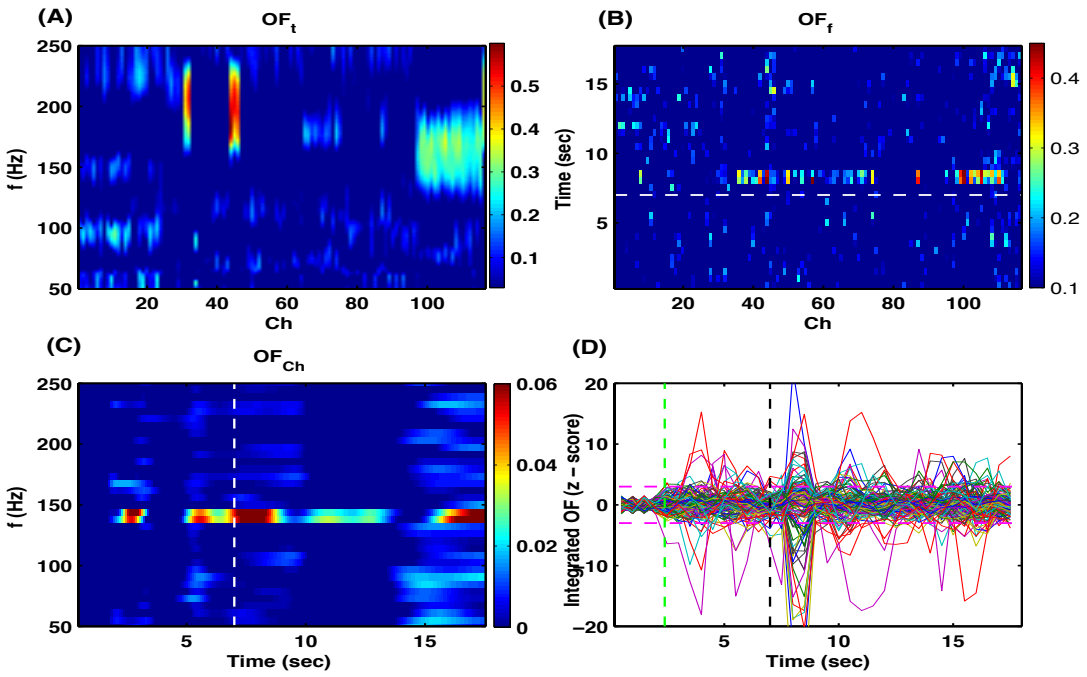

Figure B5: Patient 5

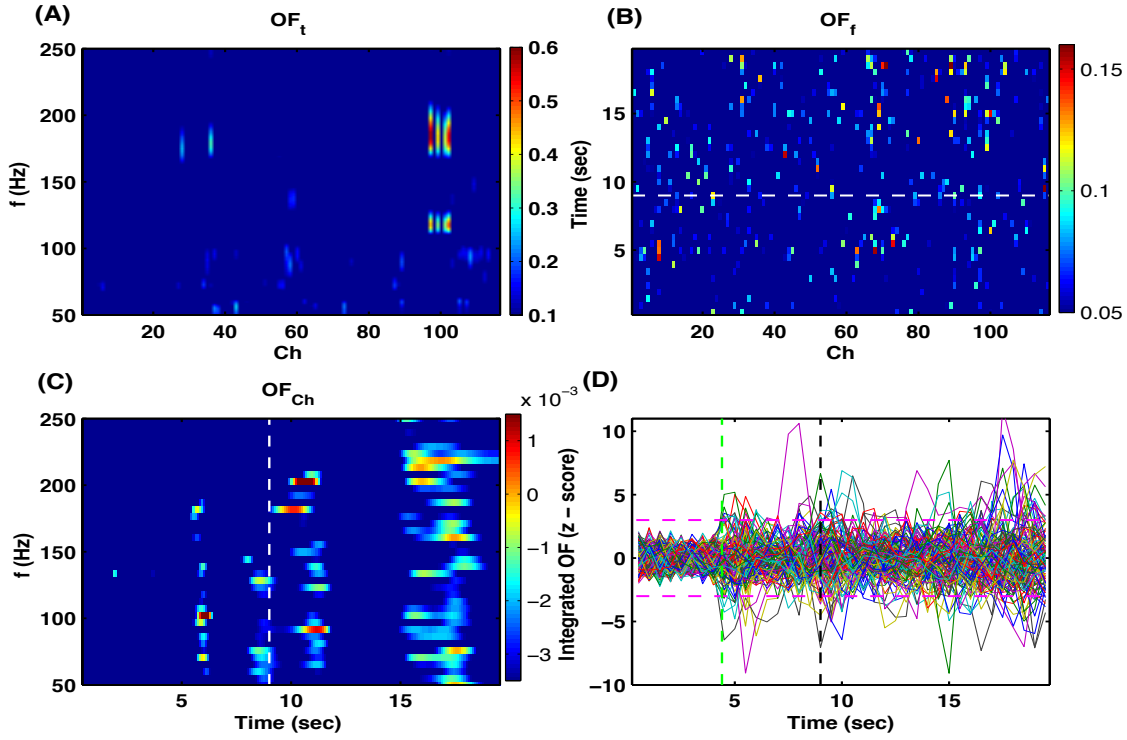

Figure B6: Patient 6

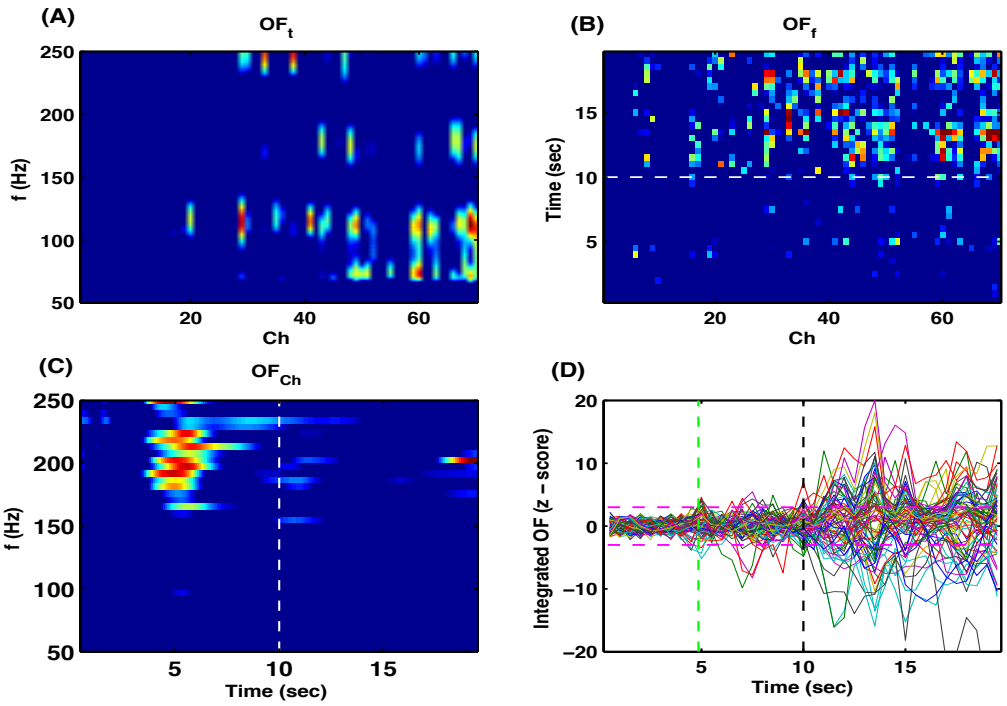

Figure B7: Patient 7

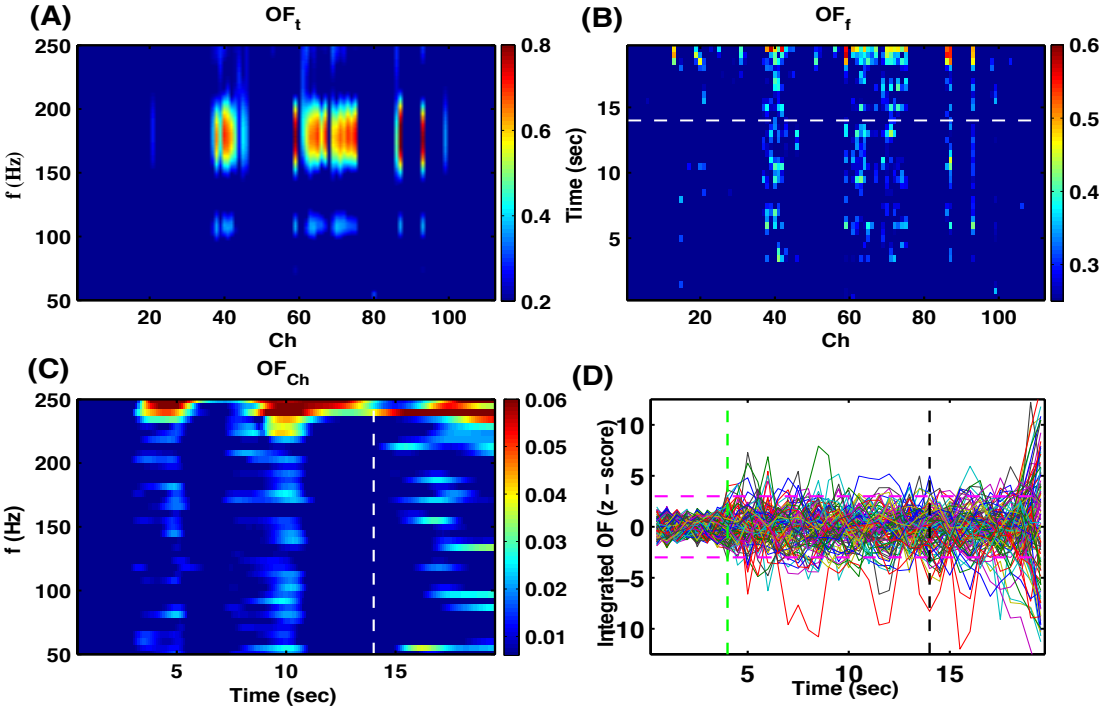

Figure B8: Patient 8

Appendix B.2: Total interdependence (TI) at different time windows in patient P4

Matrices of total interdependence (TI) at time = 8.5, 9.0, 9.5 and 10 s in Patient 4. This measure clearly shows where a seizure originates and how it propagates over the network reaching the hyper-synchronized state.

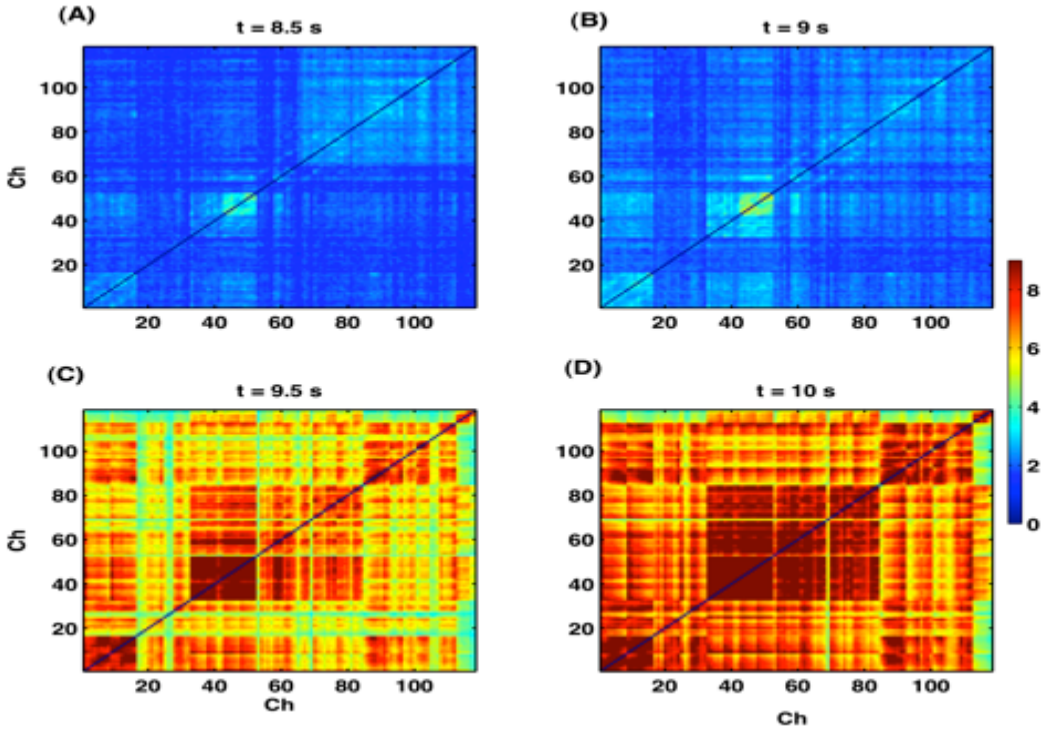

Figure B9: Matrices of total interdependence (TI) at time = 8.5, 9.0, 9.5 and 10 s in patient P4

Appendix B.3: Integrated net-causal outflows (iOF) and inflows after the time of significant causality in patient P4

Figure B10 (A-C). Integrated outflows (iOF) and integrated Granger causality (iGC) in patient P4. Fig (A) represents the frequency-integrated net causal outflows (iOF) after the time of significant causality ($t \approx 6s$). Here, sources (having +ve iOF) are categorized and shown in different colors according to iOF compared to standard deviation of GC = 0.0167 from the pre-ictal period. Figures (B-C) show the integrated Granger causality (iGC) in- and outflows from

and to channels: to Ch 23 [(B10 (B)] and to Ch 65 [B10 (C)]. These two channels plus others having –ve iOF were the sink channels in B10 (A).

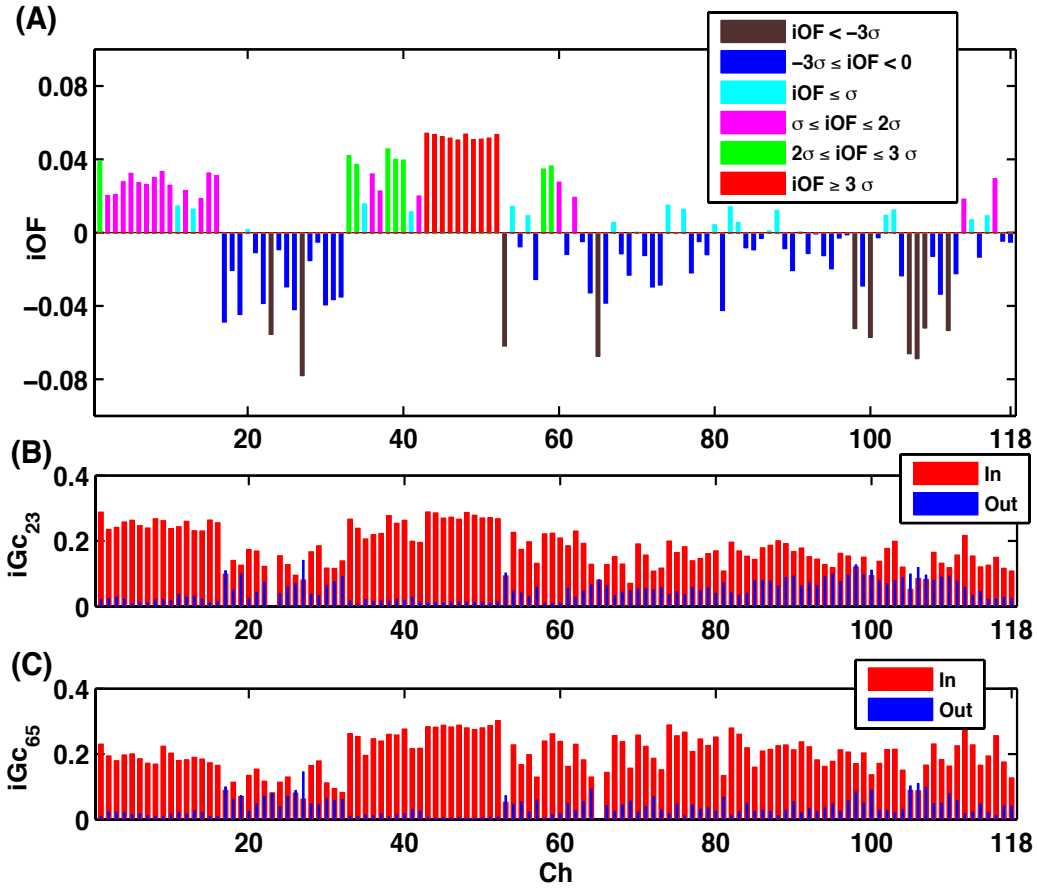

Figure B10: Integrated outflows (iOF) and integrated Granger causality (iGC) in patient P4.

Appendix B.4: Integrated Granger causality (iGC) and integrated outflows (iOF) after the time of significant causality in patient P5

Figure B11 (A-C). Fig. B11 (A) shows results of iGC in the ictal period at t = 8.5 s (in patient P5). Here, some channels [e.g. Ch = 34, 4.S11 (B)] receive stronger causal influences from other channels and some other channels [e.g. Ch = 44, B11 (C)] send out more than receiving from others.

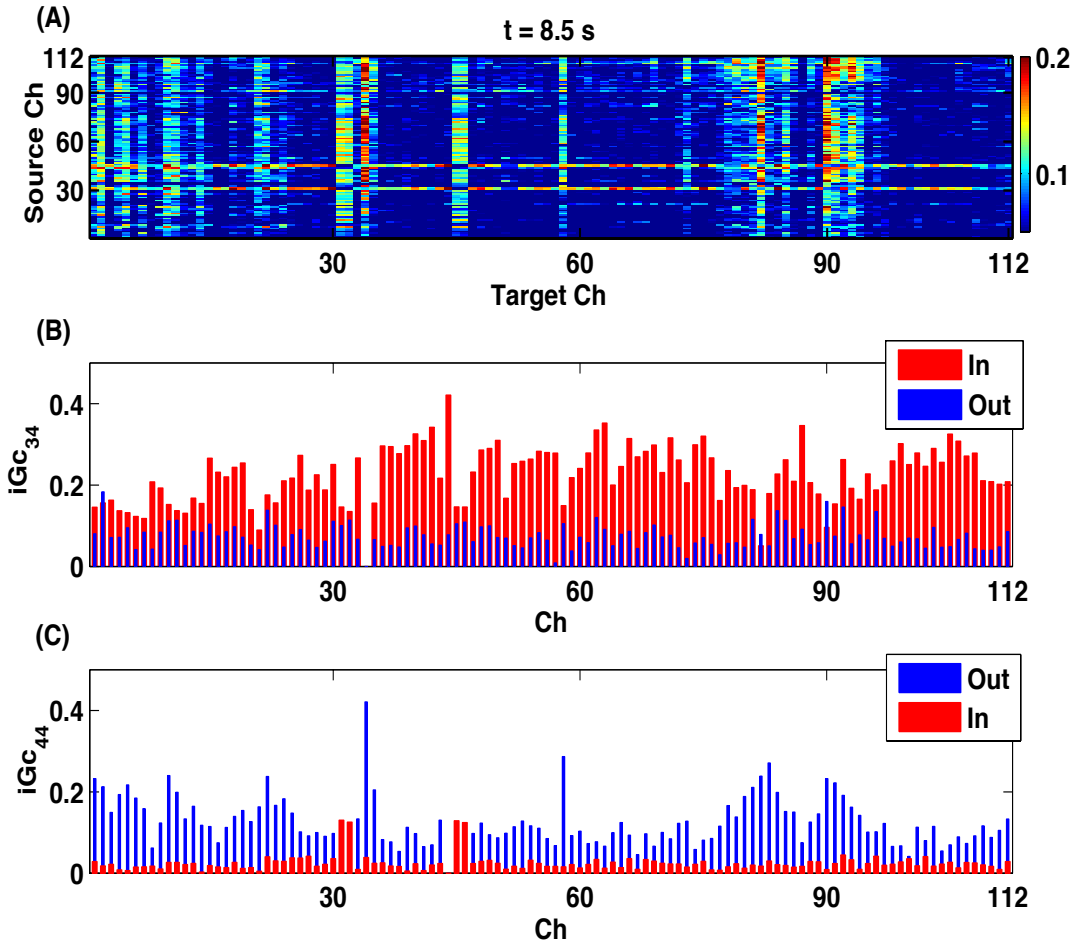

Figure B11: Granger causality results in patient P5